Philipps Universität Marburg

Microwave Measurements on n-Disk Systems and Investigation of Branching in correlated Potentials and turbulent Flows

Dissertation

zur

Erlangung des Doktorgrades der Naturwissenschaften

(Dr. rer. nat.)

dem

Fachbereich Physik

der Philipps-Universität Marburg

vorgelegt von

Sonja Barkhofen

aus

Krefeld

Marburg/Lahn, 2013

Vom Fachbereich Physik der Philipps-Universität als Dissertation angenommen am 02.07.2013
Erstgutachter: Prof. Dr. Ulrich Kuhl
Zweitgutachter: Prof. Dr. Bruno Eckhardt
Tag der mündlichen Prüfung: 10.07.2013
Hochschulkennziffer 1180

Abstract

In this work we investigate the wave propagation in three different complex systems. In the first two systems we focus on the wave propagation through random potentials, the first one in a microwave and the second one in an acoustic setup. In both systems we focus on the non-Gaussian properties of the measured quantities. The third system is a paradigmatic example of a fully chaotic open system with a fractal repeller. Here the relation of the classical periodic orbits and quantum mechanical quantities is studied.
In the first experiment we induce a potential into the microwave cavity by placing randomly distributed metallic scatterers on the bottom plate. Spatially resolved measurements of the full wave function reveal strong intensity fluctuations and a condensation of the wave flow along classical caustics. Additionally the scaling behavior of the branching with respect to the standard deviation of the potential is investigated and the predicted exponent of $-2/3$ is reproduced. As there are several open modes in the cavity due to the high frequency, effects of mode interference and mode coupling are found and explained, which go beyond the theoretical model. Perturbation theory of the Helmholtz equation for non-parallel top and bottom plate reveals extra source terms for the wave function, which are induced by the other open modes. These dynamics are also found in the experimental data.
The second experiment deals with an acoustic setup, where the sound of a turbulent air flow is recorded. Here strong deviations from the central limit theorem, which predicts a Gaussian distribution of wave intensities, are observed. In a second experiment performed in a wind tunnel a monochromatic sound wave is sent through the air flow. The hope to learn something about the properties of the turbulence by investigating the modulations of the original sound is not met. But again non-Gaussian behavior is found.
In the third part of this thesis another complex system is studied in a microwave setup: The n-disk system consists of n equal disks placed on an equilateral polygon in a two dimensional plane. Such an open systems provides complex resonances, which are extracted from our measured spectra via an elaborate algorithm, the harmonic inversion. The challenges of this extraction are discussed in detail and possible solutions for arising problems are suggested. The finally obtained resonances are used for the calculation of the counting function of the real parts, whose growth is predicted by the Hausdorff dimension as leading order. The distributions of the imaginary parts are studied with respect to the opening of the system. The largest (negative) imaginary part defines the spectral gap, which is compared to predictions, which can be calculated by using the periodic orbits of the sys-

tem. By similar means a suggestions for the development of the maximum of this distribution is tested. Moreover the experimental data is compared to the quantum mechanical calculation of the system.

Zusammenfassung

In dieser Arbeit wird die Wellenausbreitung in drei verschiedenen komplexen Systemen untersucht. In den ersten beiden geht es um Wellenausbreitung in zufälligen Potentialen, einmal in einem Mikrowellenaufbau und einmal in einem akustischen Experiment. Der Fokus liegt hier auf den nicht-Gaußschen Eigenschaften der Messgrößen. Das dritte System ist ein typisches Beispiel für vollchaotische offene Systeme mit fraktalem Repeller. Damit untersuchen wir die Verbindung zwischen klassischen periodischen Bahnen und quantenmechanischen Größen.
Im ersten Experiment bauen wir in die Mikrowellenkavität ein Potential ein, indem wir metallische Streukörper auf der Bodenplatte zufällig verteilen. In ortsaufgelösten Messungen können wir die gesamte Wellenfunktion untersuchen und finden starke Fluktuationen in der Intensität der Wellenfunktion. Besonders hohe Intensitäten finden sich dort, wo das analoge klassische System Kaustiken ausbildet. Außerdem wird untersucht, in welchem Abstand zur Quelle die Verästelungen starker Intensität anfangen, und ihre Skalierung bezüglich der Eigenschaften des Potentials getestet. Der vorhergesagte Exponent von $-2/3$ kann reproduziert werden. Da bei den hohen Frequenzen, bei denen gemessen wurde, mehrere Moden in der Kavität offen sind, konnten zusätzlich Effekte durch Interferenz von Moden und Koppeln zwischen Moden gefunden werden, die nicht in den theoretischen Modellen berücksichtigt sind. Erst ein störungstheoretischer Ansatz für die Helmholtz-Gleichung zeigt für nicht parallele Deckel- und Bodenplatte, dass es zusätzliche Quellterme für eine Mode durch die jeweils anderen Moden gibt. Dieser Effekt kann in dem experimentellen Daten bestätigt werden.
Im zweiten Experiment mit dem akustischen Aufbau wurde der Schall, der von einer turbulenten Luftströmung verursacht wird, gemessen. Die Ergebnisse weichen stark von einer Gaußverteilung der Intensitäten ab, die der zentrale Grenzwertsatz vorhersagt. In einem zweiten Experiment in einem großen Windkanal wird zusätzlich ein Ton defnierter Frequenz durch den Luftstrom gesendet. Die Hoffnung, aus der Modulation dieses Signals Rückschlüsse auf die Eigenschaften der Turbulenz ziehen zu können, wird nicht erfüllt. Aber wieder wird nicht-Gaußsches Verhalten gefunden.
Für den dritten Teil der Arbeit kommen wieder Mikrowellenexperimente zum Einsatz, um ein weiteres komplexes System zu erforschen. Das sogenannte

n-Scheiben System besteht aus n gleichartigen Scheiben, die auf einem gleichseitigen Polygon in einer zweidimensionalen Ebene positioniert sind. In solch offenen Systemen sind die Resonanzen nicht mehr reell, sondern komplex. Diese aus unseren Messdaten zu extrahieren, erfordert einen ausgefeilten Algorithmus, die harmonische Inversion. Die Herausforderungen der Resonanzextrahierung werden angesprochen und Lösungsvorschläge diskutiert. Die letztendlich erhaltenen Resonanzen werden benutzt, um die Zählfunktion der Realteile aufzustellen. Ihr Wachstum ist in führender Ordnung durch die Hausdorff-Dimension gegeben. Die Verteilung der Imaginärteile wird in Abhängigkeit der Öffnung des Systems untersucht. Der größte der ausschließlich negativen Imaginärteile gibt die spektrale Lücke an. Diese wird mit den Vorhersagen verglichen, die auf Berechnungen über die periodischen Bahnen beruhen. Auch für die Abhängigkeit des Maximums der Verteilung von der Öffnung des Systems gibt es theoretische Annahmen, die auf ähnlichen Berechnungen beruht. Diese konnte ebenfalls unterstützt werden. Zusätzlich werden die experimentellen Resonanzen mit quantenmechanischen Berechnung verglichen.

Contents

1 Introduction

Wave phenomena in complex media are found in every field of physics and affect many parts of our everyday life. Multitudinous effects are related to that from lengths of a few Angstroms to thousand of kilometers, from quantum mechanical eigenfunctions of a Schrödinger equation describing elementary particles [1], over Bloch waves in periodic crystals [2], to water waves in the ocean, seismic waves due to continental drifts [3], or sound waves in our communication. There is great variety of complex dynamics to treat. One important topic is the interplay between the (quantum mechanical) wave picture and the corresponding (classical) point particle dynamic. As due to Bohr's correspondence principle the classical behavior must reappear in the quantum mechanical description for high energies, the semiclassical limit [4]. One might also think about Feynman's path integral methods, a generalization of the classical action principle of a single trajectory [5]. But already before the semiclassical limit is reached there are relations between classical/particle properties and quantum mechanical quantities as e.g. the eigenvalue distribution [6], counting function [7], wave intensity distributions [8].
In the first part of this thesis we investigate the wave propagation in a random potential landscape using a microwave setup [9]. Though the potential is very weak the wave pattern is shaped in an astonishing way: Instead of a random speckle pattern the wave intensity condenses along branches. Those occur, where the analogous classical system provides caustics and has nothing to do with Anderson localization, that takes place on much larger length scales [10, 11]. Due to the flexibility and the controllability of the microwave setup it is possible to introduce potentials with exactly defined properties, i.e. their strength and their correlations [9, 12]. Thereby it is possible to study the emergence of the branches with respect to the structure of the potentials. The predicted scaling behavior is shown experimentally and an agreement between classical particle densities and wave intensities is found. One additional effect beyond the theoretical model is the mode coupling between the different open modes. In this point we have to expand the simple mode picture of the microwave resonator description and find many evidences for the interaction between the modes in our experimental results.
The basic idea of waves traveling through a random potential is taken up in the second part of this thesis, but in a different setup. Here we use sound waves and send them through a turbulent air stream or record the sound generated by the turbulence. In this setup it is possible to measure the wave signal time dependently and not only standing waves as in the microwave setup. The challenge of this experiment was the installation of a new acous-

tical setup and the specification of the best quantities to study the influence of the turbulence potential. Finally the experimental setup is functional and first evidences of a non-Gaussian distributions of the signal are found, but the parameter dependency is still questionable.
The third part deals with another open system, again studied via microwave cavities: the n-disk system, a paradigmatic example of fully chaotic system with a fractal repeller [13, 14]. Here one is typically not interested in the wave intensity distribution, but in the structure of the resonances. As the system is open, the resonances become complex. Thus we count the resonances regarding their real part to obtain the counting function and to study its growth. Additionally we investigate the distribution of their imaginary parts, especially the largest (negative) imaginary part, which defines the spectral gap. The predictions of the slope of the counting function in the semiclassical limit as well as the development of the gap and the maximum of the distribution of imaginary parts are calculated using the periodic orbits of the underlying classical system. Again the fingerprints of classical dynamic are found in the wave picture.

2 Microwave Basics

Quantum chaos in flat metallic cavities, the microwave billiards, have been studied experimentally over the last 23 years in many variations [9]. Two metallic plates adjusted parallel to each other with a small distance in an arbitrary shape define the volume, in which –inserted by an antenna– electromagnetic waves propagate. The underlying electromagnetic treatment for those systems is well understood and was often described in detail [9, 15, 16]. Nevertheless it is convenient to repeat the important equations once more.
From Maxwell's equations for solenoidal fields the Helmholtz equations for $\vec{E}$ and $\vec{B}$ can be derived:

$$(\Delta + k^2)\ \vec{E}(\vec{r}) = 0 \tag{2.1}$$
$$(\Delta + k^2)\ \vec{B}(\vec{r}) = 0 \tag{2.2}$$

with wavenumber $k = \omega/c$ and angular frequency ω. c is the speed of light in the medium in the cavities. The boundary conditions at the metallic surfaces of the cavity with the normal vector $\vec{n}$ look like

$$\vec{n} \times \vec{E} = 0 \tag{2.3}$$
$$\vec{n} \cdot \vec{B} = 0 \tag{2.4}$$

Exploiting the boundary conditions (2.3), (2.4) $E_\parallel = 0$ and $B_\perp = 0$ at top and bottom plate a separation ansatz of the mode in z-direction (perpendicular to the plates) and the modes in x- and y-direction (parallel to the plates) is possible. For a cavity with a height smaller than half of the wavelength only the z-component of the fields $\vec{E}$ and $\vec{B}$ can form a standing wave. The first state is called TM-mode, the latter one TE-mode. Hence this component ψ can be treated separately by two dimensional Helmholtz equation (2.1)

$$(\Delta_{xy} + k_{xy}^2)\ \psi(\vec{r}) = 0 \tag{2.5}$$

The wavenumbers are given by

$$\begin{aligned} k^2 &= k_x^2 + k_y^2 + k_z^2 \\ \Rightarrow k_{xy} &= \sqrt{k^2 - k_z^2} \end{aligned} \tag{2.6}$$

For higher frequencies, i.e. smaller wavelengths, there exists also standing waves in z-direction. In this case solutions for TM modes look like $E(x, y, z) = E(x, y)\cos(n\pi z/h)$, which –inserted in equation (2.1)– leads to

$$\left[-\Delta_{xy} + \left(\frac{n\pi}{h}\right)^2\right] E_z(x, y) = k^2 E_z(x, y) \tag{2.7}$$

A comparison with the analog two dimensional Schrödinger equation

$$\frac{\hbar^2}{2m}\left[-\Delta_{xy} + V(x,y)\right]\psi(x,y) = E\psi(x,y)$$

suggests to treat the extra term due to the modes in z-direction ($n > 0$) as a potential [17, 12]. The eigenvalue E corresponds to k^2 and k_z can be evaluated via

$$k_z = \frac{2\pi}{\lambda_z} = \frac{n\pi}{h} \tag{2.8}$$

for n being the number of half wavelengths, which fit in the cavity height h. For $n = 0$ the potential-free original case, the TM_0 mode, is reproduced.
In part III about n-disk systems I will present microwave measurements in flat cavities, where only the TM_0 mode propagates and no potential is induced, but the shape of the billiard boundary defines the system. In part I about branching formation we use from the potential term in equation (2.7)

$$V(x,y) = \left(\frac{n\pi}{h(x,y)}\right)^2 \tag{2.9}$$

By varying the height $h(x,y)$ between the two plates we can introduce a potential landscape for the propagating waves. As this height variation must be adiabatic, as otherwise the mode separation ansatz is not valid anymore, our system can only be approximated in this picture. Especially the TM_0 mode cannot be well described by this ansatz, as the potential corresponding to $n = 0$ is equal to zero and thus the mode is supposed to be constant. However, we will observe a spacial dependency of this mode experimentally, which then can be explained by perturbation theory, given in the appendix A. In the discussion of the experimental results in section 7 additional effects causing such an observation are mentioned.

Part I
Branched Flow in Weak Potentials

3 Motivation

The investigation of branched flow attracted much attention in various fields of physics, like electron gas in a quantum point contact [18, 19, 20], rogue sea waves [21], sound waves propagating through the ocean [22] and even microwaves experiments [23]. It is a universal phenomenon as many two dimensional flows can be approximately described by a Hamilton flow through a random potential. Is the potential weak and embodies a correlation, the basic ingredients are given for branching to occur. Especially the question how freak events, which are extreme events of rare probability, for example monster waves in the ocean [24], may be influenced by an underlying branching pattern of the classical flow, is of actual interest. Its significance for the survival of sailors and the protection of valuable goods transported on the seaway are obvious. Already in the 1970s Berry studied the influence of classical caustics on waves in random media [25] by analyzing the moments of the intensity distributions.
A phenomenon, which appears in so different contexts, but might be a consequence of one universal underlying model, is a typical application for microwave measurements. In his PhD-thesis Ruven Höhmann already observed branched wave functions in his measurements related to freak waves [23, 26]. He used randomly distributed brass scatterers to imitate a random potential, measured the wavefunction spatially resolved and obtained instead of random speckle patterns clear branching structures shown in figure 1 for frequencies around 30 GHz. The right part of figure 1 shows the ray density of the classical dynamics of the same potential. Here one can clearly see the similarities between the microwave intensity and the underlying classical behavior of the system. Further analysis had shown, that these enhanced intensities do not gather in the valleys of the potential, but follow the slopes of the scatterers, a clear hint that caustic formation is responsible [27]. In this direction I have thus performed further experiments to investigate in detail the connection between caustics and branched flow. First of all the theoretical approaches must be understood. They provide a scaling law for the occurrence of the first branches with respect to the properties of the potential. This behavior is the basis for many theories on the formation and the counting of branches

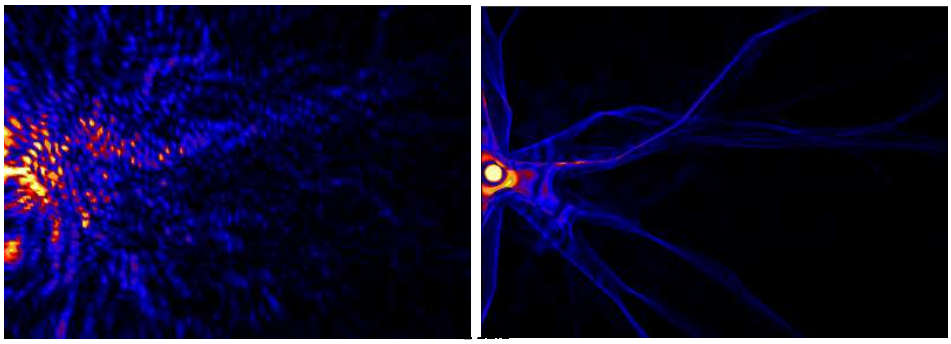

Figure 1: Example of branched microwave wavefunction (left) and the corresponding classical trajectory density (right), taken from [26]

[27, 28, 21], but was not experimentally verified, yet. The model will be presented in section 4. I shall present a new experiment to test this scaling law and to go beyond a qualitative comparison of branching patterns and the underlying classical trajectory densities. In the theoretical approaches I shall focus on the requirements on the experiment, which will result from them. These will be implemented in a new setup explained in section 5, as it turned out that the former experiments did not meet the demands. The quality and the adequacy of the new setup is tested in basic measurements first. They are discussed in section 6 and offer a convincing starting point for the measurements on large potential landscapes, see section 7. In the data analysis I will first establish a method to separate the several open modes from each other, because the scaling behavior is only valid for single modes and not for a superposition of multiple wave energies. For the single modes the branching pattern is compared to classical simulations of particle density in the same potential showing a reasonable agreement. Based on this similarity a quantity which defines the first occurrence of branches needs to be established and analyzed. The variance of the amplitudes over circles with a fixed distance from the source antenna is a promising candidate. Therewith the scaling law can be observed experimentally. Additionally one effect beyond the theory will arise: the coupling between modes. Consequences of it are found in the variance plots as well as in the wave patterns. With a perturbation ansatz they can be explained satisfactorily and display surprising properties, especially in the range where a mode just opened.

4 Theoretical Background

4.1 Classical Caustics

In this chapter I will give a brief overview over caustic formation in classical flows. Figure 2 (a) shows a typical example of the formation of caustics. In black the density of particle trajectories starting from the left with the same energy but with uniformly distributed angles is plotted. The potential is illustrated in the green-white color scale and in (b) in three dimensions and compared to the particle energy (orange). This figure as well as many theoretical models [27, 28, 21] use a weak Gaussian correlated potential in two dimensions

$$\langle V(\vec{r})\rangle = 0 \qquad c(|\vec{r}-\vec{r}'|) = \langle V(\vec{r})V(\vec{r}')\rangle = \epsilon^2 e^{-|\vec{r}-\vec{r}'|^2/l_c^2} \tag{4.1}$$

where ϵ denotes the potential strength and l_c is its correlation length. The potential is supposed to be weak compared to the kinetic energy E_k of the particle to avoid backscattering and Anderson localization on the scales we are looking at, see figure 2 (b). In the experiment by Topinka [18] and numerical simulations e.g. by Kaplan [27] a typical ratio is $\epsilon/E_k \approx 0.08$.
The process of caustic formation is visualized in 2 (c) and (d). We start the initial momentum in x-direction and set p_x and the mass to one. Based on these starting conditions the motion can be assumed to be unidirectional and x plays the role of the time. Hence we have $x(t) = t$ and $p_x(t) = p_x(0) = 1$. For the evolution in transverse direction we then have

$$\mathrm{d}y(t)/\mathrm{d}t = p_y(t), \qquad \mathrm{d}p_y(t)/\mathrm{d}t = -\partial V(t,y)/\partial y$$

and a reduced one-dimensional dynamic with an effective time-varying random potential. Initially we have zero transverse momentum p_y, thus investigate the stretching and folding of a straight manifold $p_y = 0$ in the reduced (y/v_y)-phase space, see lower panel of figure 2 (c). The upper panel in (c) shows the evolution of particle density in the configuration space. The vertical lines indicate the discrete time steps t_i at which the deformation of the manifold is plotted in the lower panel. In (d) the projection of two folded manifolds (red and orange) to the particle density ρ in configuration space is plotted. We see that caustics are caused by folding of the manifolds, i.e. the classical density diverges where

$$\left.\frac{\mathrm{d}p_y}{\mathrm{d}y}\right|_t = \infty$$

In such a weak potential a trajectory must pass over many correlation lengths in longitudinal x-direction, until it has traveled over one correlation length

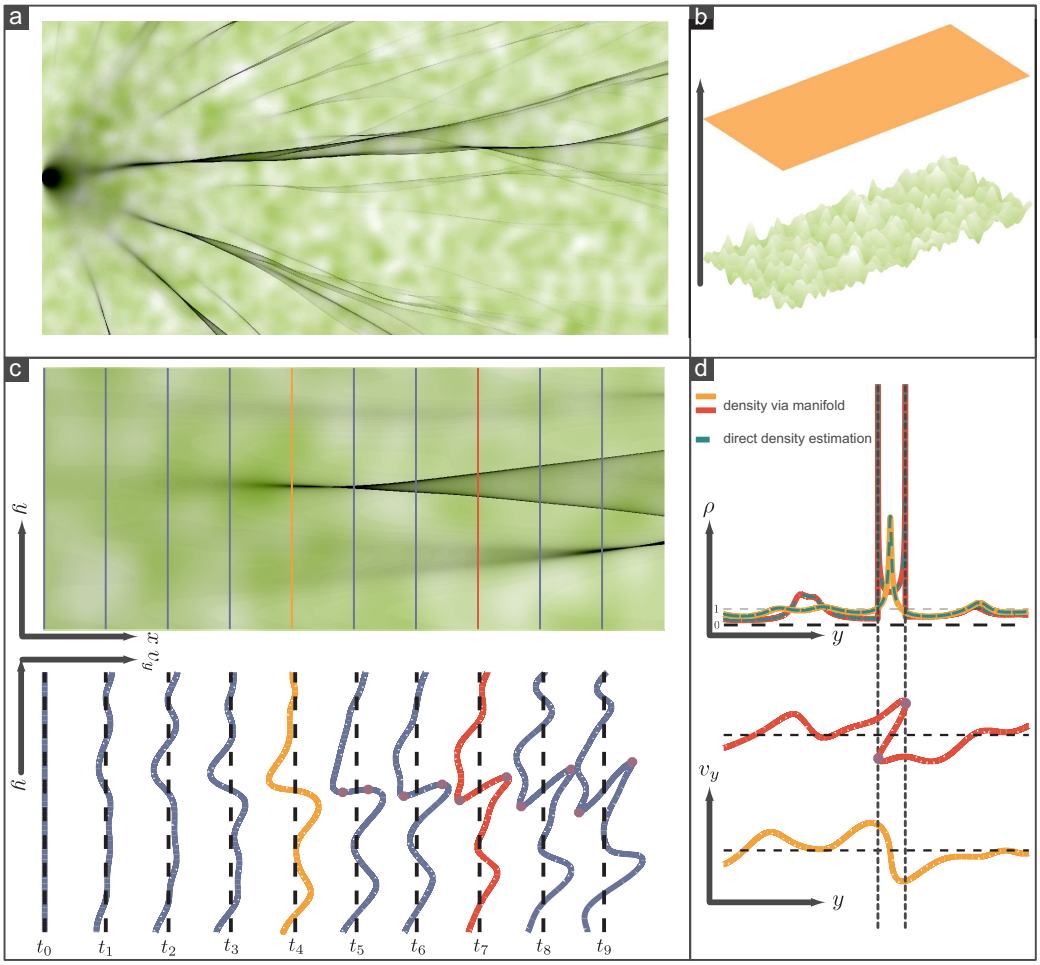

Figure 2: Process of deformation of a classical manifold in weak Gaussian correlated potential leading to caustics, provided by Jakob Metzger

in the transverse y-direction. The homogeneous "kicks" of the potential on the manifold over a correlation length result in the stretching and folding and therefore in the formation of the caustics. It occurs on the characteristic time scale [27]

$$t_0 \propto l_c \, \epsilon^{-2/3} \tag{4.2}$$

Its derivation is given in appendix B. This universal time scale enables universal theories for very different systems and potentials.
Up now all the considerations were performed for classical system, but can be expanded also to quantum and wave mechanical investigations. Then additionally a smoothing on a scale $b \ll 1$ must be performed in order to

get a well-defined height of the branch [27]. The uncertainty principle in quantum mechanics for example takes care on the smoothing automatically as the phase space area enclosed by a fold must be larger than $\hbar$ to resolve a caustic. Exploiting these considerations analytic expressions for the number of branches in those systems with respect to the source distance were found, e.g. in a far distance approximations [27] or even as a universal expression [28]. These theories are all based on the scaling law (4.2), which is now investigated experimentally for the first time.

5 Setup

5.1 The Scattering Potential

The experimental setup should realize the theoretical model described in the previous section, i.e. a system with waves propagating through a potential, which is Gaussian correlated with $\langle V(\vec{r})V(\vec{r}')\rangle = \epsilon^2 \exp(-|\vec{r}-\vec{r}'|^2/l_c^2)$ for two given positions $\vec{r}$ and $\vec{r}'$. A typical value for the standard deviation is 6 to 8 % of the particle energy, thus the potential is supposed to be very weak. Correspondingly I have to setup my new experiment with respect to these conditions. The former experiments used metallic cones (with height $H = 10\,\mathrm{mm}$ and radius $R = 12.5\,\mathrm{mm}$ and a minimal distance to the top plate of $h_{\min} = 10\,\mathrm{mm}$) which lead to an effective potential of

$$V(\vec{r}) = \frac{(n\pi)^2}{(h_{\min} + \frac{H}{R}|\vec{r}|)^2} \tag{5.1}$$

For $|\vec{r}| = 0$ it is not differentiable (see right part of figure 3) and thus does not meet the requirement of being smooth. Jakob Metzger performed simulations

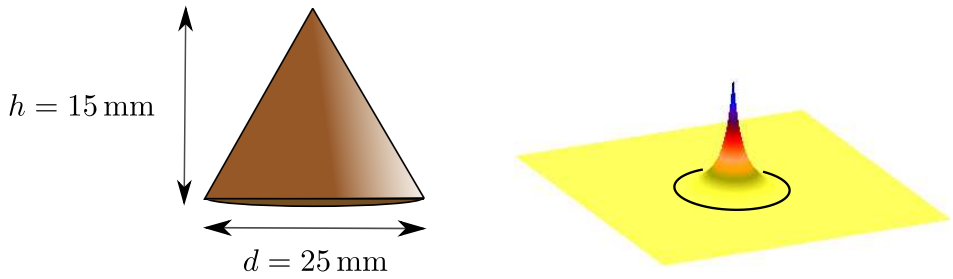

Figure 3: Geometry and potential of a conical scatterer with singularity at $r = 0$

with the cone potential to illustrate the strong scattering properties of each scatterer, see figure 4. Here it becomes clear, that the branching occurring in the wave pattern is not a multi-scattering effect in a weak potential as assumed, but every branch appears behind one scatterer (red circle), which appear to divide the flow. Consequently they are not suitable for our purpose. For the required weak potential we still want to use individual scatterers, as this guarantees the highest flexibility in the setup. A milling out of a certain shape in the bottom plate would be very cumbersome. A second simulation (figure 5) reveals that randomly distributed spherical caps would be a suitable

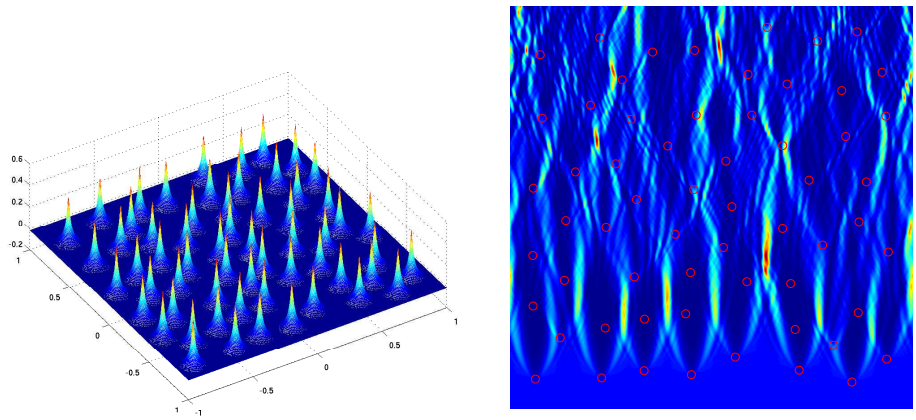

Figure 4: Left: Potential landscape given by conical scatterers. Right: Branching of an incoming plane wave in the given potential [29]

alternative as their scattering strength is much weaker and thus get closer to the assumptions of the model. Based on these simulations two different

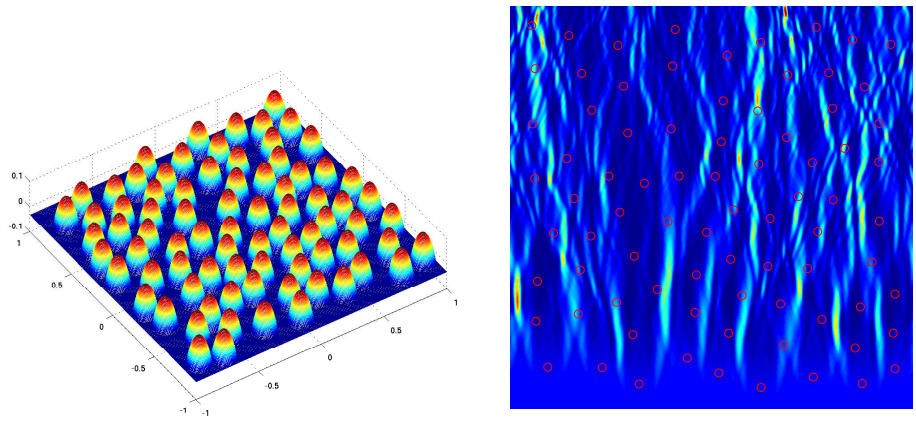

Figure 5: Left: Potential landscape given by spherical scatterers. Right: Branching of an incoming plane wave in the given potential [29]

types of scatterers are made to offer the possibility of studying weaker and stronger potentials. The sizes of the scatterers are given in figure 6 and their potentials in a colored 3d-plot in figure 7 revealing a much smoother potential than the one of the conical scatterers.

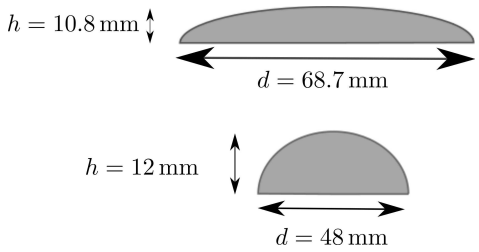

Figure 6: Geometry of the new scatterers, the upper one is defined as type II and the lower one as type I

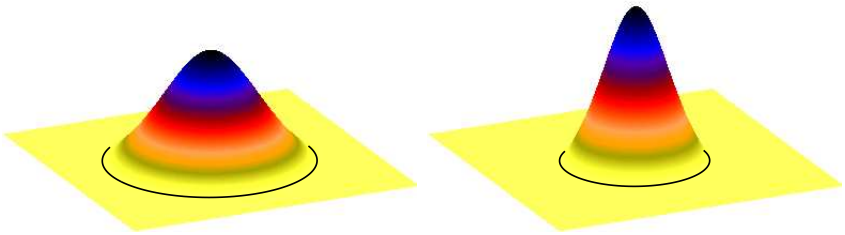

Figure 7: Potential corresponding to the new scatterers, left: type II, right: type I

5.2 The Measurement Table

As described above it was suitable to establish new scatterers with a weaker potential. Consequently the branching will appear in larger distances from the source and the former setup used by Ruven Höhmann with an accessible range of 340 mm x 240 mm turned out to be too small. In the former version the bottom plate with the scatterers was fixed and the top plate with a second antenna moved over the cavity. The disadvantages are then that the usable area of the bottom plate can only reach a quarter of the table size. Moreover the cavity is slightly perturbed by the movement of the plates.
The new setup is based on another principle: The top and bottom plates are fixed in a distance of 20 mm, but there are small holes in the top plate through which a thin wire antenna is inserted and extends 3 mm into the cavity. Before it was tested that these small holes do not affect the measurements, as their diameter is very small (2 mm) compared to the wavelength of $\approx$ 1 cm (at 30 GHz e.g.). The worst the quality factor of the billiard might be reduced a little, which is however not the limiting parameter in these

kinds of experiments on open cavities. A second antenna is positioned at $[0, 260]$ mm in the bottom plate, is teflon-coated and extends 5 mm into the cavity. Thereby transmission measurements can be performed. A side view of the cavity and the two antennas is illustrated in figure 8. The new table enables a measurement field of 1060 mm x 520 mm with a resolution of 5 mm. As the movement of the antenna must be very accurate not to miss the holes,

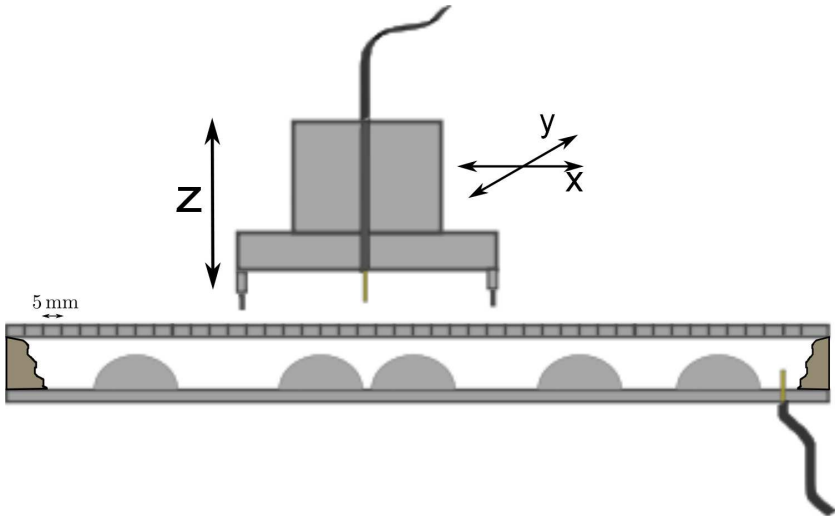

Figure 8: Side view of the cavity: One antenna (right) is fixed in the bottom plate, the other one (golden pin) is moved over the top plate and inserted through holes with a distance of 5 mm. The open ends of the cavity are surrounded with absorbers to avoid reflections at open ends. Inside the cavity the scatterers are distributed establishing a weak potential landscape

which are only 0.7 mm larger than the antenna's diameter of 1.3 mm, the lower part of the "elevator" is slightly flexible so that the two metallic pins to the left and the right (see figure 8) can guide the antenna into the hole. Then the whole elevator is pressed firmly on the plate to guarantee equal contact in all of the measurements. A photograph of the whole setup is presented in figure 9. The new table was already used for measurements of the Goos-Hänchen shift [30] and investigations of mixed phase spaces with a mushroom billiard [31]. For the measurements of the transmission spectrum we used a Wiltron 360B vector network analyzer (VNA) providing frequencies up to 40 GHz and a step width of 10 MHz. It offers access to the full scattering matrix of the system, the modulus as well as the phase of the measured signal as a function of frequency.

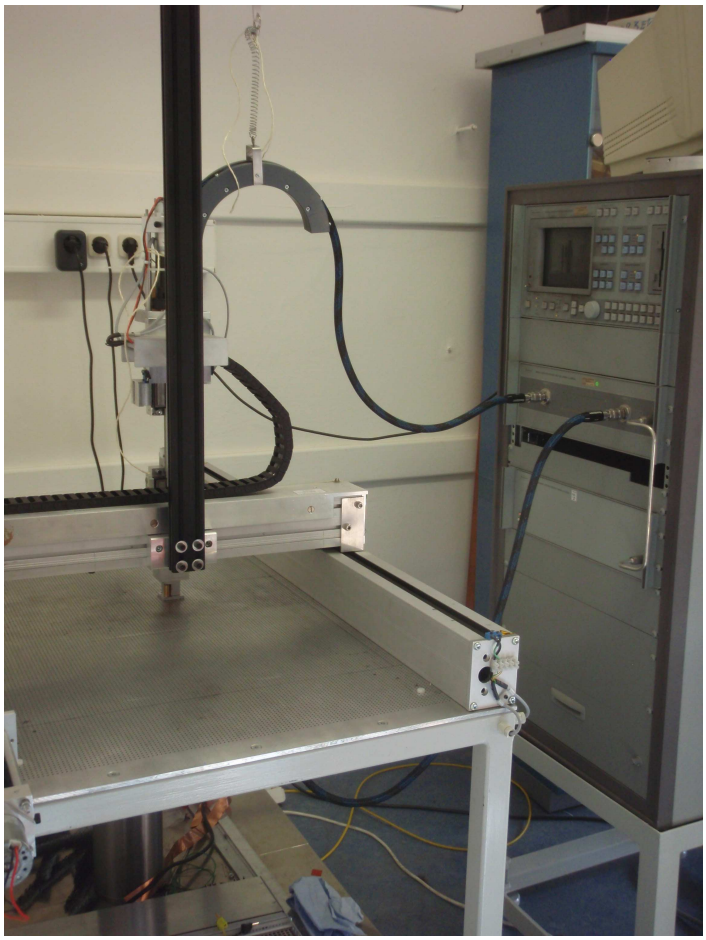

Figure 9: Photo of measuring table and vector network analyzer with two cables to the fixed and movable antennas

6 Results on Basic Measurements

6.1 Empty Cavity

To test the quality of the setup the empty cavity surrounded with absorbers but without any scatterers was measured. As the measurement of the full accessible area takes 8 weeks we restricted ourselves to a smaller field of $x \in [-95, 95]$ and $y \in [0, 250]$ and measured a frequency range of 15 to 35 GHz. The intensity of the wavefunction for different frequencies is presented in figure 10. As expected we observe the circular waves starting from

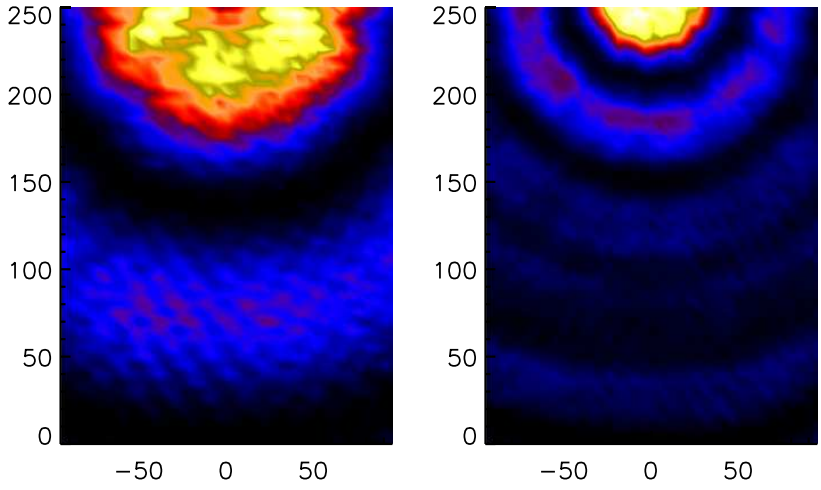

Figure 10: Two examples of wavefunctions (intensities) of the empty cavity at 15 GHz (left) and 25 GHz (right)

the fixed antenna slightly above the field at the position $[0, 260]$. We did not measure directly atop this antenna, as the two antennas would touch each other destroying any reasonable result. As already studied by Ruven Höhmann [26] we expect for the free wave propagation a superposition of Hankel functions for every open mode with the singularity at the source antenna. For frequencies less than 15 GHz there are only the TM_0, the TM_1 and the TE_1 modes open, from which only the first two can couple to our dipole antenna. Thus only the two are taken into account leading to a wave function of

$$\psi(r, \phi) = a_0 H_0(k_0 r) + a_1 H_1(k_1 r) \tag{6.1}$$

with wave numbers k_0 and k_1 for zeroth and first mode according to equation (2.6) and the complex coupling constants a_0 and a_1, which depend on

frequency. A fit of this equation to the data is shown in figure 11 revealing a good agreement with the assumptions. The higher the frequency the

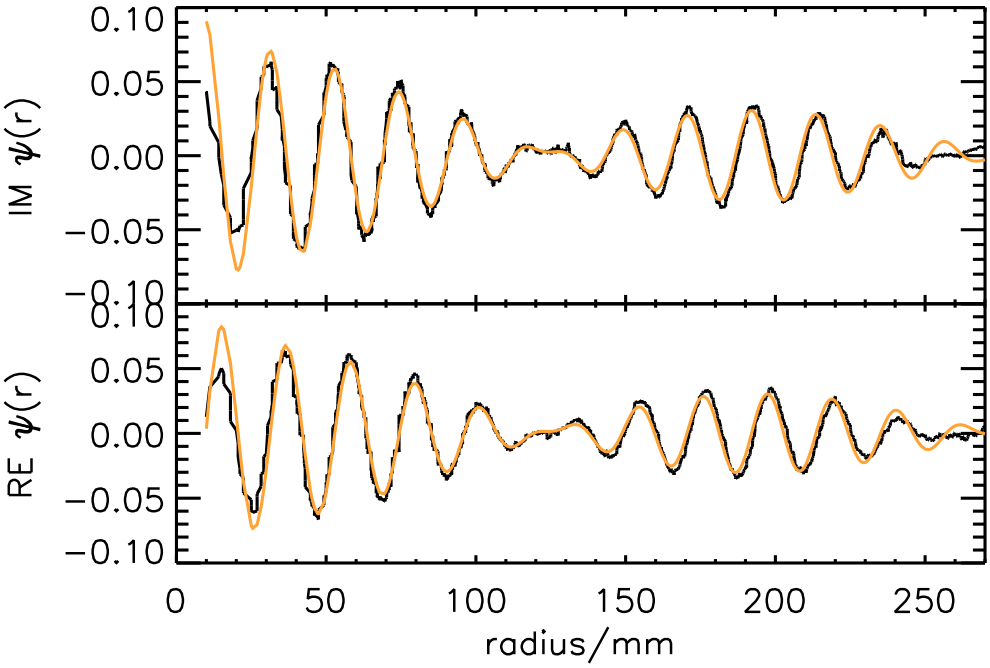

Figure 11: Radial dependent wavefunction at 15 GHz with fit corresponding to equation (6.1)

more modes are open and the more fit parameter appear in equation (6.1) which makes the fit much more sensitive on the starting parameters and thus reduces its reliability. Nevertheless it is shown that the coupling of the antennas, the absorbers and the measurement mechanism work suitable. A new feature, which was not investigated by Ruven Höhmann, is revealed by looking at the intensity of the wavefunction radial dependently, see figure 12. There are two obvious maxima with a distance of 149 mm, denoted by the arrow. The length corresponds to a frequency of 2 GHz, which is the difference between the two propagating frequencies of $\nu_0 = 15\,\text{GHz}$ and $\nu_1 = 13\,\text{GHz}$ revealing a beating between the modes, also seen in figure 11 (left). For higher frequencies and measurements with scatterers placed in the cavity the two modes do not only interfere with each other, but couple to each other by exchanging energy. This will be investigated in detail in section 7.3.

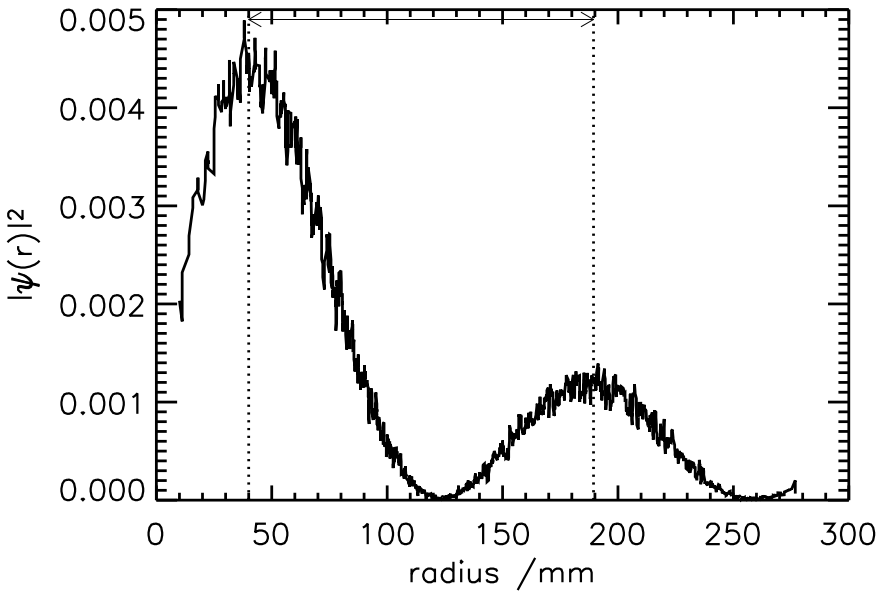

Figure 12: Intensity of radial dependent wavefunction averaged over all angles at 15 GHz. The distance between the two maxima is 149 mm (arrow)

6.2 Characterizing the Scatterers

With the next basis measurements small configurations of one or two scatterers are investigated to study their characteristics. Two examples of single scatterer measurements are presented in figure 13. It can be nicely seen that the circular wave starting at the source antenna is bent around the scatterers. In figure 13 (left) the wavefunction is symmetric around the vertical axis, in the right picture this symmetry is slightly perturbed. A reason for that might be an inaccurate placing of the scatterer or small differences in the absorbers. For focusing effects two scatterers are necessary: They are placed in a symmetric setup and I measured again the small field around them. The results are presented in figure 14. For both scatterer arrangements one can see again the circular wave coming from the source antenna, which is then perturbed by the scatterers' potential. A focusing along the vertical symmetry axis and an intensity enhancement behind the scatterers is found (see arrows). In comparison with classical and wave simulations (here the example for the scatterers of type II is shown in figure 15) we see caustic formation and intensity enhancement at the same positions. These results are also in agreement with the measurements by Ruven Höhmann:

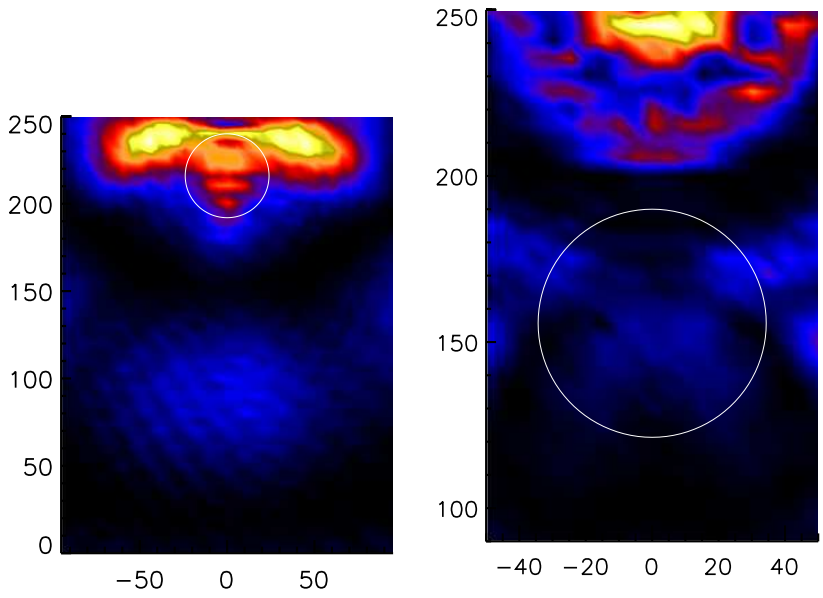

Figure 13: Wavefunctions (intensities) of one scatterer (type I) at 15 GHz (left) and of one scatterer (type II) at 27 GHz (right). Note the different field sizes. The one antenna is still fixed at $[0, 260]$.

Though he has used scatterers with a stronger potential the bending and the characteristics of the wave functions agree in both measurements. Now all the requirements for large scatterer arrangements are verified.

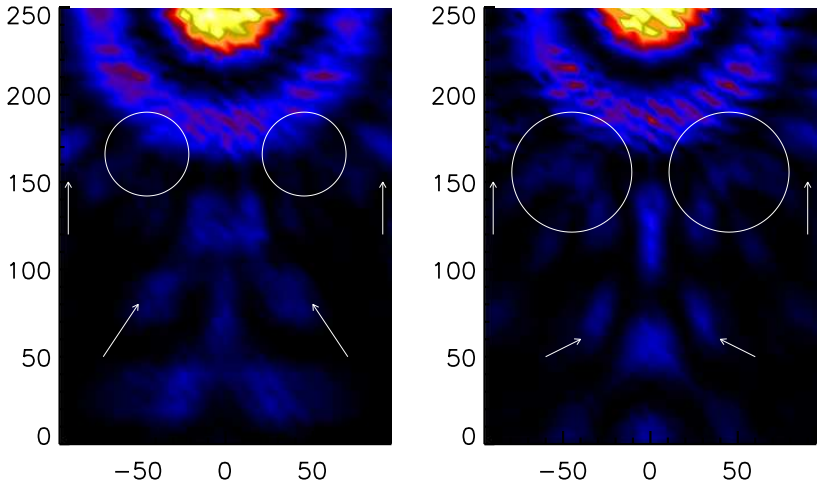

Figure 14: Wavefunctions (intensities) of two scatterers of type I at 25 GHz (left) and of two scatterers of type II at 25 GHz (right), the arrows mark the intensity enhancement according to the simulations in figure 15

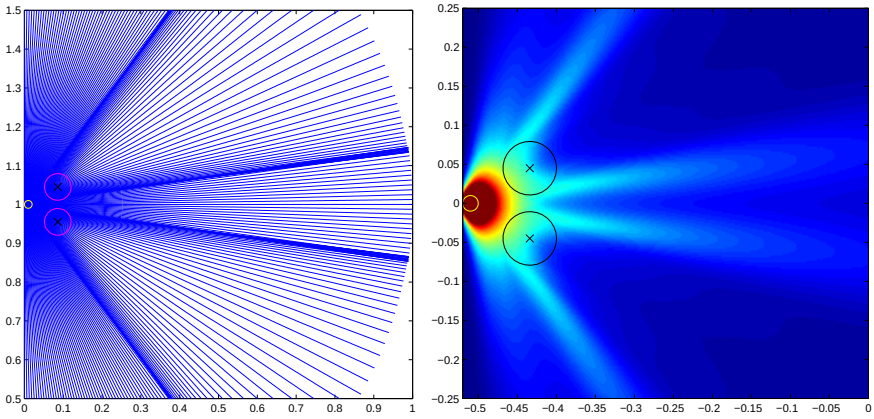

Figure 15: Trajectory density and wave simulation for the arrangement of two scatterers of type II, provided by Jakob Metzger. The labels are given in m.

7 Results on large Scatterer Configurations

7.1 Mode Filtering

In the following three different arrangements of scatterers are measured in the full accessible field.

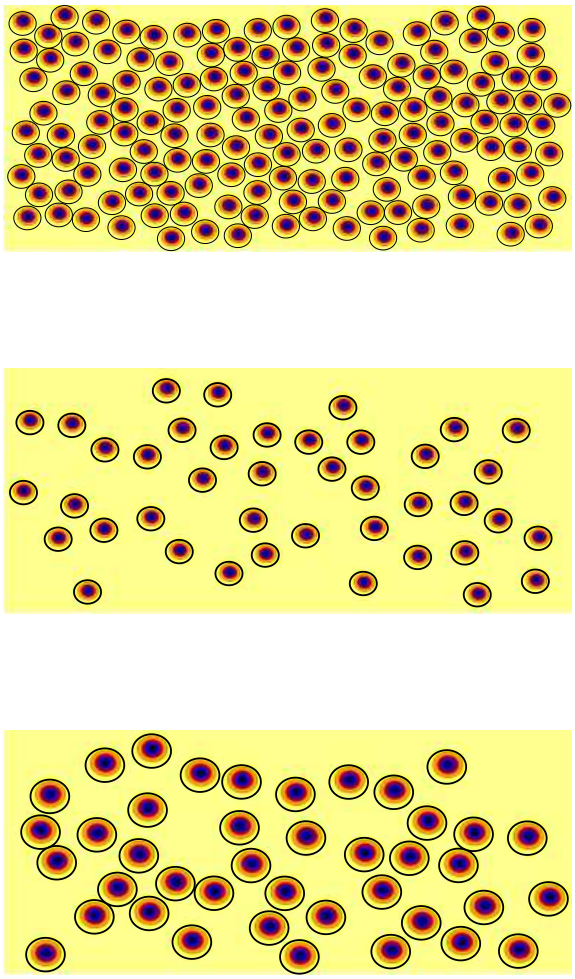

Figure 16: The potentials of configuration 1, 2 and 3 in a shade plot. The circles mark the border of the scatterers and the darker the color the higher the potential. Outside of the scatterers the potential is constant.

The potentials are presented in figure 16. For the first two configura-

tions the smaller scatterers (type I) are used, for the third one type II. On the basis of the data of configuration 2 the procedure of data analysis is described. Figure 17 shows this configuration and the wave function at 25 GHz. Figure 18 shows the radial decay of the wavefunction at 25 GHz, which was

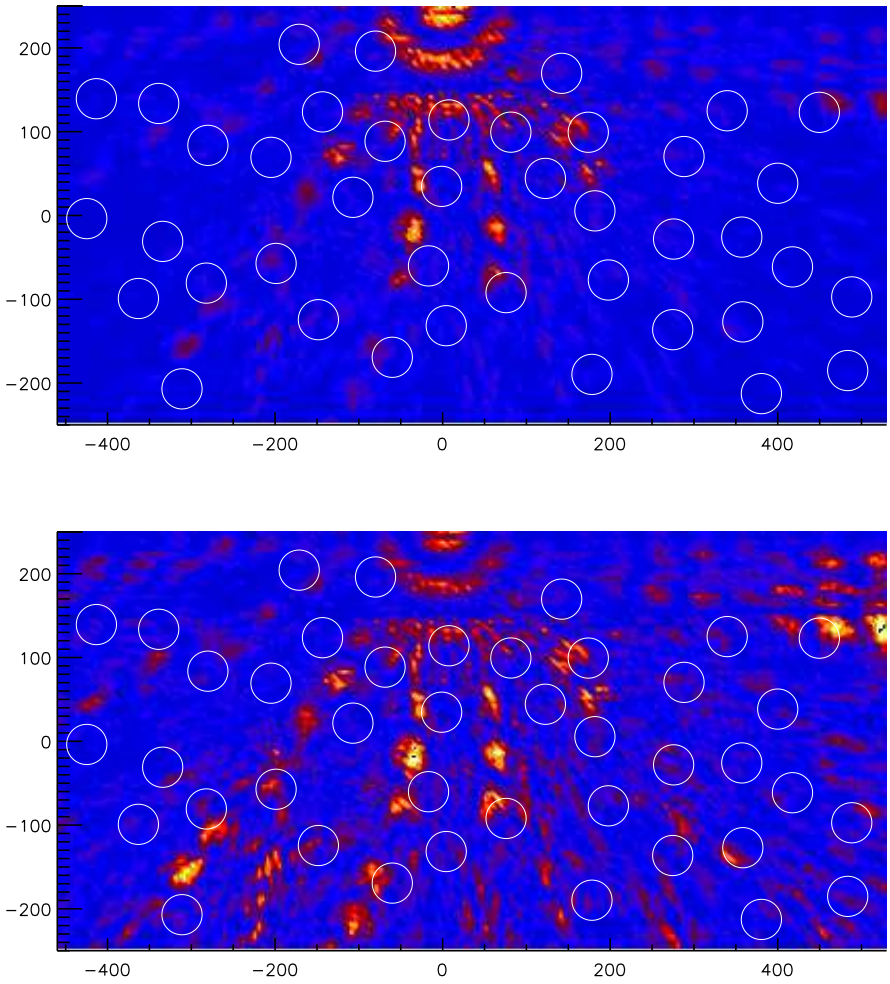

Figure 17: Wave function intensity at 25 GHz (upper panel) and the same where the exponential decay was removed (lower panel).

removed to obtain the lower panel of figure 17. From the theoretical point of view one would expect a $1/r$ decay for the intensity and this was also found in the simulations. Nevertheless already Ruven Höhmann found an exponential decay in his experiments. As a reason for it absorber effects or skin effects of top and bottom plate can be excluded, as the exponential

decay was only found in the large arrangements of scatterers and not in the empty cavity measurement. Another effect not accounted for in theory and simulation is the scattering between modes and the different coupling of the antennas to different modes. Thus a possible explanation of the decay is the scattering from the mode which is coupled strongest to the antenna into the other modes which couple weaker. Correspondingly the measured intensity decays exponentially with the distances from the source. Figure 17 reveals a

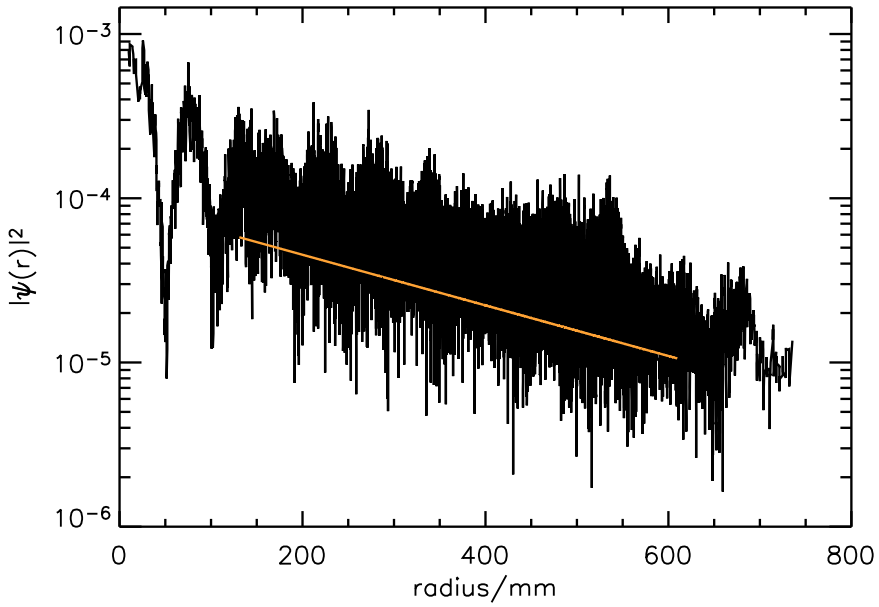

Figure 18: Radial Decay of the intensity of the wavefunction at 25 GHz with exponential fit (orange line). Only for the presentation the data was smoothed over 5 points

second deviation from theory: Again a clear beating with half a wavelength of $\approx 40\,\mathrm{mm}$ which corresponds to the frequency difference of $\Delta\nu = 3.8\,\mathrm{GHz}$ of the TM_1 and the TM_2 mode can be seen in the circular waves around the source. As neither the theory nor the simulation take into account several modes, but assume only one single propagating frequency, we have to filter the different modes to analyze them separately. A two dimensional fast Fourier transform (FFT) offers a possibility to identify the different modes, see figure 19. In the left part of the figure there are three clear circles at $\approx 20, 23, 25\,\mathrm{GHz}$ of speckles (inside the smaller black circle, in between the two black circles and outside of the larger black circle, respectively), the frequencies of the propagating modes TM_2, TM_1 and TM_0. Every mode is now

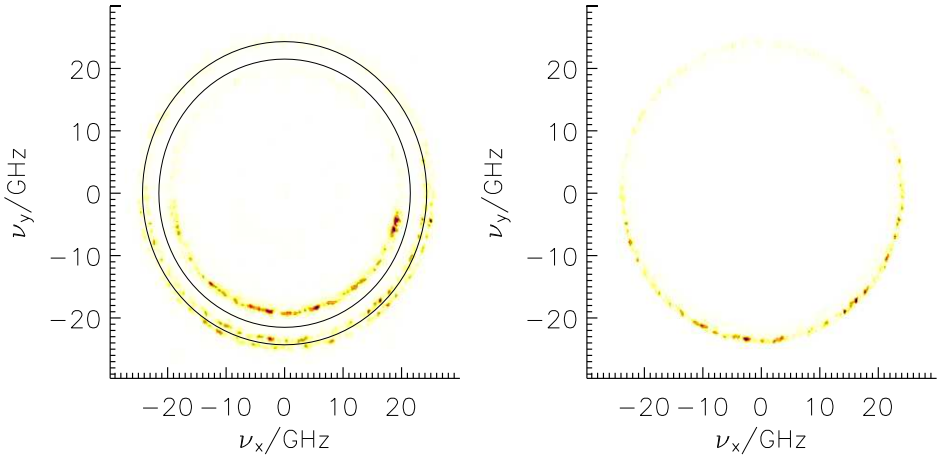

Figure 19: 2d FFT of configuration 2 at 25 GHz. The speckles between the plotted circles belong to TM_1. To filter this mode out all values outside are set to zero (right)

filtered out separately and transformed back. In the right part one can see that the lower half of the circle is much brighter than the upper half, showing that there is only weak back scattering and the assumption of the theory of a quasi-one dimensional dynamic in positive $\vec{r}$ direction is justified.
After separating the modes for every frequency the individual exponential decays $\propto \exp(a_1 r)$ are removed. The decay constant a_1 for the modes are plotted frequency dependent in figure 20. The values are in the range of -0.007 and $-0.001\,\mathrm{mm}^{-1}$ and thus the decay is slightly weaker as in the former experiment in which Ruven Höhmann found values between -0.009 and $-0.005\,\mathrm{mm}^{-1}$. As expected the new scatterers cause only weaker coupling of the different modes. Moreover the figure shows that the TM_0 (black), TM_1 (blue) mode are very similar to each other and define the overall decay (orange), while the TM_2 mode starts with a weak decay, which becomes stronger the higher the frequency is. The observation that even the TM_0 mode feels a potential and shows similarities to the first mode cannot be explained in the simple mode picture of equation (2.7) anymore. This picture assumes parallel top and bottom plate and thus a constant height. On this condition the separation of the z-coordinate is possible. If height variation up to first order is considered, additional source terms appear in the Helmholtz equation, which lead to a coupling between different modes (see appendix A).
Figure 21 shows that the filtering process was successful: Here the filtered TM_1 mode of the wave function at 25 GHz is shown. Now the beating is gone and the branches are much more pronounced than before. For all the further

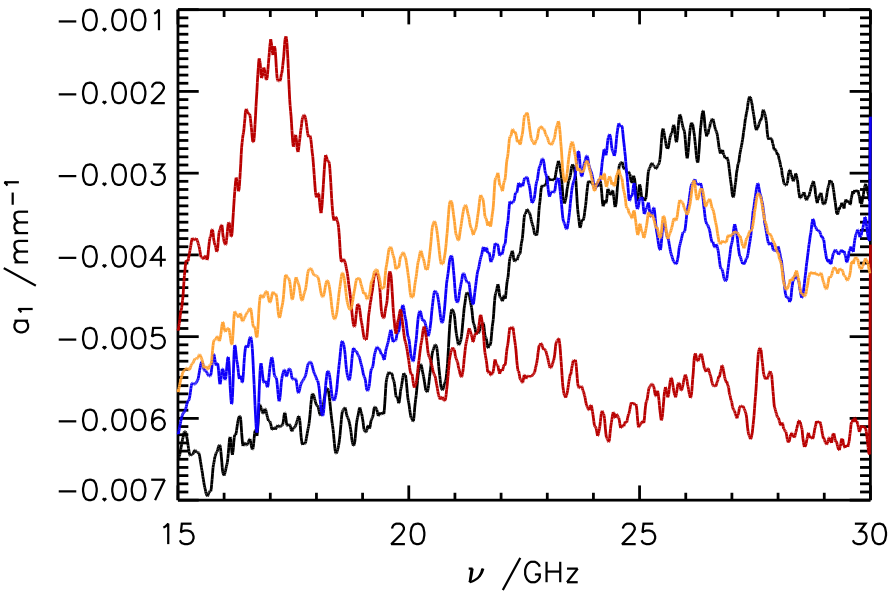

Figure 20: Decay constants for TM_0 (black), TM_1 (blue), TM_2 (red) and for the mixture of all modes before filtering (orange)

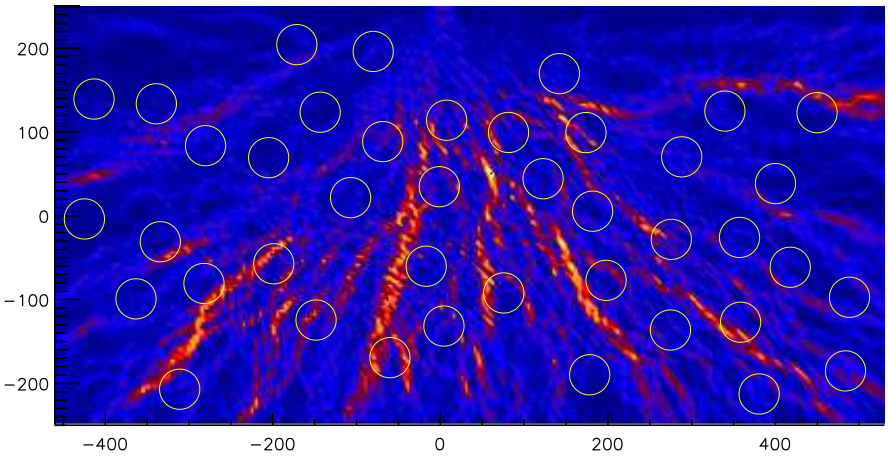

Figure 21: The same wavefunction as in figure 17, but only the TM_1 mode at 25 GHz (decay is removed)

investigations this filtered data is the basis.
In figure 22 the TM_0 mode for the same configuration and the same frequency

is plotted. Though this mode is supposed to be constant due to the simple mode picture (equation (2.9)) we observe not only strong intensity fluctuations but also a clear branching. This structure has striking similarities with the brightest branches in figure 21, the first mode in the same configuration. As according to equation (A.3) the TM_1 mode acts as an extra source term for the TM_0 mode this behavior becomes elucidated.

In the comparison between our measured wave pattern, the simulated wave

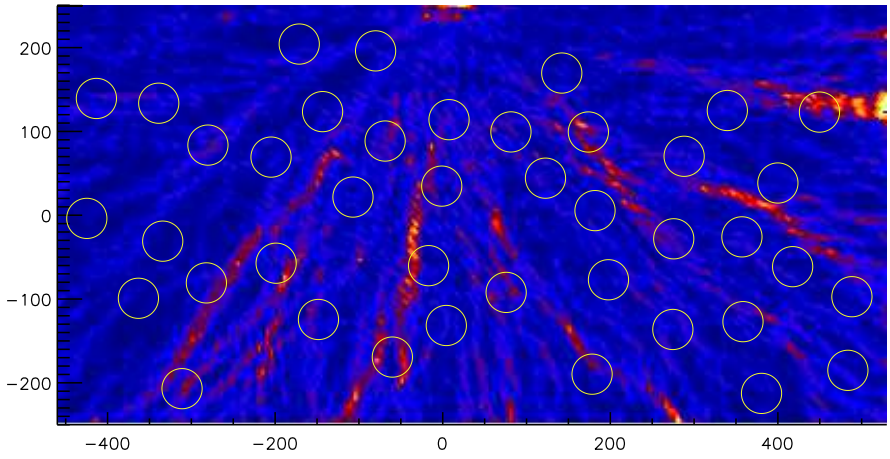

Figure 22: The same wavefunction as in figure 17, but only the TM_0 mode at 25 GHz (decay is removed)

pattern and the particle density calculated for the same potential the similarity between classical caustics and the (micro-)wave flow becomes convincing, see figure 23. The five main branches (see arrows) appear clearly in all three plots. The contours of the scatterers are marked by red circles to make it easy to identify the positions of the branches in all plots. The green circles indicates r_0, the occurring of the first branches in the wave plot. The plot of the classical density (lower left) shows that the first caustics appear directly behind the first disks at a distance around 150 mm. But this is not the distance of the highest intensity fluctuations in the wave plot (green circle). At that indicated distance several classical caustics converge or cross each other. The dependency of this position from the properties of the potential is presented next.

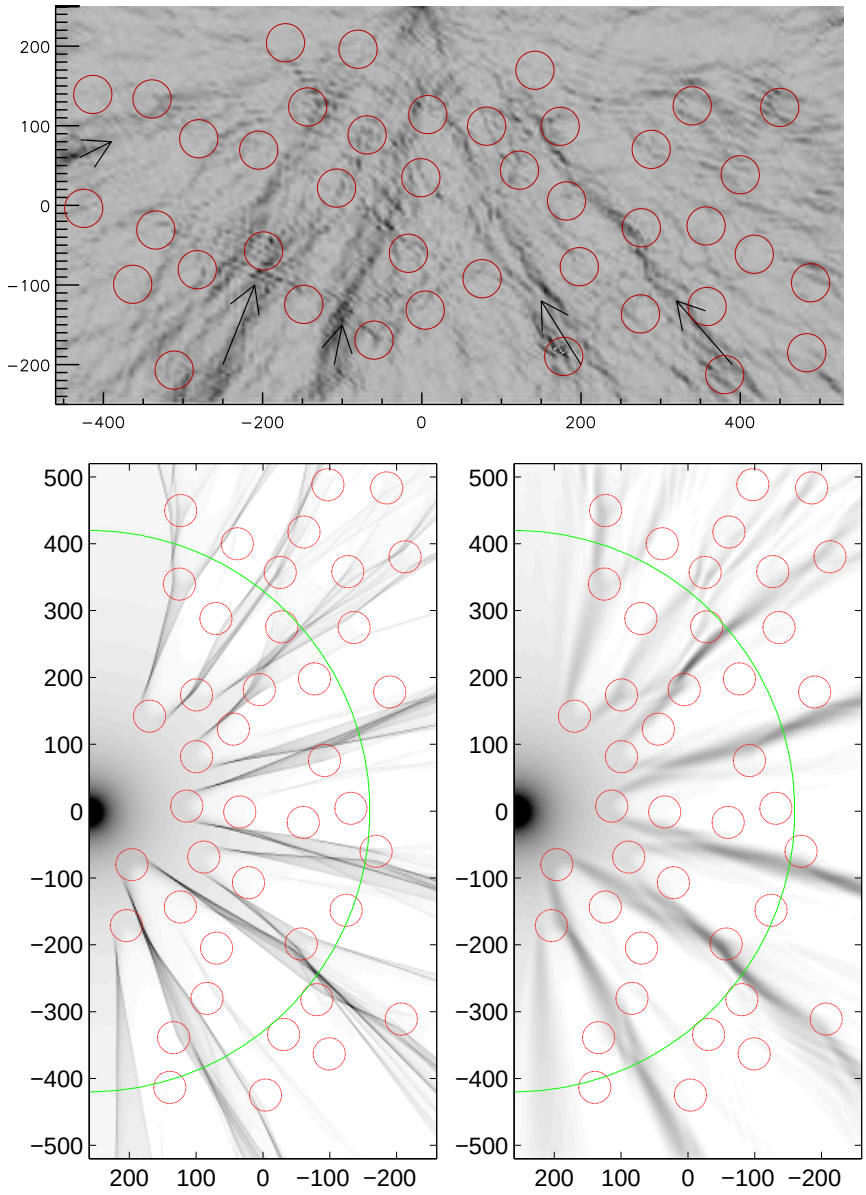

Figure 23: Measured wave function (upper) in comparison with classical ray dynamics (lower left) and wave simulations (lower right) for configuration 2 at 30 GHz and the TM_1 mode, the main branches are marked by arrows and r_0 by the circle (simulations provided by J. Metzger [29])

7.2 Correlation Function and Correlation Length

Equation (4.2) gives the scaling law for t_0 (i.e. a length r_0 in our case) depending on the standard deviation $\epsilon = \sqrt{\langle V(r)V(r)\rangle}$ and the correlation length l_c

of the potential. In a Gaussian correlated potential there is only one length scale, but in this experimental realization there are two: the radius of the scatterers and their mean distance. Thus I calculate the correlation function and fit a Gaussian decay to the first points. From this fit the correlation length is extracted according to equation (4.1). Figure 24 shows the correlation functions for the three scatterer configurations and the Gaussian fit (orange). As the potential for the second mode differs only by a factor of $n^2 = 4$, which does not play a role in the normalized correlation function, only the calculations for one mode are shown. In the beginning the decay

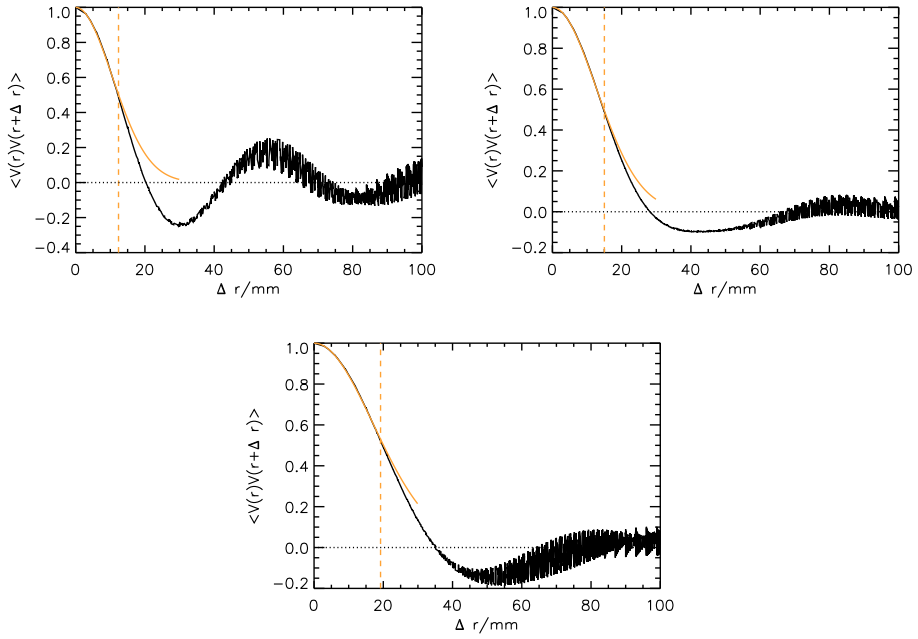

Figure 24: Correlation functions for the three configurations 1,2 and 3 (from left top to bottom) and a Gaussian fit to the starting of the decay, where only the data to the left of the vertical dashed orange line has been used in the fit. The horizontal dotted line marks the zero position to emphasize the undershoot.

of the correlation is well described by a Gaussian (with fixed amplitude 1 and mean of 0). The fit range takes all the values of the correlation function into account, which are greater equal to 0.5. It was checked, that the fitting parameters did not depend sensitively on small changes in the fitting range. The extracted correlation lengths are given in table 1. They turned out to be smaller than the scatterer radii of $r_1 = r_2 = 24\,\text{mm}$ and $r_3 = 34.34\,\text{mm}$. It is worth mentioning that the first two configurations turned out to have dif-

ferent correlations lengths, though the same scatterers were used. Probably the undershoot caused by the self-avoiding of the scatterers, which cannot be placed overlapping, leads to a compression of the first decay. In configuration 1 this undershoot appears much earlier ($\approx 30\,\mathrm{mm}$) as in configuration 2 ($\approx 40\,\mathrm{mm}$), as here the scatterers are placed much denser ($309/m^2$) as in configuration 2 ($83/m^2$). Thus the compression effect might be stronger in the first case leading to a steeper decay and a smaller correlation length.
The standard deviations of the potentials for the different modes and the energies of the propagating waves, by which the potential is normalized, are given in table 1, too. The theoretical model assumes a weak potential, not

Configuration	$l_c/\,\mathrm{mm}$	$\epsilon/\,\mathrm{m}^{-2}$	$k_{xy}/\,\mathrm{m}^{-1}$	ϵ/k_{xy}^2
1 (mode 1)	14.91	33049.0	608.8	0.089
1 (mode 2)		132196.0	544.6	0.446
2 (mode 1)	17.88	19951.1	608.8	0.054
2 (mode 2)		79804.5	544.6	0.269
3 (mode 1)	24.10	19559.5	608.8	0.053
3 (mode 2)		78237.9	544.6	0.264

Table 1: Correlation lengths, standard deviations of the different potentials and the wavenumbers of the propagating waves (exemplary for 30 GHz)

reaching more than 12% of the particle energy. In the experiment strictly speaking only the TM_1 mode meets this requirement, see fifth column of table 1. Nevertheless we will also analyze the TM_2 and see what we can extract from it. The TM_0 mode was not investigated further, as it is supposed to be constant and no clear potential shape can be assigned to it.

7.3 Mode Coupling and Scaling Behavior

One intention of these experiments is the investigation of the distance between source and first appearance of branching. As the wave function plots still include some noise and speckles it is not easy to extract the position of the first branching from there. It turned out that the variance of amplitude values $A(r, \varphi)$ on circles in dependence of the radius r is a reliable quantity to extract the t_0.

$$\mathrm{Var}(r) = \frac{1}{N-1} \sum_{j=0}^{N-1} \left[A(r, j\Delta\varphi) - \langle A(r, \varphi) \rangle_\varphi \right] \tag{7.1}$$

In figure 25 the perfect agreement between the prominent peak in the variance and the occurring of the branches is shown for simulations.

For the comparison of the variances of the simulation and the experiment the

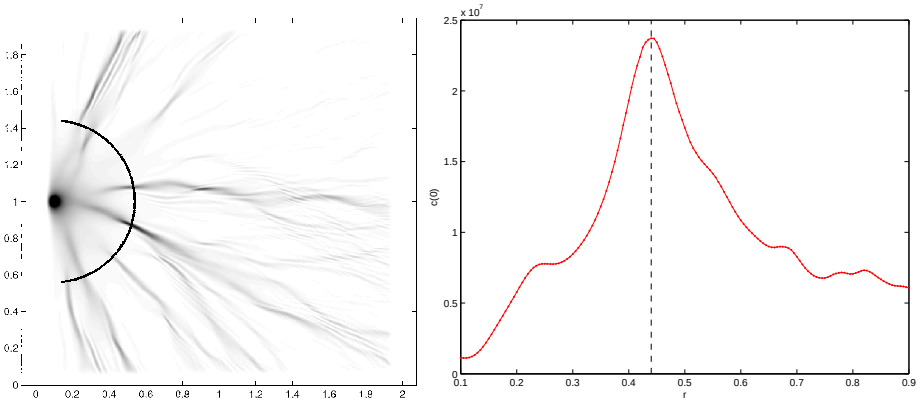

Figure 25: Simulation of a flow in Gaussian correlated potential (left) and the variance Var(r) corresponding to equation (7.1) with radius r [m] (right). The vertical line corresponds to the distances indicated by the circle in the left picture, where the first branching occurs, provided by J. Metzger [29]

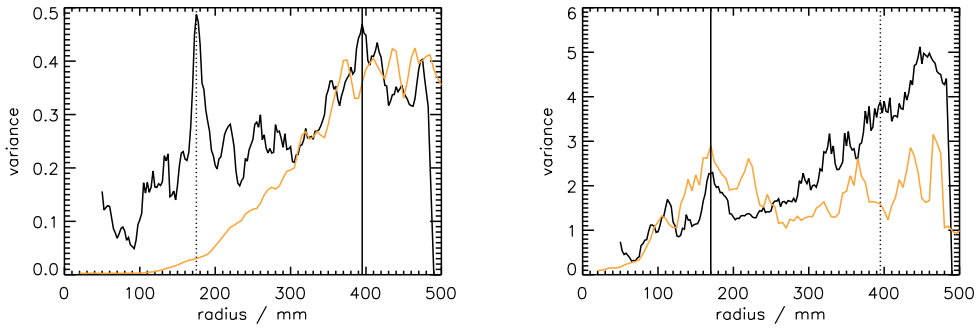

Figure 26: Variance Var(r) of TM_1 mode (left) and TM_2 (right) at 30 GHz with data from the simulation (orange), the solid vertical lines each indicate the peak expected for the mode and the dotted lines the peak caused by mode coupling to the other mode

$1/r$ decay was removed from the calculated data and the exponential decay from the measured data. To reduce the influence of noise in the experiment an average over 5 points in radial direction was performed. Due to this average the small speckles (see e.g. upper panel in figure 23) loose their influence while branches, which follow approximately this radial direction, have an enhanced impact. Figure 26 includes the experimental (black) and the numerical (orange) variance for configuration 2. For the main peaks at

$r_0 = 395\,\mathrm{mm}$ (left) and $r_0 = 170\,\mathrm{mm}$ (right) we find an agreement between experiment and simulation. Also in the wave function (figure 27) the solid circles (corresponding to the solid lines) indicate a distance of large intensity fluctuations. But here again the impact of mode coupling becomes crucial: In

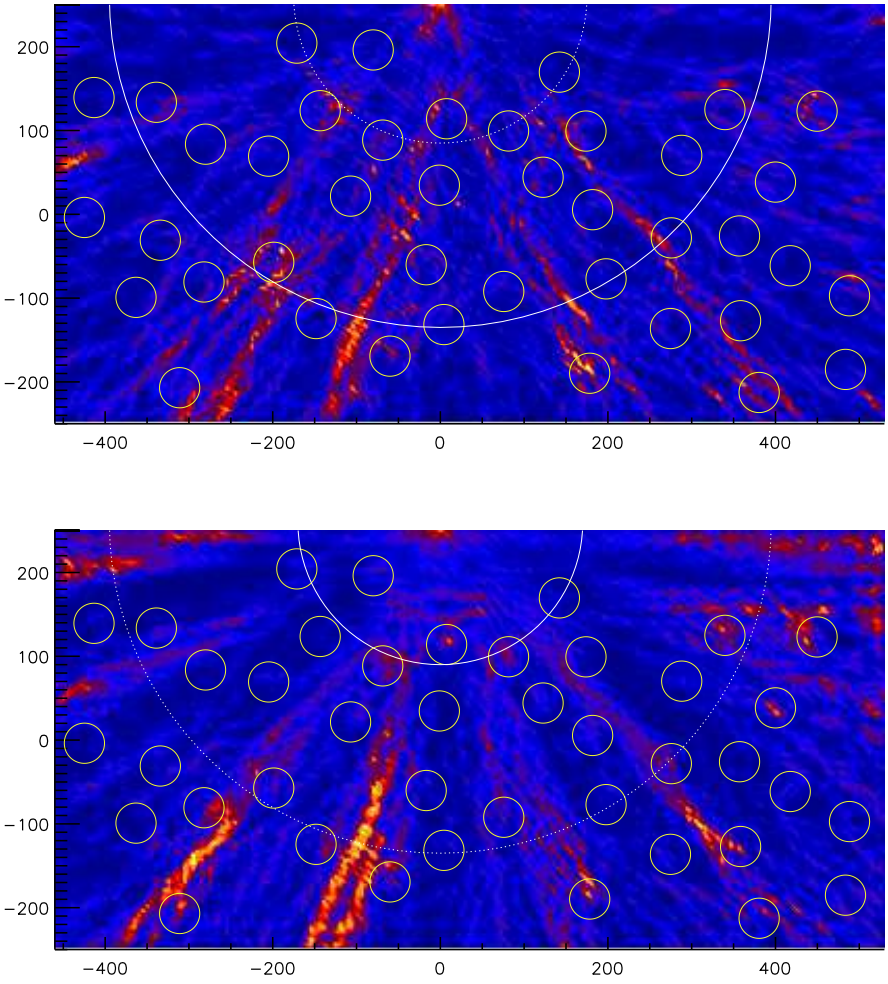

Figure 27: Wave function of TM_1 mode (upper panel) and TM_2 (lower panel), the circles corresponds to the distances indicated in figure 26

the variance pictures the peak of the other mode occurs, in the wave pictures we observe additional branching belonging to the other mode. In other words the wave of TM_1 acts as a source term for TM_2 and the other way round. Equation (A.3) reveals this effect exemplary for the TM_1 and TM_0 mode. A similar behavior was also found in the other measurements.

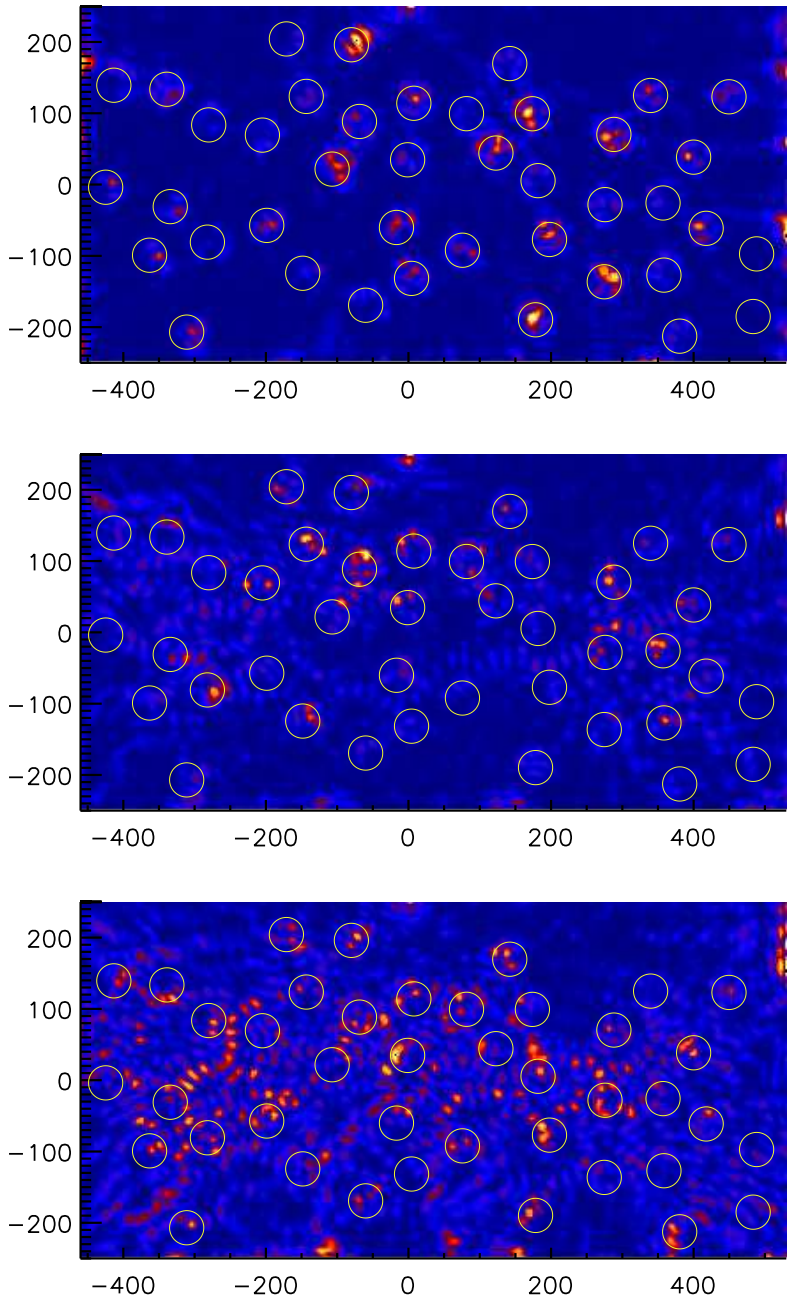

Figure 28: Wave functions of TM_2 mode at the frequencies $\nu = 15.5,\ 17.5,\ 18\,\mathrm{GHz}$ (from top to bottom) of the second configuration

Other interesting dynamics occur at frequencies, at which a certain mode just opens, e.g. the TM_2 mode at 14.99 GHz. The corresponding wave func-

tions for different frequencies starting at 15.5 GHz are presented in figure 28. When the mode is just open (upper panel) its intensity is only distributed over the centers of the scatterers. At frequencies around 17 GHz the pattern starts to leave the scatterers (middle panel). Here the transversal wave vector (k_{xy}) holds an energy of 8.02 GHz. At $\approx$ 18 GHz larger patterns over the entire field are formed, the energy of the transversal wave reaches 10 GHz. According to equation (A.3) the potential, strictly speaking the derivatives of the potential, are part of the source terms and influence the coupling between two modes.
Nevertheless it is surprising, that the wave functions are that strongly located on the scatterers even though the TM_2 mode opens already at 14.99 GHz. This observation suggest, that the approximation of perfect mode decoupling and sharp cutoff frequencies is not sufficient to explain the wave pattern near the cutoff frequencies. Here the higher order terms inducing the mode coupling seem to become dominant. Furthermore one has to keep in mind, that even in the approximation of perfect mode decoupling the transversal wave lengths are approximately 80 mm for 15.5GHz. Accordingly one would not expect a completely free propagation in the scatterer free region, because the scatterer distances are often smaller than half a wavelength. The energy can thus travel much easier through the potential via the TM_0 and TM_1 modes and then couple back to the TM_2 mode at points, where the height variations, i.e. the coupling terms, are strong.

Due to the mode coupling the extraction of the correct peak in the variance plot for different frequencies, modes and potentials was not unambiguous, as in every plot more than one peak occurred as it is observed in figure 26. As discussed above the peaks of two different modes appear in the plots, thus only the peak in the expected range was considered for the scaling analysis. The results are presented in figure 29. The peak positions r_0 were rescaled with the extracted correlations lengths l_s, see table 1, and the standard deviation of the potential ϵ was scaled with the particle energy k_{xy}^2. For the first configurations (upper left) the frequencies 30 and 25 GHz with first and second modes and 20 and 16 GHz with the first mode (second mode did not show clear peaks) are taken into account. The blue line is a line fit with a standard regress routine giving an exponent of -0.54 and a χ^2-error of 0.005. In the fit the first data point was neglected. The orange line marks the expected exponent of $-2/3$. In the second configuration (upper right) the frequencies 30 GHz (first and second mode), 25 GHz (first and second mode), 20 GHz (second mode) and 16 GHz (first mode) are analyzed, resulting in an exponent of -0.50 with a χ^2-error of 0.042. In the third case (lower left) all 5 frequencies with both modes could be evaluated. Here I found an exponent

of -0.60 with a deviation of $\chi^2 = 0.016$. The last plot shows all the analyzed data points and an exponent of -0.56 ($\chi^2 = 0.060$). We observe a scaling

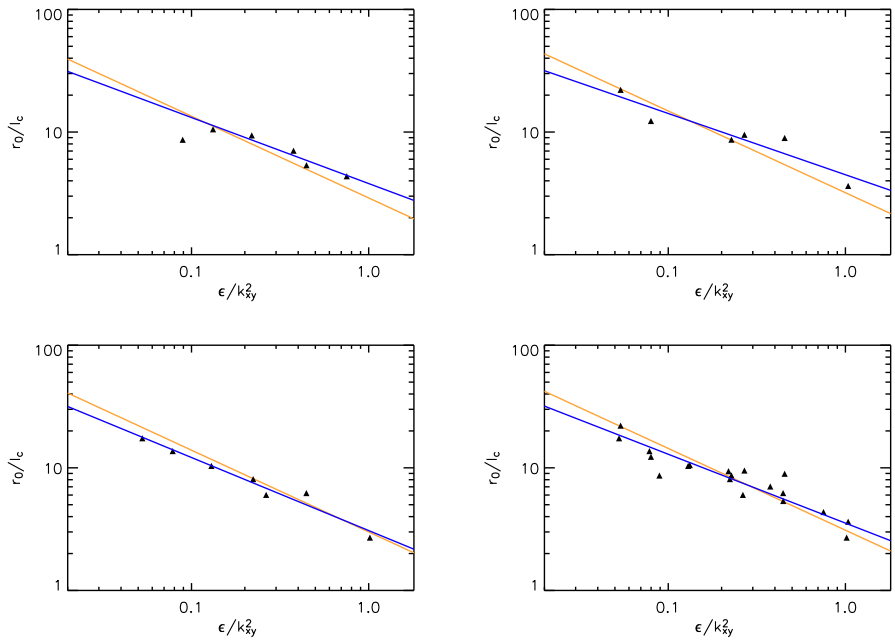

Figure 29: Scaling behavior of the peaks in the variance curves for the configurations 1 (upper left), 2 (upper right), 3 (lower left) and all together (lower right). The blue line is a line fit to the data points and the orange line indicate the exponent of $-2/3$

behavior of the branches, compatible with the predicted exponent of $-2/3$ (orange line). The small deviations can be explained by the difficulties of extracting the correct peak in the variance pictures. Also the curves of the simulations do not show one single dominant peak, but some noise and oscillations, which is even stronger in the experimental data. Moreover the mode coupling complicates the identification of the correct peak and influences the peak positions with respect to their theoretical value. The effect of random speckles causing the noise in the variance curves was reduced by the averaging in radial direction, but has unfortunately still some disturbing influence on the data. Additionally one must have in mind that the used potentials are not Gaussian correlated in strict sense. The influence of two different length scales is not investigated theoretically, yet. The data points belonging to the TM_2 mode are even not supposed to fit the exponent as they do not fulfill the assumption of a weak potential, see values in table 1. Nevertheless the last plot in figure 29 includes all identified peaks in the variance plots of the two

modes and shows a clear trend following the fit (blue line), but is described almost as good by the orange line, indicating the theoretical exponent. Thus we have shown a reliable consistency between our experimental data and the theoretical scaling assumptions, even in a larger range than expected.

Part II
Sound Waves

8 Motivation

In 2008 Ruven Höhmann et al. performed measurements on "Freak Waves in the linear regime: a microwave study" [23]. They measured the transmission of waves traveling through a random potential built with metallic cone scatterers in a quasi-two-dimensional resonator. The scatterers were randomly distributed in the microwave cavity. At high frequencies branching structures in the flow were found, which were the basis for the investigations in part I. In the lower frequency regime the wave height distribution was analyzed. Here large deviations from Rayleigh's law, a prediction of the random plane wave model, were found [25]. From the measured wave patterns ψ_i in the frequency regime many propagating waves were calculated by a superposition of the measured patterns including a random phase according to

$$\psi(\vec{r},t) = \sum_{i=1}^{N} \psi_i(\vec{r})\ e^{i(2\pi\nu_i t - \varphi_i)} \quad , \tag{8.1}$$

where $\psi_i(\vec{r})$ is the measured wave pattern at frequency ν_i and φ_i is a random phase. Performing the time average of the wave intensities at a fixed position $\vec{r}$ a Rayleigh distribution was found. But the local time-averaged values $s = \langle I \rangle_t$ were not equal, but χ^2_n-distributed. So the overall intensity distribution was thus given by the compounding of the two distributions

$$P(I) = \int_0^\infty ds\ P_{loc}(I,s)\ g(s) \tag{8.2}$$

where the local intensity distribution is given by the Rayleigh distribution [32]

$$P_{loc}(I,s) = e^{-I/s}\ s^{-1} \tag{8.3}$$

with $s = \langle I \rangle$ and the distribution of s by a χ^2-distribution

$$g(s) = \chi^2_n(s) = \left(\frac{n}{2}\right)^{n/2} \frac{1}{\Gamma(n/2)}\ s^{n/2-1}\ \exp\left(-\frac{ns}{2}\right) \tag{8.4}$$

Performing the integration one obtains a K-distribution

$$P(I) = \frac{n}{\Gamma(n/2)}\ \left(\frac{nI}{2}\right)^{n/4-1/2}\ K_{n/2-1}\left(2\sqrt{\frac{nI}{2}}\right) \tag{8.5}$$

and found a good agreement of fit (red curve) (with 8.5) and the experimental values, see red crosses in figure 30. Thus also the time-dependent waves

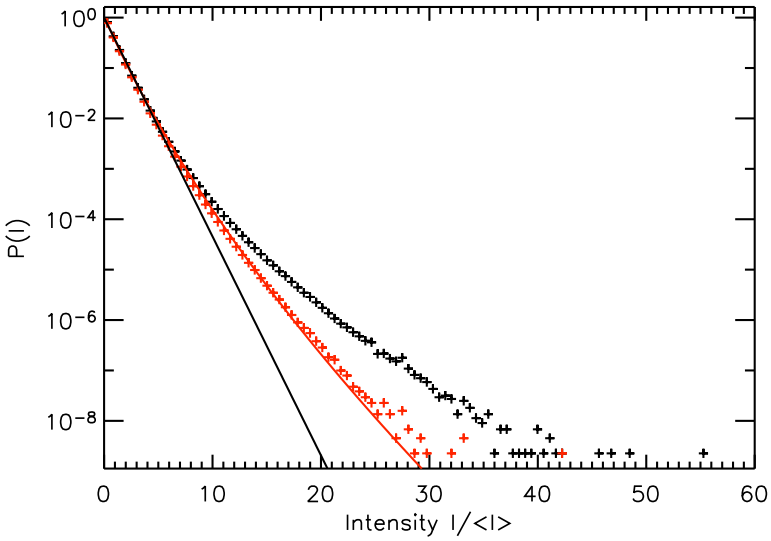

Figure 30: Overall experimental intensities (black crosses) with Rayleigh (black curve) and K-distribution (red curve) and experimental data without extremest events, the hot spot, (red crosses) (figure taken from [26])

showed a non-Rayleigh behavior with a large increase of the probability to find high intensities. Only the extremest events, the so called hot spots, could not be included in this description (black crosses). The fit value of n, the degree of freedom in the χ^2 function, was in the range between 30 and 35, compared to $N \approx 150$ superimposed wave patterns (see equation (8.1)) depending on the realization. Thus the pulse components are in part correlated. The idea of the compounding of a χ^2 and a Rayleigh or normal distribution (either for intensity of amplitude) is also found in a complete different context. Münnix et al. investigated correlations in credit risks using random matrix theory and found again a K-distribution for the averaged price distribution in a credit portfolio with correlations resulting from the compounding of χ^2 distributed variances and a multivariate normal distribution for the prices [33].
Based on these observations a new measuring idea was developed: To get direct access to time-dependent waves without going the long way round on frequency dependent measurements, we came up with performing measurements on sound waves. The abstract idea of waves traveling through a random potential (with correlations) should be projected on a turbulent

air stream, replacing the potential, and sound propagating through it. It is similar to White and Fornberg's idea, that freak waves in the ocean are caused by random currents [24]. We expect the turbulence pattern to be stationary for a small time, in which the sound waves will be influenced. After a short time the actual turbulence flow changes which will lead to a different modification of the traveling sound waves. Thus the fixed position measurements of the microwaves are translated into small time windows, in which the sound is recorded. This way of experiments was completely new terrain in our group, but we wanted to find out if those measurements were realizable with a reasonable effort. As no estimations on the turbulence-sound-interaction were available, we did not know in advance, what sampling rate, sound frequency were needed to sample the potential, i.e. the vortices in the air stream. Consequently we follow the experimenter's way to find out how far to come with a low-cost equipment and the simple model. That meant to start with cost-efficient standard sound equipment like sound card, microphone and loudspeaker in the audible frequency regime, instead of spending much more money on e.g. faster ultrasound setups. The aim of this experimental approach was to test if the idea of stationary vortex pattern for short times and K-distributed intensities for long time can be observed with this standard equipment. In the end it turned out that in the accessible parameter range these effects were not observable. For the transfer between the microwave experiment and the acoustical setup a more detailed theoretical background is mandatory. Nevertheless all the detailed experimental approaches are documented and discussed in the following.
The next sections are organized as follows. First the basis measurements with the simplest, already present equipment are presented in section 9. Based on the first result the new setup was developed and the data analyzing methods were improved, see section 10. Using the new setup and methods more test measurements were performed and studied, revealing other problems. To solve these problems the entire setup was moved into a professional wind tunnel in Oldenburg, where the main measurements took place. The corresponding findings are presented in section 11.

9 Measurements without external Sound Generation

For the first measurements we used a standard fan and a cheap table microphone to record the sound. The fan has 3 velocity steps corresponding to three different revolutions per minute presented in table 2, measured with a light barrier instrument. As the fan has 3 blades there are 3 light interruptions (counts of the instrument) per rotor revolution. A photograph of

fan level	light interruptions p.m.	Rotor Frequency ν_{rot} [Hz]	$\nu_{\text{rot}} \cdot 3$ [Hz]
1	2030 ± 10	11.28	33.83
2	2800 ± 10	15.56	46.67
3	3320 ± 10	18.44	55.33

Table 2: Data values of the fan

this setup is presented in figure 31. A typical recorded sound signal $A(t)$ in a small time range is presented in figure 32, where the time development of the recorded amplitudes in arbitrary units is plotted.

The entire signals last around 50 s including many rotor rotations leading to

Figure 31: Experimental setup with fan, microphone and Laptop

a sufficient statistic. We are convinced that the turbulence patterns change several times during this period. One problem are too high amplitudes, which

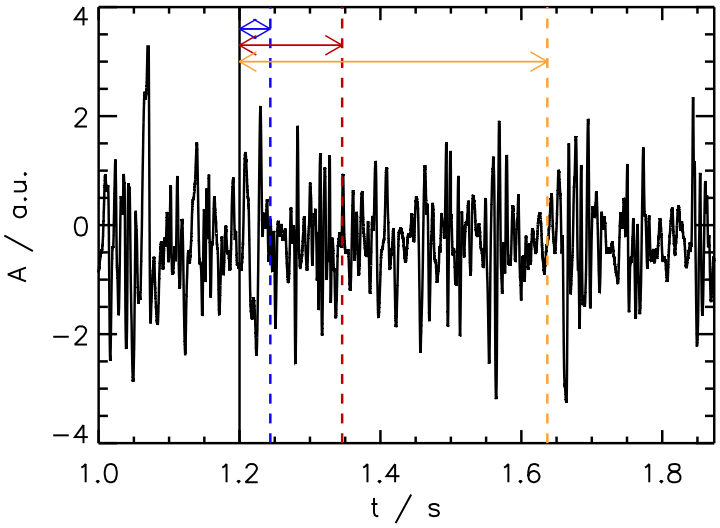

Figure 32: Detail of a typical recorded signal (fan level 1); amplitude in arbitrary units, small time range; the vertical lines and the arrows mark different time windows used for the investigation of the intensity distributions, see figure 34

exceeds the digital resolution of the sound card of 2^{16} amplitude levels giving access to amplitudes from -32768 to 32767 a.u. Thus amplitudes exceeding these limiting values are filtered out of the signal for further analysis. For first investigations the overall intensity distribution of $I = A^2$ is plotted, normalized by the mean intensity $\langle I \rangle$, shown in figure 33. We find an agreement with the K-distribution corresponding to equation (8.5) and $n = 2$ (red line). The agreement takes place over 3 orders of magnitude within the accessible intensity range. The small deviations in the tail are surely caused by a lack of statistic for those large events. But $n = 2$, which is the degree of freedom in the χ^2 function, is unexpected small.
Nevertheless we checked the other assumptions coming from our basic model: The intensity distribution of a time window, which is short enough that the turbulence configuration is stable, should lead to a Rayleigh distribution with a decrease changing from window to window. These decreases s (e.g. the local mean value) should follow a χ^2 distribution. How long those small time windows are supposed to be is not evident. On the one hand side enough data points are needed to obtain a proper statistic including the tails. On the other hand we do not want to average over several turbulence patterns. The identification of the correct timescale during which the vortex patterns

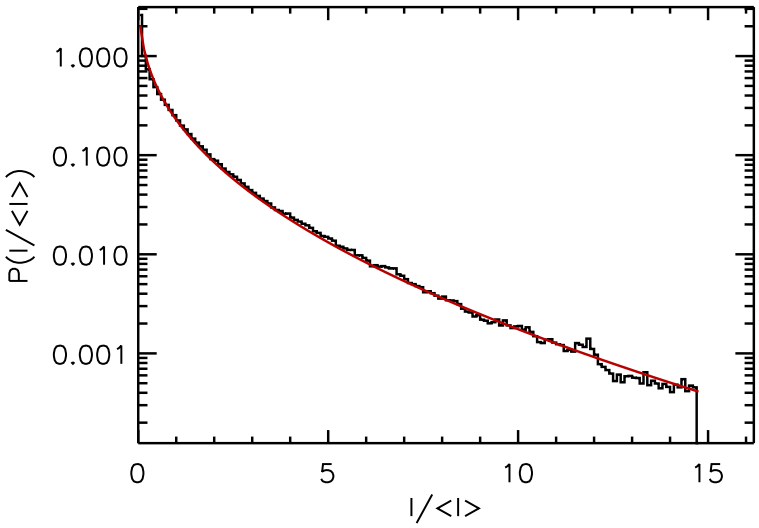

Figure 33: Intensity distribution of the same measurement as in figure 32 (black histogram) and in red equation (8.5) with $n = 2$

remain stable is the challenge of the data analysis. In the microwave experiments this separation is undisputed, because instead of a time separation a well-defined separation of (antenna) position appears. The distributions for different window lengths are shown in figure 34. We cut the full signal with a length of 43.69 s and 2093481 data points in 100, 300 and 1000 sub-windows of length 0.436 s (20934 points), 0.146 s (6978 points) and 0.0436 s (2093 points), respectively, to find out in which time range the expected Rayleigh behavior can be found. These window lengths are indicated in figure 32, all three starting at the black vertical line stopping at the blue or red or orange line, respectively. The problem is that for too short windows local structure destroys the idea of random fluctuations resulting in large deviations from the Rayleigh law (blue line) in figure 34 (a). Furthermore the number of points is quite small for statistical analysis. For the second case (b) the overall decay seems to agree quite convincingly with Rayleigh's prediction (blue line), but several oscillations on the histogram are revealed. This shows that there is still local structure resolved which is not averaged out. Also for the longest window, where many signal oscillations are included per window, the agreement is not better, as the distribution does not start at 1 but is already arched there and might already follow a K-distribution better than the plotted Rayleigh distribution (blue line). In the limit of sub-window length of the same order as the full signal length we expect the K-distribution of figure

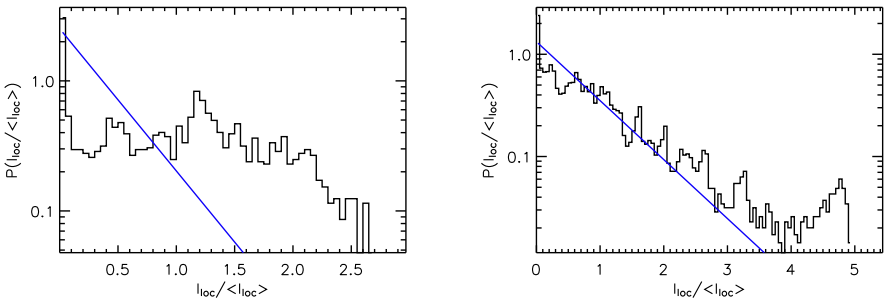

(a) length = 0.0436 s

(b) length = 0.146 s

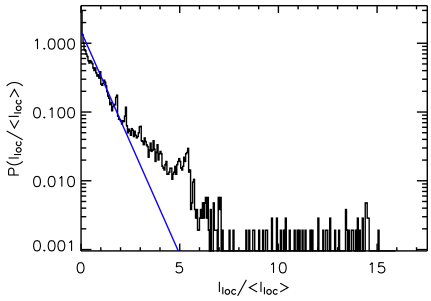

(c) length = 0.436 s

Figure 34: Examples of local intensity distributions of different time windows with Rayleigh law (blue lines) corresponding to equation (8.3) with fixed slope $\langle I \rangle$

33 to reappear, pointing out that the chosen sub window length of 0.436 s is already too long to resolve stable turbulence patterns. Nevertheless we had a further look into the values of s for all three examples. The distributions of the local mean values s is shown in figure 35 with s normalized like $s = \langle I \rangle_{loc} / \langle s \rangle$, where two different fit possibilities are added. In blue the fit with the χ^2-distribution according to equation (8.4) is plotted and in red a normal distribution. Unfortunately it is not decidable, which of these fits describe the data better, as both have a nearly equal curve progression and deviation errors of the same order. Moreover the obtained values for the n-parameters of 10.6, 34.4, 61.3 of the χ^2-distribution do not coincide with the value of 2 in the overall intensity distribution of figure 33, resulting in a violation of consistency. Several other window lengths and other experimental data from the other fan levels and data from an experiment with a small turbine were analyzed, all resulting in similar non-consistent outcomes. Concluding we have seen a non-Gaussian distributions of intensities follow-

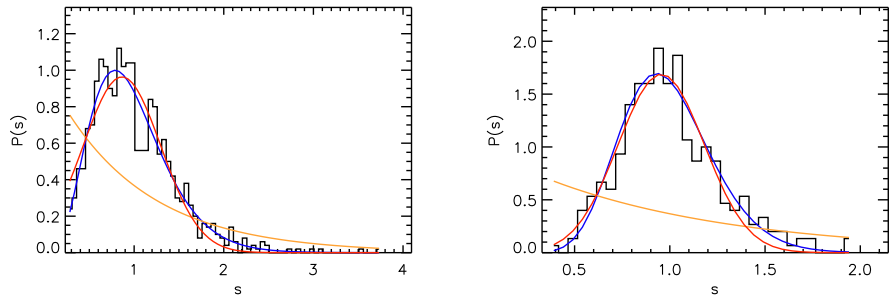

(a) 1000 windows of length = 0.0436 s, $n_{fit} = 10.6$

(b) 300 windows of length = 0.1456 s, $n_{fit} = 34.3$

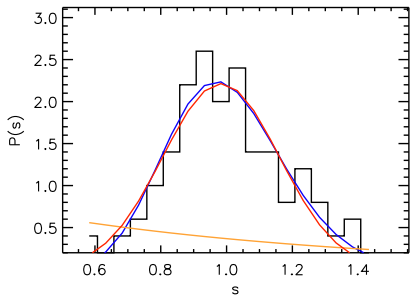

(c) 100 windows of length = 0.436 s, $n_{fit} = 61.3$

Figure 35: Distributions of local mean value with Gauss (red) and χ^2 fit (according to equation (8.4)) (blue), in orange the χ^2 distribution for the expected value of $n = 2$ is plotted

ing the expected K-distribution. However the segmentation of the signal in short time window and their analysis is still not convincing and results in the contradiction of the degrees of freedom. But the simple setup leaves room for development: As the propagating sound waves are not controlled at all, because they are caused by the rotor noise and the wind velocity, it makes it hard to test the vortex structures without knowing the exact sound input. Only if the incoming sound waves are well characterized the influence of the vortex potential on them can be identified. This leads us to the second generation of pre-experiments.

10 Measurements with external Sound Generation

To overcome the uncertainties of the sound generated by rotor noise and the air stream we added a new component to our setup: a loudspeaker to generate sound waves with a controlled, adjustable frequency. After a few attempts with borrowed equipment it became clear that we needed a high end equipment concerning a high and reliable sound frequency (to probe the turbulence) for the loudspeaker and a high sampling rate of the sound card to obtain a good resolution of the generated frequency. Our financial limits restricted us to standard audio technique offering frequencies up to 20 kHz and sampling rates of 192 kHz resulting in 9 to 10 data points per frequency period. We bought the ribbon tweeter MHT 12 of Visaton with a frequency response of 20-40 kHz, a linear amplitude frequency response and a high degree of signal fidelity. The microphone is a E 614 by Sennheiser with a frequency response of 40 Hz - 20 kHz, a good directional characteristic and a small diameter of 20 mm, as in our model the source is assumed to be even point-like (compared to the wavelenghts). A new sound card with matching connectors and a maximal sampling rate of 192 kHz was necessary to exploit the quality of microphone and loudspeaker. For controlling the experiment a Labview program was written, dealing with the synchronization of generation and recording of a provided fixed frequency. A photograph of the setup is presented in figure 36.
Now the question arose whether the loudspeaker-microphone axis should be positioned along or across the air flow. We expected the vortex patterns to change with respect to their distance to the source, the fan. Thus a positioning along the flow might lead to an averaging over many vortex patterns. Moreover the tools would be standing in the wind, influencing the turbulence. The advantage on the other hand is, that the length of wave propagation in the flow is only limited by the size of the lab. Measuring across the stream only the cross section of the air stream is available for the propagating waves, but the sort of turbulence patterns is supposed to be constant due to the fixed distance to the source. Based on these considerations the across positioning seems to be more promising. Nevertheless we always tested also the other configuration. (This case will be marked in the further analysis). A typical signal and its Fourier Transform are presented in figure 37 and 38.
The signal looks very erratic and only in the zoom 37(b) the oscillations that lie on top of the line in 37(a) are observable. But in the Fourier transform 38(a) the peak at 15 kHz, the generated frequency, is clearly visible (arrow). In the zoom of the Fourier Transform the peak occurs very sharp and clean

Figure 36: Setup with microphone (middle), loudspeaker (left), fan (right) and external sound card (middle in the front) in the "along"-configuration

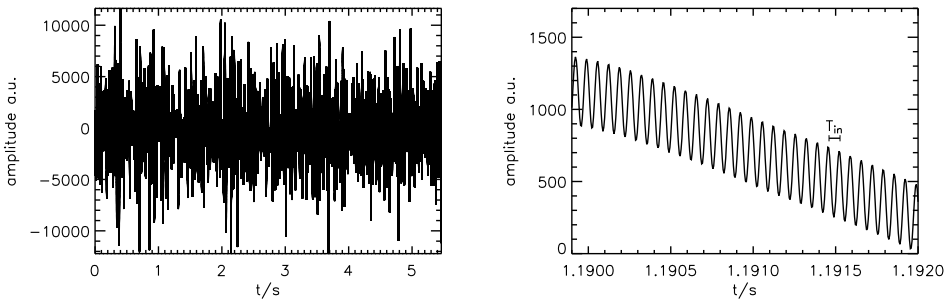

(a) Complete recorded signal

(b) Zoom

Figure 37: Amplitudes of recorded signal of fan level 1 with main frequency $\nu_{\text{in}} = 15\,\text{kHz}$ in arbitrary units and a black bar indicating the corresponding period length T_{in} in the zoom

over two orders of magnitude.
Our first attempt to cut the signal again in small time windows, Fourier transform them and to compare the height of the peak at the main frequency –an analogous procedure as in the first experiments in section 9– failed due to an insufficient resolution in the Fourier transformed signal of the short windows. The peak included only a few data points, thus an analysis of its maximum

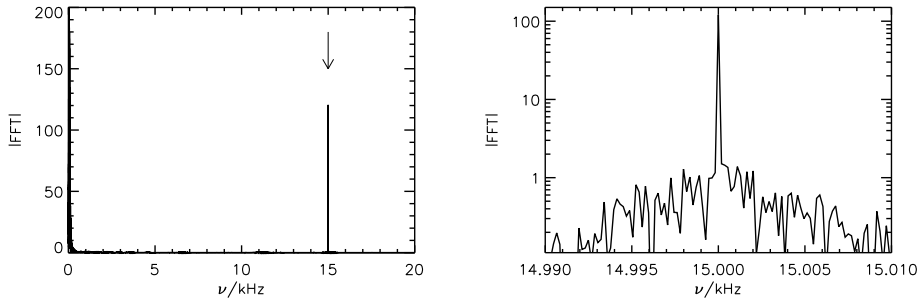

(a) FFT of the complete signal (b) Zoom around main peak as a log-plot

Figure 38: Fast Fourier transform of the same signal with dominant peak at $\nu_{\text{in}} = 15\,\text{kHz}$

was not reliable. Hence we decided to filter the signal to get rid of the frequencies caused by the air stream and the motor and use only frequencies from a window around the main peak. An example of such a filtered signal is shown in figure 39. The filtering was a standard Fourier filter: the ori-

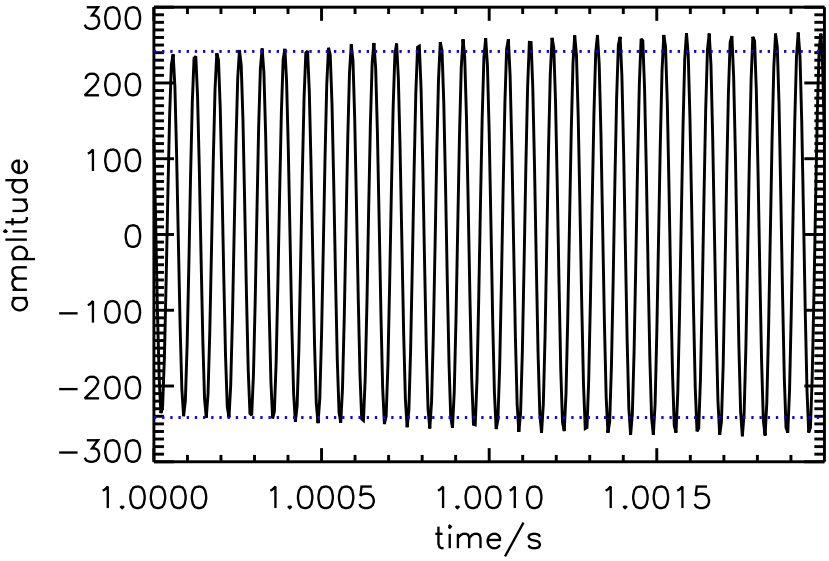

Figure 39: Amplitudes (a.u.) of filtered signal of fan level 1 with main frequency $\nu_{\text{in}} = 15\,\text{kHz}$ in arbitrary units, the vertical dotted line marks the mean amplitude

ginal signal was Fourier transformed, a window around the main peak was cut out using a rectangular window function, as other more complex window functions like Hanning or Hamming led to the same results, and finally

the remaining data was back transformed. The result was a regular cosine curve of the main frequency, but with an envelope shaping the amplitudes and small variations of the mean period length. These deviations from the mean amplitude are marked in figure 40(a) as well as the deviations from the main frequency in the period length (figure 40(b)). As the deviations of

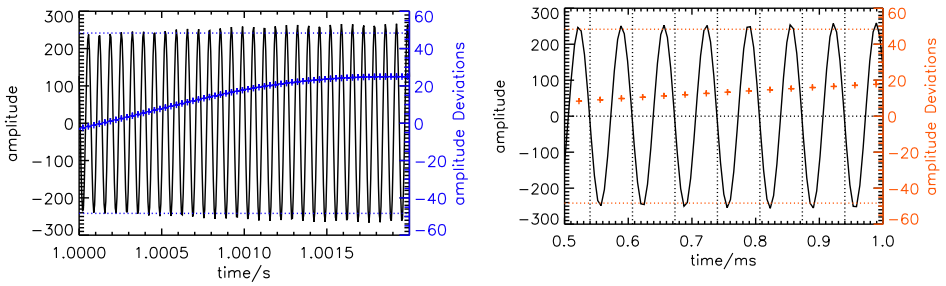

(a) Deviations from mean amplitude marked in blue (note the different scales!)

(b) Zoom: Deviations from mean amplitude marked in red and the mean periods are marked by vertical lines

Figure 40: Filtered signal with main frequency of 15 kHz (fan's level 1)

the periods can only be seen in large zoom-ins (see figure 40(b)), where of course only a few oscillations are shown, those two deviations are analyzed statistically. To avoid windowing effects of the filter procedure the first and last 1500 periods were not taken into account for further investigations. To extract these deviations reliably a fit was necessary, as due to the small sampling rate of only ≈ 10 data points per period the extremal data point did not describe the maximum correctly.
After attempts with parabolic and order 4 polynomial fits a local cosine fit of a few data points around the extremal points lead to the cleanest results. But how many points are to include into one fit? On the one hand more data points mean longer times used for one fit, which is supposed to be *local*. On the other hand minimum 3 points were needed for a cosine fit. Hence we ended up with 5 data points per fit of every half period. One example of a zoom in the filtered signal with the fit ranges indicated by the vertical lines and two half cosine fits of a minimum and maximum are presented in figure 41. Here the deviation between the extremal data points (red crosses) and the extrema of the fitted cosines (arrows) can be seen. From these fits we obtained position and amplitude of the extremal points. From the difference of the x-positions of the extrema the *local* period length P_{loc} was calculated, indicated by the horizontal arrow in the figure. These are the data points for all further investigations. Figure 42(a)/42(b) includes the distributions

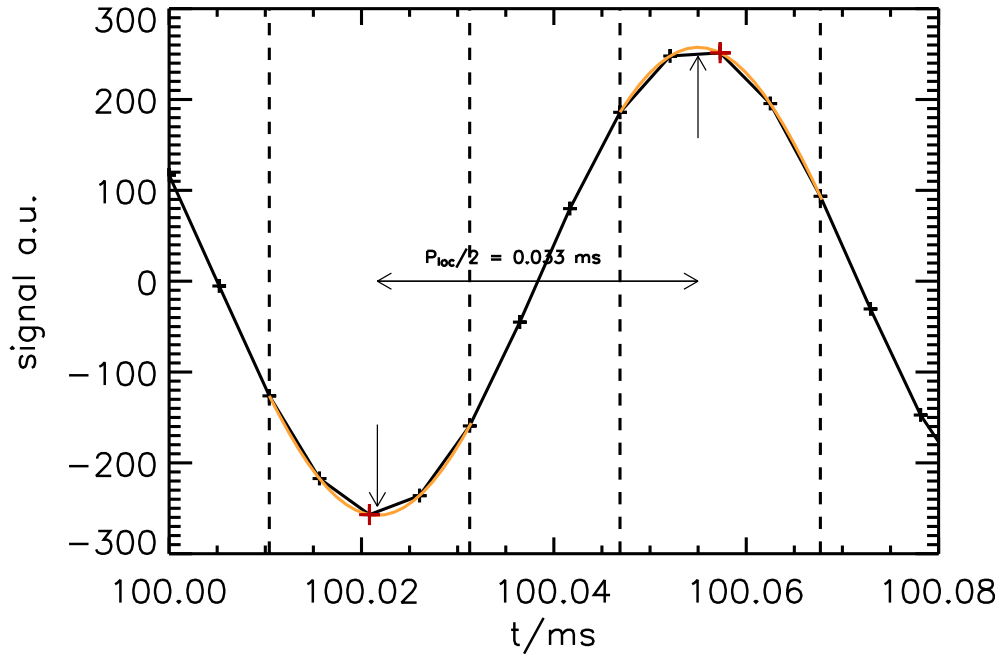

Figure 41: Amplitudes of filtered signal (same as in the figures before) with two exemplary half cosine fits (orange) in the range between the vertical lines; the minimal and maximal data points are marked by a red cross, the extrema of the fits by arrows. The horizontal arrow gives the length of half the local period length $P_{\mathrm{loc}}/2 = 0.03333\,\mathrm{ms}$ which corresponds to a local frequency of 15.0010 GHz

of deviations of the mean amplitude $A \equiv A_i - \bar{A}$ and the deviations from the mean period lengths $P \equiv P_i - \bar{P}$. Large deviations from a normal dis-

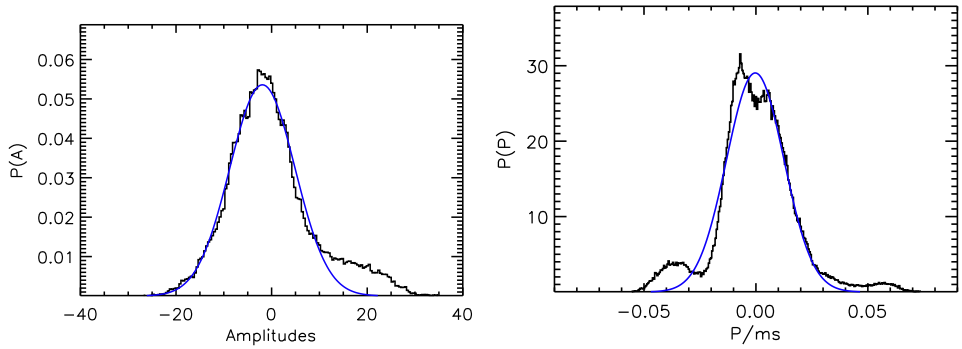

(a) Amplitudes A (b) Periods P

Figure 42: Distributions of A and P with a normal distribution (blue)

tribution (in blue as a guide to the eye) are found. Plotting A and P over the time (see figure 43) reveals that those quantities are continuous proving that frequency and sampling rate are fast enough to probe the development of the envelopes of the signal. We hope that the vortex patterns are mapped on this development. To test this assumption we changed the turbulence (by placing a obstacle between fan and setup, surely influencing the turbulence in any certain way, see figure 44) and compared the results before and after.

The distributions of A and P are changed dramatically, if one compares figure 42 and figure 45. In the latter one $P(P)$ looks very Gaussian. But $P(A)$ has large deviations from a normal distribution. Another interesting quantity to look at, especially in comparison of different underlying turbulence patterns is the (anti-)correlation between A and P, which might already be suspected by a closer look into figure 43. For a more precise analysis we created a two dimensional density plot for A and P, presented in figure 46. Additionally the correlation coefficient for two quantities defined as

$$\mathrm{Cor}(A,P) = \frac{\frac{1}{N}\sum_{i=1}^{N}(A_i - \bar{A})(P_i - \bar{P})}{\sqrt{\frac{1}{N}\sum_{i=1}^{N}(A_i - \bar{A})^2 \cdot \frac{1}{N}\sum_{i=1}^{N}(P_i - \bar{P})^2}} \tag{10.1}$$

with N the number of accessible data points is calculated. -1 means in this normalization perfect anti-, 1 perfect correlation. 0 is the value of completely uncorrelated data. Here we obtain the value $\mathrm{Cor}(A,P) = -0.029$ for the measurement with, respectively $\mathrm{Cor}(A,P) = -0.627$ without the extra obstacle. The figure 46, as well as the calculations of $\mathrm{Cor}(A,P)$, show that the anti-correlation –meaning that higher amplitudes are related to smaller

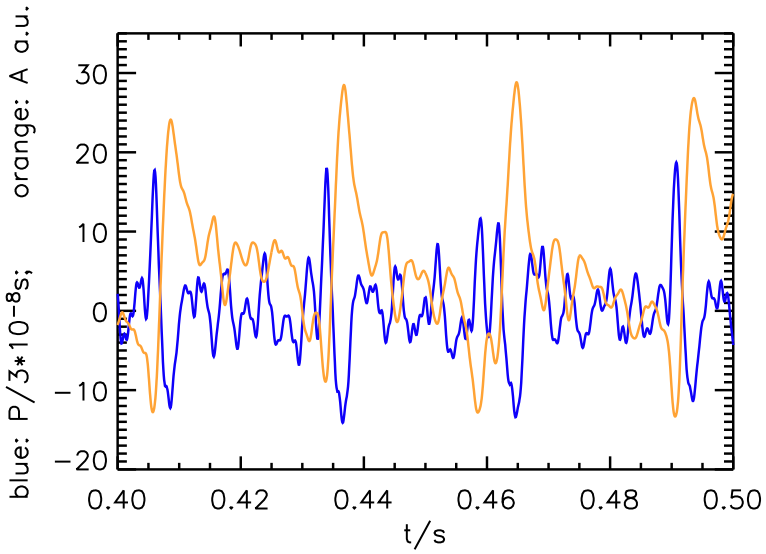

Figure 43: Time development of amplitudes (orange) and periods (blue)

Figure 44: Schematic picture of the setup with obstacle between fan and loudspeaker

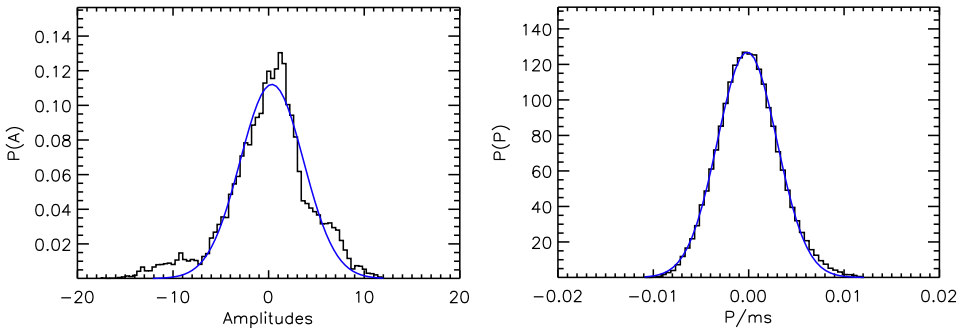

(a) Amplitudes A (b) Period lengths P

Figure 45: Distributions of A and P with a normal distribution (blue) obtained in the setup with additional obstacle in the air stream

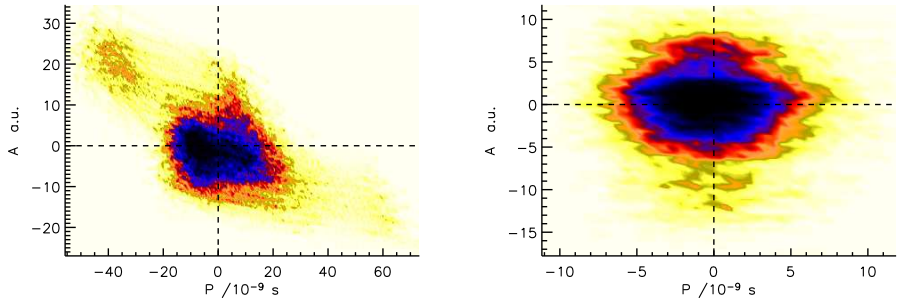

Figure 46: Shade plot of the density of correlated A and P; without obstacle $\mathrm{Cor}(A, P) = -0.627$ (left) and with obstacle $\mathrm{Cor}(A, P) = -0.029$ (right)

period lengths– is destroyed by changing the turbulence pattern. Summarizing our findings it seems that the analyzed quantities are reasonable and contain some information about the flow, information which of course has to be quantified and tested in a more precise way.
Unfortunately already figure 43 shows a clear signature of a remaining periodicity. This is checked by a Fourier Transform of A and P. Figure 47 shows the modulus of the FT of A (the results for P are not presented, but show a similar behavior) and in vertical lines a frequency of $\sigma_1 = 11.97\,\mathrm{Hz}$ (red dotted) and $\sigma_2 = 3\sigma_1 = 35.92\,\mathrm{Hz}$ (black dashed). It is obvious that the amplitude signal contains striking peaks at the two frequencies. They obviously correspond to the rotor of the fan and the frequency for the three blades, respectively, as indicated in table 2. The same oscillatory characteristics with 35.92 Hz is found looking at the autocorrelation functions, defined as the time average $\langle ... \rangle_t$ over $A(t)A(t + \Delta t)$ (see figure 48). Again we also

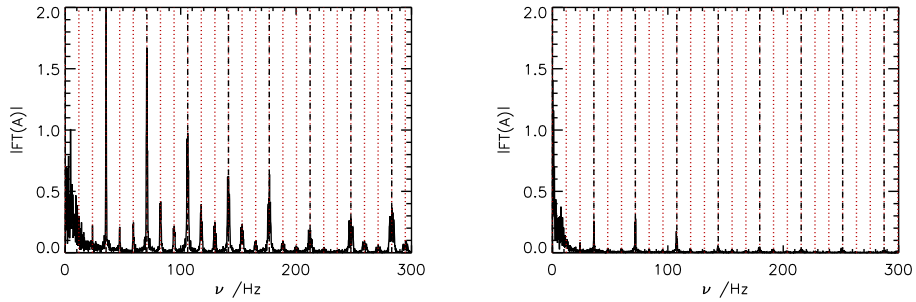

(a) without obstacle (b) with obstacle

Figure 47: Fourier transform of A for both setups (a.u.) with main frequencies indicated by vertical lines

checked the consistency with P and several other measurements with other rotor velocities, which are not shown here. It seems that the obstacle be-

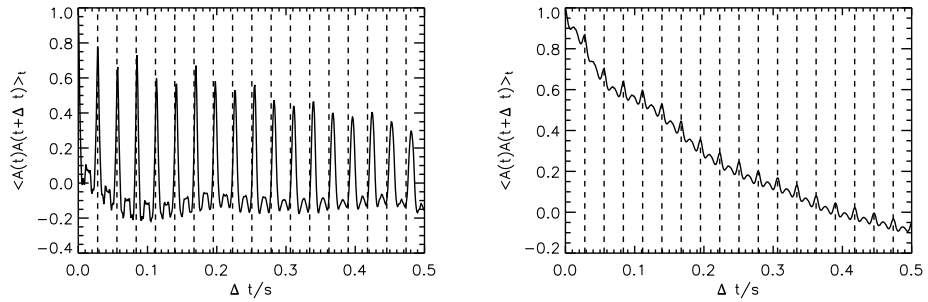

(a) without obstacle (b) with obstacle

Figure 48: Autocorrelation function of A for both setups (a.u.) with main frequencies indicated by vertical lines at $\delta t = 0.028\,\mathrm{s} \Rightarrow \nu = 35.92\,\mathrm{Hz}$

tween fan and sound setup minimizes the effect of the rotor frequency, as the occurrence of the peaks in the Fourier Transform and the autocorrelation function is less prominent, but it is still present. Now we have reached the limits of our cheap basic setup, as we must realize that the turbulence created by the fan is not "random" enough, e.g. contains to much information about its source and cannot be treated as a random potential for the propagating waves as it was proposed in our model. Here was the point to hop on a more professional level. Thus we started a cooperation with the group of professor Joachim Peinke in Oldenburg, where a large wind tunnel with very reliable conditions is installed.

11 Measurements in a large Wind Tunnel

Through this cooperation I got the possibility to perform the next measurements in the institute of physics of the Carl-von-Ossietzky University in Oldenburg in professor Peinke's group. Their wind tunnel is a recirculating acoustic tunnel schematically presented in figure 49. In the laminar regime

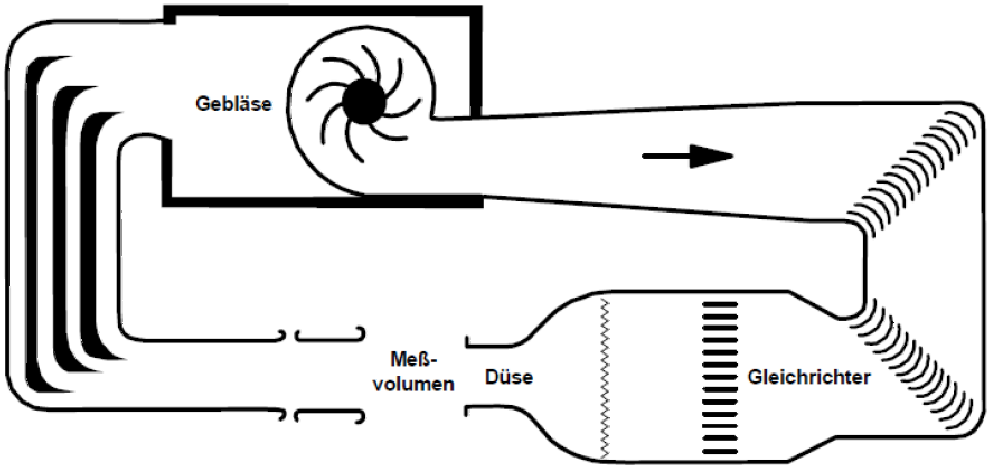

Figure 49: Scheme of wind tunnel of the Göttinger style used in Oldenburg, taken from [34]

the wind tunnel has a background turbulence intensity of less than 0.2% and a maximal wind speed of 50 m/s can be reached. The tunnel is normally open with a 1.8 m long test section (denoted by "Meßvolumen" in the picture) between the absorbing funnel and the injector ("Düse"). The streams' cross section at the injector has the size of 1.0 x 0.80 m^2. The drive mechanism of the tunnel is a direct current engine with a maximum power of 77 kW. The speed of the wind is regulated via the rotational frequency of the air blower ("Gebläse") and the direction of the stream vectors is parallelized in the flow straightener ("Gleichrichter"). The control can be carried out manually at an operator console. Additionally the tunnel has a temperature controll system, ensuring a variation of temperature of less than $\pm 1^\circ$ C. The approach velocity is defined by the controlling voltage at the wind tunnel. In this thesis instead of the voltage the corresponding speed of wind and the rotations per minute will be indicated (e.g. the speed of the free air stream without any obstacles or grids), because these are the more intuitive quantities. A controlling voltage of 1.0 V corresponds here to a reference wind speed of 5.26 m/s. All the information about the wind tunnel were communicated to me during my stay in Oldenburg or can be found in [35].

To generate a turbulent air flow obstacles in the stream are installed systematically: To obtain homogeneous and isotropic turbulence rectangular grids of a defined mesh size are used. The largest scale of the turbulence pattern is thus predetermined by the mesh size. The formation of vortices is based on the viscous shear forces at the grid elements. Eddies arise mainly in the plane perpendicular to the grid with vortex vectors oriented parallel to the bars. Hence there is a large anisotropy of turbulence directly behind the grid. Downstream the current field changes due to the interaction and the dissolution of the eddies, respectively the dissipation. Thus we can expect the turbulence only to be homogeneous and isotropic if the distance to the grid is sufficiently large (depending on mesh size, wind speed etc.).
The precise characteristics of the turbulence created with the accessible grids is unknown. Thus I exhaust the full parameter range like mesh size, bar width, wind velocity, distances to the grid and generated sound frequency to see where the findings match with our basis model.

11.1 Findings

For the experiments in the wind tunnel in Oldenburg the same sound equipment as in the previous section was used. First measurements without extra grid were performed to be the reference for the further analysis. Then 3 regular rectangular grids were installed and finally one fractal grid. The last was used only as investigation of its turbulence is of actual interest of the local group in Oldenburg and there might be some new aspects from which they could take benefit [36]. A picture of the grids and the setup is shown in figure 50. Loudspeaker and microphone are installed to the right and to the left outside of the air stream in the height of the grid center, see figure 51. Sound card and PC are positioned outside of the test section. I made sure that the temperature during my experiments was constant at $20° \pm 0.5°$ C.

The relevant settings of my LabView program are documented in table 3. The excited frequencies were for all setups (defined by wind speed, grid and

Volume	100
Amplitude	20
Sampling Rate	192 kHz
number of channels	1 (mono)
bits per sample	16
recording time	15 s
pause between recordings	2 s

Table 3: Setting of the controlling LabView program

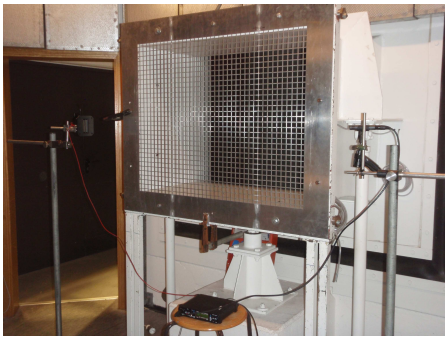

(a) grid 1

(b) grid 3

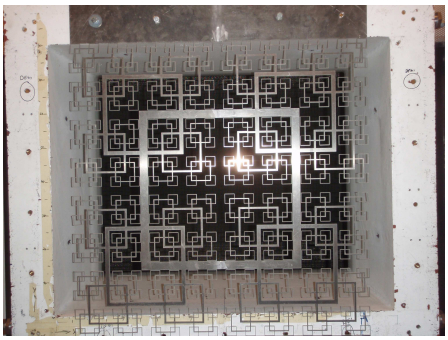

(c) fractal grid

(d) no grid

Figure 50: Photograph of the different grids respectively tunnel without grid with microphone, loudspeaker and sound card in the front

distance to the grid) $\nu = 0, 2.5, 5.0, 7.5, 10.0, 12.5, 15.0, 17.5, 20.0\,\mathrm{kHz}$. 0 Hz means in this case that no sound was generated, so that the pure noise of the wind and the environment was measured. The nine measurements were performed automatically with a short pause in between to adjust properly for the new frequency. Hence the sound was started at t_0, but the recording started 2 s later when transient oscillation of the loudspeaker was over. The recording time of 15 s was a compromise between gathering enough statistic for the analysis but performing as many measurements during my stay as possible. After the recording of the nine different frequencies the wind speed was increased from 5 to 20 m/s in 5 m/s-steps. One more measurement nearly without wind $\leq 0.23\,\mathrm{m/s}$ but with running engine was additionally performed. All these parameter combinations were measured three times for each installed grid in distance to the grid plane of 16, 88 and 150 cm. The mesh sizes of the grids are found in table 4. The fractal grid consists of 5 generations of squares, the denoted values belong to the largest cell. The ra-

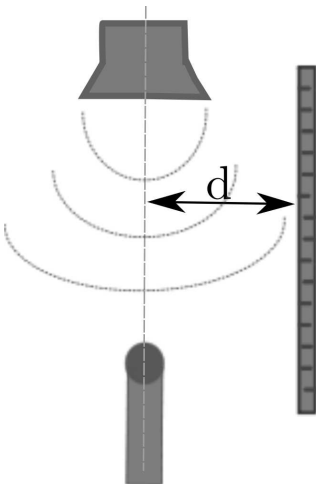

Figure 51: Sketch of experimental arrangement of microphone-loudspeaker-axis parallel to the grid in distance d

tios of the bars's length and thickness between every iteration are $R_L = 0.5$ respectively $R_t = 0.5$ [36]. The data analysis was performed in the same

Grid no.	mesh size/bar length	bar width
1	2.2 cm	0.35 cm
2	4.5 cm	0.8 cm
3	8.9 cm	1.5 cm
4 (fractal)	$L_{max} = 44.7$ cm	$t_{max} = 2.37$ cm

Table 4: Geometry of the used grids

way as in section 10. Again A and P are the quantities obtained and used for further treatment. Of course all the data was analyzed, but due to the large amount of measurements only a few exemplary measurements are presented. Learning from the experiences in the test measurements we checked the Fourier Transform for any unwanted periodicities. Only a small 50 Hz instability and a slight 9 Hz peak are found. The first one is the expected frequency of the electricity network, the second one corresponds to the time of circulation of the wind tunnel. Both effects are much smaller than the influence of the rotation frequencies of the fan, thus we hope to be close to our ideal model of a random potential.
First of all the distributions of A (not shown) and P were investigated. Figure 52 includes exemplary several different distributions of P. On that basis all the relevant properties will be discussed. In the left column of figure 52 a linear and in the right column a logarithmic plot are presented, which

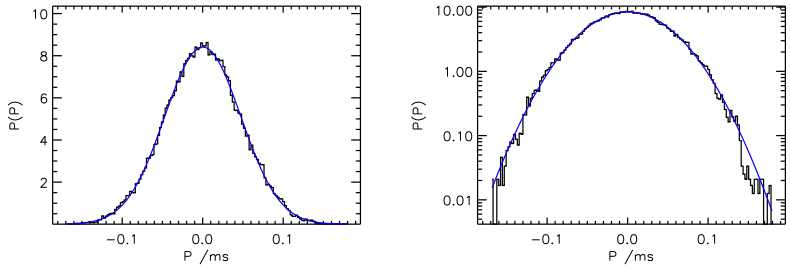

(a) without grid, distance $d = 16\,\mathrm{cm}$, wind speed $= 20\,\mathrm{m/s}$, $5\,\mathrm{kHz}$

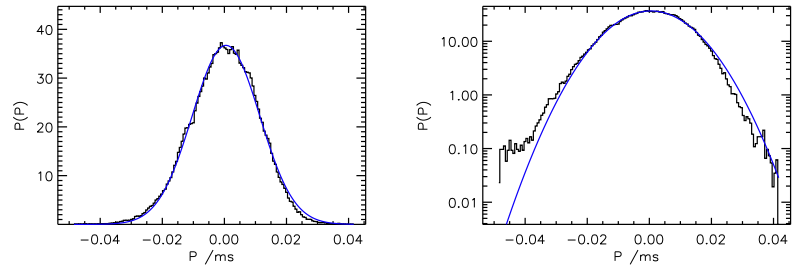

(b) without grid, $d = 16\,\mathrm{cm}$, wind speed $= 20\,\mathrm{m/s}$, $20\,\mathrm{kHz}$

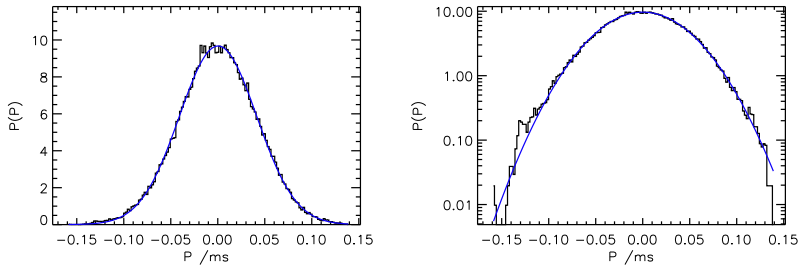

(c) grid 3, $d = 16\,\mathrm{cm}$, wind speed $= 10\,\mathrm{m/s}$, $5\,\mathrm{kHz}$

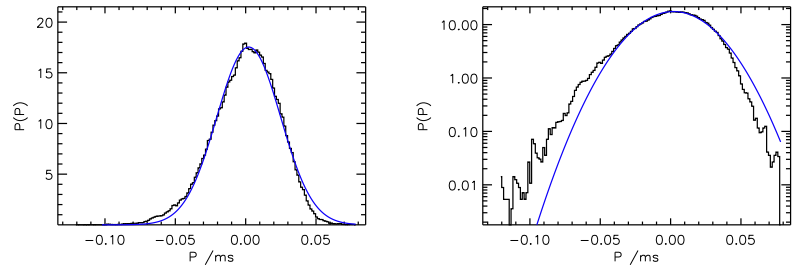

(d) grid 3, $d = 16\,\mathrm{cm}$, wind speed $= 10\,\mathrm{m/s}$, $20\,\mathrm{kHz}$

Figure 52: Distributions of P with normal distributions (blue) in a linear (left column) and a log plot (right column)

makes the deviations from the normal distribution (fit in blue) more visible. The first 4 pictures correspond to measurements without grid with a wind velocity of 20 m/s, setup positioned 16 cm away from the grid plane and with sound frequency of 5 respectively 20 kHz. The lower 4 pictures belong to grid number 3 and a wind speed of 10 m/s. In the linear plot all the distributions follow the normal distribution. But the logarithmic plots in 52 (d) and (h) reveal some deviations in the tails. Especially (h) contains significant deviations and asymmetry. Here we hope to find the reminiscences of the turbulence's nature. Hence we focus on the third and fourth momenta, skewness S and kurtosis K, of the distributions and their parametric dependency. The skewness is a measure of the lopsidedness of a distribution, vanishing for any symmetric one. The kurtosis describes the deviations from a normal distribution.

$$S(x) = \frac{1}{N}\sum_{j=0}^{N-1}\left(\frac{x_j - \bar{x}}{\sqrt{\mathrm{Var}}}\right)^3 \tag{11.1}$$

$$K(x) = \frac{1}{N}\sum_{j=0}^{N-1}\left(\frac{x_j - \bar{x}}{\sqrt{\mathrm{Var}}}\right)^4 - 3 \tag{11.2}$$

where $\bar{x}$ is the mean value, Var the variance and N the number of data points. We expect these two moments to grow continuously with increasing turbulence and –if not increasing– at least to have a monotonous behavior. Again the variety of quantities and parameter combinations makes it impossible to present all the results. But a typical selection is shown in the figures 53 and 54.

No monotonous behavior was found in any of the plots. The data points

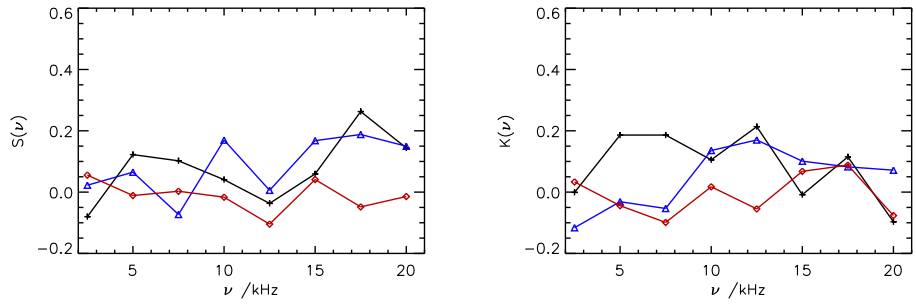

(a) Skewness of $P(A)$ (b) Kurtosis of $P(A)$

Figure 53: Grid 3, wind speed = 5 m/s, black crosses: d = 150 cm; blue triangles: d = 88 cm; red diamonds: d = 16 cm

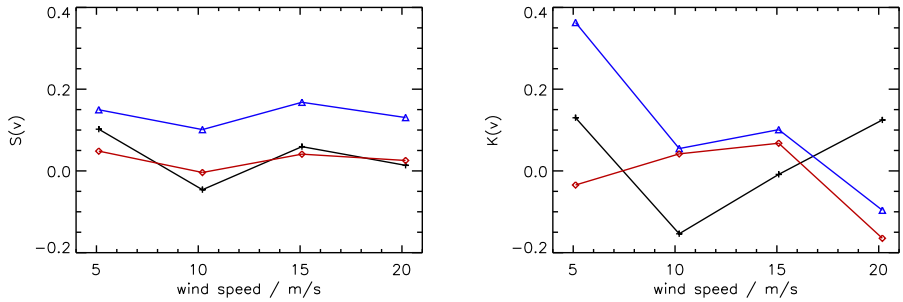

(a) Skewness of $P(A)$ (b) Kurtosis of $P(A)$

Figure 54: Grid 3, $\nu = 15\,\text{kHz}$, black crosses: d = 150 cm; blue triangles: d = 88 cm; red diamonds: d = 16 cm

of the kurtosis seem to distribute randomly around zero, changing its sign. The skewness is mostly positive, but seems not to depend significantly on the wind speed. The three curves of the different distances to the grid among themselves do not follow a certain order neither: The red curve of the minimal distance is in between the two other curves (figure 53 (b)) or nearly the lowest one (figure 54 (a)). No trend is recognizable. One problem is the low number of data points per curve (4 to 8) thus we tried to map more measurements on one new parameter, a Reynolds number defined as

$$\text{Re} = \frac{v\ L}{\nu_{\text{vis}}} \tag{11.3}$$

where v is the mean velocity of fluid (we used the wind speed), L a characteristic length dimension (we took the mesh width of the grids) and $\nu_{\text{vis}} = 1.322\ 10^{-5}\,\text{m}^2/\text{s}$ the kinematic viscosity of the air. It is clear that for a stream through a grid a Reynolds number is a microscopic quantity corresponding to local velocities on smaller scales, but we only try to map several parameter dependencies on one scale. Unfortunately also the the plots in figure 55 with several data points show no continuous behavior at all. Hence the idea of mapping length scale and wind speed on one parameter does not work. Even in the measurements with other grids, other frequencies and other distances between setup and grid no promising parameter dependence has occurred.
The last chance are the experiments without extra sound, but only the noise of the wind and the background. Here we hoped to find the characteristics of turbulence in the decline of the time correlation function of the recorded signal. Again the procedure of cutting the signal into smaller time windows failed for the same reasons as in the test measurements. Thus we had a look at the autocorrelation function of the time signal, in particular its decay. For

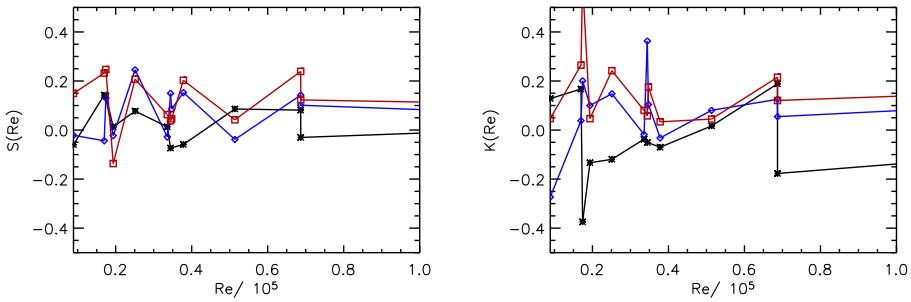

(a) Skewness of $P(A)$ (b) Kurtosis of $P(A)$

Figure 55: fixed distance d = 88 cm to the grid, mesh width and wind speed mapped onto Re; black crosses: $\nu = 5$ kHz; blue diamonds: $\nu = 10$ kHz; red squares: $\nu = 15$ kHz

this purpose we investigate its first zero crossing t_0, presented in figure 56. As we have $\Delta t = 0.001$ s in the autocorrelation function, this is the resolution of the zero crossing. Initially we expected that a more turbulent air flow

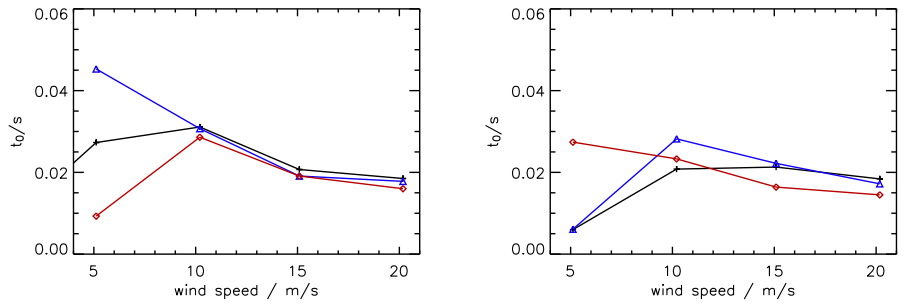

(a) no grid (b) grid 3

Figure 56: Zero crossing t_0 of the autocorrelation function; black crosses: d = 150 cm; blue triangles: d = 88 cm; red diamonds: d = 16 cm

leads to a faster decay of the sound signal's autocorrelation, thus to smaller values of t_0. For one grid t_0 should thus decay for higher wind speeds and there should be an observable difference between the different grids and for different distances to the grid. This behavior was observed in figure 56(a) for the laminar flow without grid. Here the autocorrelation decays for higher wind speeds from 10 m/s. However here the data for the measurements with grid look very similar to the measurements with the laminar flow. Moreover there is nearly no difference between the different distances between setup

and grid. Thus it is impossible to gather information about the turbulence, a typical correlation length or its intensity from these measurements.

12 Discussion

Finally after evaluating all these measurements carefully the experiments have shown that the suggested picture of vortex fields changing smoothly with time and providing a random potential for the propagating sound waves could not be observed. Possible causes for the discrepancy of experimental findings and the model are the following: It is not clear if the transfer of our basic model to the physical system of sound waves traveling through a turbulent air stream is correct and where its limits are. Though the exact characteristics of the flow behind the grids are not known it is clear that the turbulence is created on one scale and breaks down through the cascade until the dissipation regime is reached. Kolmogorow found in his works in 1962 the 5/3-law for the spectral density $P(k) \propto k^{-5/3}$ depending on the wave number k [37]. Thus it is impossible to define a proper correlation length in a turbulent flow, as all vortex sizes between the largest initial size and the dissipation length appear with a certain probability. If and how many of them can be resolved with our sound waves is unclear. Maybe ultra-sound frequencies and higher sampling rates would be more suitable to resolve the structures. In addition the turbulence intensities in the wind tunnel may be too small to imitate a random potential. Pascal Knebel wrote in his thesis [35] about his development of active grids to increase the turbulence intensity as it is hard to reach it with standard grids. He writes that one needs on the one hand a large distance to the grid to obtain a homogeneous and isotropic turbulence independent from direction and geometry of the grid, but that on the other hand then the dissipation becomes more prominent and shrinks the turbulence intensity. The reason for this problem is that the redistribution of the vorticity runs slower than the dissipation. Consequently, the turbulence was neither homogeneous nor isotropic in the close distances to the grid. But this was a strong assumption in our model. For the largest distances isotropy and homogeneity are improved, but here the turbulence becomes too weak. This might be the reason for the similar findings for the laminar flow without and the turbulent flow with grids (see e.g. figure 56).
The second type of experiments without external sound, where the recorded signal was caused by the turbulence, was much too complicated to match with our simple model. The process of sound radiated from a fluid flow is a very complex problem and is investigated for decades [38, 39].

Approaching a new experimental field within a limited time and with a limited budget is always risky, but holds a large potential in case of success. In summary our setup with the accessible equipment was not appropriate to adapt to the simple model, which was developed in microwave measurements.

Part III
Study of n-Disk Systems

13 Motivation

The study of n-disk systems, its classical and quantum mechanical dynamics, offers many relations to the fundamental fields and topics of quantum chaos: We will investigate periodic orbits and the system's repeller, which turns out to be fractal. For the categorization and bookkeeping of the infinitely many periodic orbits we need to exploit symmetries by applying group theory, need to find symbolic dynamics and take care of the pruning. These periodic classical trajectories will leave its fingerprints also in quantum properties and we will find a spectral gap of the complex quantum mechanical resonances, which can be calculated from classical geometrical properties of the system using transfer operators and the thermodynamic formalism resulting in classical zeta functions.
The relation between classical and quantum mechanical quantities manifests itself in many famous equations like the Gutzwiller trace formula, relating the eigenvalue spectrum of the Schrödinger operator to the periodic orbits of the underlying classical system [6], the (fractal) Weyl law concerning the asymptotic eigenlevel number [7] and its relation to the system's dimension or the Hausdorff dimension of the fractal repeller, respectively. Not only the spectrum but also chaotic wave functions include the memory of the classical dynamic as was already observed experimentally in our group for two- [40] and three-dimensional [41] billiards and named *scarring* [8, 42].
The n-disk system is a system, which is very instructive due to its simple geometry, defined only by the ratio of disk radius to disk distance. This unique geometric parameter defines at the same time the opening of the system. Thus it offers the possibility to control the opening very accurately and allows for a continuous transition from a closed over a weakly to a wide open configuration. This transition is studied in the numerical calculations (see section 15) and in the experimental realization as well (section 16.1). Open systems are experimentally difficult to handle, as the resonances in the spectrum become broad and overlap strongly. Here we face the data extraction of the resonances as the big challenge. The harmonic inversion, our solution to this problem, is presented in section 16.2. With the successfully extracted resonances the distribution of their imaginary parts is studied, especially their distance to the real axis, the spectral gap. The results are shown in section 17.2 and we published them in [43]. Beside the imaginary parts of the

complex resonances we can investigate the counting function of the real parts and its asymptotic exponent and compare it with the calculated Hausdorff dimension (section 17.3). The results on this have already been published in [44].

14 Definition of n-Disk Systems

A paradigmatic hyperbolic open system with a classical fractal repeller is the n-disk system (see figure 65 and 66). The repeller are those points in phase space that do not escape to infinity neither for positive nor for negative times. It has been introduced in the late 80s by Ikawa in mathematics [45] and by Gaspard and Rice [13, 46] and Cvitanović and Eckhardt [14] in physics. Theoretically it has been studied in the classical, semiclassical and quantum mechanical regime and there has also been an experimental study on the spectral autocorrelation [47, 48]. A n-disk system describes the scattering of a classical or quantum mechanical particle in a 2 dimensional plane on n hard disks (i.e. infinite circular potentials) whose centers form a regular polygon. While the distance between the centers historically is denoted by R the radius of the disks is called a and up to scaling the geometry is completely described by the ratio R/a (for an illustration see figures 65 and 66). This ratio also defines the "openness" of the system: For $R/a = 2$ the disks are touching each other and we have a closed area in the interior between the disks. By increasing this ratio parameter the distances between the disks become larger and the interior couples to the outside. The system's simplicity allows for a detailed study of quantum mechanical, semiclassical and classical scattering. For the classical study of the n-disk system one is interested in the trajectories of particles which perform hard wall reflections on the disks or escape to infinity. From periodic trajectories a wide range of classical quantities like the classical escape rate, the fractal dimension of the repeller and the topological pressure can be calculated. Though they are purely classical they will play a role in the analysis of the quantum resonances. This will be described in section 15. From here on we restrict $n > 2$ as there is just one periodic orbit in the 2-disk system (the bouncing ball between the disks) and only from $n = 3$ there exist infinitely many periodic orbits providing the needed complexity.
The big advantage of the n-disk systems is that the orbits can be categorized and provide a constructive topological description of the system dynamics: With the so called symbolic coding every orbit can be translated into a word including the labels $1, 2, \ldots, n$ (the alphabet) for every disk, with that the particle collides. Orbits belonging to the repeller are described by an infinite

series of labels, where especially the periodic orbits consist of a bi-finite but periodically repeated sequence, e.g. a bouncing ball orbit between disks 1 and 2 will be denoted by $\overline{12}$ or simply by 12 if it is clear from the context that a periodic orbit is meant. It is shown (e.g. in [49]) that there exists a one to one correspondence between every possible label sequence and the periodic orbits with the only restriction that two consecutive labels must not be the same. This one to one correspondence is only valid for disks sufficiently far apart, because for very narrow configurations some orbits do intersect with another disk's boundary which will prohibit these orbits. In this case the symbolic dynamics is not complete anymore and an additional grammar, i.e. pruning rules, must be introduced, see figure 57. For all calculations based on the symbolic dynamics it thus must be ensured that the appearing orbits are not pruned. Considering the restriction of the symbol repetition and respecting

Figure 57: Periodic Orbit 0213243041 (= $\underline{21}$ in reduced coding) in the 5-disk system pruned ($R/a = 2.1$) (left) and valid ($R/a = 2.5$) (right)

the symmetry degeneration of orbits (e.g. the bouncing balls 12 and 23 can be transfered into each other by a rotation operation and thus look the same in the projection onto the fundamental domain) we took advantage of the symbolic dynamics for the symmetry reduced system, invented by Eckhardt and Cvitanović in 1989 [14]. For the 3-disk system they have shown that the symbolic dynamics associated with the numbering of the disks of the collision (with the restriction that the same disk cannot be hit twice in serial) can be reduced to the binary code 0 for reflecting backwards to the previous disk and 1 for reflecting forwards to the next disk. Hence the global symbolic orbit $\overline{12}$ becomes 0 and the orbit $\overline{123}$ becomes 1 in reduced code. Further details can be found in the original publications [49, 50]. Generally speaking a coding of a n-disk system of n labels with the only rule regarding symbol repetition will lead to $(n-1)$ reduced labels without extra restrictions. For the 5-disk system we had to generalize this reduced alphabet: We chose the

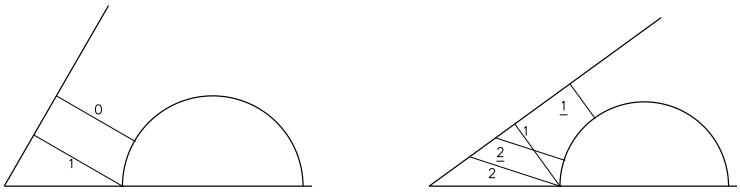

Figure 58: 3-disk (left) and 5-disk (right) fundamental domain with the fundamental (= order 1) orbits 0, 1 respectively 1, $\underline{1}$, 2, $\underline{2}$

four symbols $1, 2, \underline{1}, \underline{2}$, where the number plays the role of the distance to the next disk of collision. The underlining indicates a reverse of orientation of the following dynamic after the collision with the disk. Consequently the direction changes from clockwise to anticlockwise or the other way round. A non-underlined number keeps the orientation and indicates a flight to a disk in distance 1 or 2 in the current direction. For example the global orbit $\overline{12}$ becomes $\underline{1}$ and the orbit $\overline{12345}$ becomes 1. The fundamental orbits of the 3-disk and 5-disk systems are illustrated in figure 58. It is obvious that all periodic orbits of an order n in the symmetry reduced case include orbits up to much higher orders in the global code. E.g. the global orbit $\overline{0213243041}$ (see figure 57) of order 10 reduces to $\underline{12}$ (order 2) and is consequently already included in a second order symmetry reduced calculation. Why this reduction leads to a better convergence of the computations of the classical quantities and how it is implemented will be explained in section 15.6 and appendix H. The quantum n-disk system is described by the Helmholtz equation

$$-\nabla^2 \psi_n = k_n^2 \psi_n \tag{14.1}$$

with Dirichlet boundary conditions on the disks boundaries. As the system is open the quantum resonances $k_n = \mathrm{Re}(k_n) + i\mathrm{Im}(k_n)$ are complex valued. For the 3-disk system Gaspard and Rice [51] gave an explicit expression for the scattering matrix in terms of Bessel and Hankel functions which allows for the calculation of the quantum resonances numerically, which is presented in the appendix I and whose findings are compared with the experiments in section 17.1.
We realize such a "quantum" n-disk system in a microwave analog system based on the ideas presented already in section 2 and described in detail in 16.1.

15 Theoretical Background

15.1 Classical Escape Rate

The escape rate is a classical quantity which turned out to be also interesting in a quantum system in the description of the distributions of the imaginary parts of resonances [52]. This connection will be exploited in the section of the experimental results 17.2. But first a definition of this quantity is given and based on that in the next passages its relation to a ζ-function and topological pressure is presented.
Imagine a classical open scattering system with a scattering center (e.g. several hard disks of our n-disk system) and N_0 point-like particles with a fixed energy. They will be launched towards the scattering center in all angles. For the limit of large N_0 and large times the number of particles in the scattering region (e.g. inside a virtual box around the disks) goes like $N(t)/N_0 \propto \exp(-\gamma t)$, where γ is referred to as the "classical escape rate". γ is related to the largest eigenvalue of a transfer operator $\hat{F}_t$ which is introduced now. This section does not intend to give a detailed mathematical derivation of all the classical and semiclassical calculations, but I would like to give an overview of the ideas of the abstract mathematical way and try to give some intuitive arguments where the strict derivations are too bulky and not helpful for a further understanding.
The transfer operator describes the time development of a function $\varphi \in \mathcal{C}^\infty(\Sigma_E)$, where Σ_E is an energy shell in phase space. Such a function may be the probability density, which modulus square denotes the probability of finding particles in a certain phase space volume. For the time development a Hamiltonian flow acting on the phase space variables p and q like

$$\begin{aligned} \Phi_t : \Sigma_E &\to \Sigma_E \\ p, q &\mapsto p(t), q(t) \end{aligned} \tag{15.1}$$

is responsible. Now the time development of φ, i.e. the transfer operator, can be defined as

$$\hat{F}_t \ \varphi(p,q) \equiv \varphi_t(p,q) := \varphi(\Phi_{-t}(p,q)) \tag{15.2}$$

Figure 60 (b) is a good illustration for the appearance of $\Phi_{-t}(p,q)$. The important property of the transfer operator $\hat{F}_{n\cdot t}\varphi = \hat{F}_t^n\varphi$ can easily be seen as for the flow it is $\Phi_{t_1+t_2}(p,q) = \Phi_{t_2}(\Phi_{t_1}(p,q))$. Now let us suppose that $\hat{F}_{t_0}$ acting on a Hilbert space $\mathcal{H}$ is diagonalizable, then there is a complete set of complex eigenfunctions φ_i and eigenvalues λ_i with $1 \geq |\lambda_0| \geq |\lambda_1| \geq \ldots$. This inequality is true for open systems without gain where the particle probability

always decays with time. For later application it is suitable to write the eigenvalues as $\lambda_i = \exp(-t_0\gamma_i)$ with $\gamma_i \in \mathbb{C}$ and $0 \leq \mathrm{Re}(\gamma_0) \leq \mathrm{Re}(\gamma_1) \leq \ldots$. Now any probability distribution φ_0 on Σ_E at time $t = 0$ can be written as a superposition of the eigenfunctions φ_i

$$\varphi_0 = \Sigma_i c_i \varphi_i$$

At time $t = nt_0$ we find

$$\begin{aligned}
\varphi_t &= \hat{F}_t\ \varphi_0 \\
&= \hat{F}_{t_0}^n\ \varphi_0 = \hat{F}_{t_0}^n\ \Sigma_i c_i \varphi_i \\
&= \Sigma_i c_i \lambda_i^n \varphi_i \\
&= \Sigma_i c_i \exp(-nt_0\gamma_i)\varphi_i \\
&= \Sigma_i c_i \exp(-t\gamma_i)\varphi_i \\
&\xrightarrow{t\to\infty} c_0 \exp(-t\gamma_0)\varphi_0
\end{aligned}$$

This means that for large times only the decay with the smallest $\mathrm{Re}(\gamma_0)$ survives and we obtain for the probability an exponential behavior $\propto \exp(-t\gamma_0)$, the requested condition on the idea of an escape rate. Now the problem is of course how to obtain the eigenfunctions and eigenvalues (especially the largest one) of $\hat{F}_t$. The problem can also be restated as

$$\begin{aligned}
\hat{F}_{t_0}\ \varphi_0 = \lambda_0\varphi_0 \quad &\Leftrightarrow \quad \lambda_0^{-1}\hat{F}_{t_0}\ \varphi_0 = \varphi_0 \\
&\Leftrightarrow \quad \det\left(\lambda_0^{-1}\hat{F}_{t_0} - \mathbb{1}\right) = 0 \\
&\Leftrightarrow \quad \det\left(e^{t_0\gamma_0}\hat{F}_{t_0} - \mathbb{1}\right) = 0 \qquad (15.3)
\end{aligned}$$

Thus the finding of the escape rate is equivalent of finding the root with the largest real part of $\tilde{\zeta}^{-1}(s) \equiv \det\left(e^{t_0 s}\hat{F}_{t_0} - \mathbb{1}\right)$.
Up to now we considered only global dynamic on the energy shell, but our aim is to connect the periodic orbits in symbolic coding with this problem. The symbolic coding is a discrete dynamic as it only considers the collisions with the disks and its order, but not the free flight in between. Thus it makes sense to come to a reduced and discrete dynamic on a Poincare section. In the n-disk case this is typically the collision point on the disks' wall and the angle of reflection. But the explicit form is not important here: Let $\mathcal{S}$ be a submanifold of the energy shell Σ_E and P acting on it like

$$\begin{aligned}
P : \mathcal{S} &\to \mathcal{S} \\
z &\mapsto \Phi_{t_z}(z) \qquad (15.4)
\end{aligned}$$

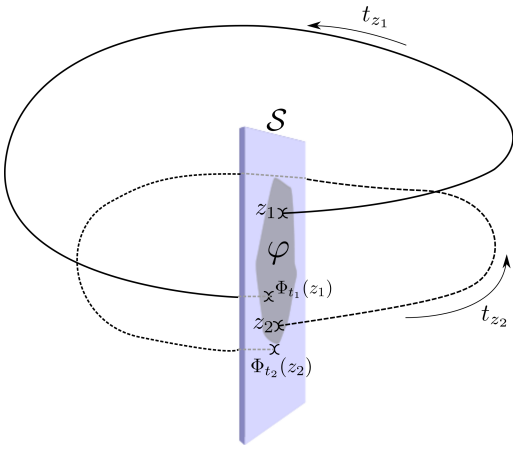

Figure 59: Poincare section $\mathcal{S}$ with a function φ and the two points z_1 and z_2 with their evolution with Φ and $t_{z_1} > t_{z_2}$

with $t_z > 0$ is the shortest time with $\Phi_{t_z}(z) \in \mathcal{S}$. A schematic picture of this procedure is given in figure 59. The naive definition of a transfer operator

$$\begin{aligned} \hat{P} : \mathcal{C}^\infty(\mathcal{S}) &\to \mathcal{C}^\infty(\mathcal{S}) \\ \varphi(z) &\mapsto \varphi\left(P^{-1}(z)\right) \end{aligned} \tag{15.5}$$

is not convenient as its eigenfunction can not be continued on the full Σ_E as the time t_z depends on the starting point z, see figure 59. Thus a family of operators is defined like

$$\begin{aligned} \hat{P}_s : \mathcal{C}^\infty(\mathcal{S}) &\to \mathcal{C}^\infty(\mathcal{S}) \\ \varphi(z) &\mapsto e^{-t_z s}\, \varphi\left(P^{-1}(z)\right) \end{aligned} \tag{15.6}$$

because if there exists an s with $\det(1 - \hat{P}_s) = 0$, i.e. there is a φ_0, which is eigenfunction of $\hat{P}_s$ with eigenvalue 1, then $\varphi_0(z)$ can be continued for every $(p, q) \in \Sigma_E$:

$$\tilde{\varphi_0}(p, q) := \varphi_0(z_{p,q}) e^{-s t_{p,q}}$$

where $z_{p,q} \in \mathcal{S}$ with $\exists t$ s.t. $\Phi_t(z_{p,q}) = (p, q)$ and this $t \equiv t_{p,q}$ the time between $z_{p,q}$ and (p, q) (figure 60(a)). This continuation of φ is in agreement with the dynamics on the Poincare section, because it is

$$\begin{aligned} \varphi_0 &= \hat{P}_s \varphi_0 \quad \text{(postulated for } s\text{)} \\ \Leftrightarrow \varphi_0(z) &= e^{-t_z s}\, \varphi_0\left(P^{-1}(z)\right) \quad \text{(definition of } \hat{P}_s\text{)} \\ \Leftrightarrow \varphi_0(P(\tilde{z})) &= e^{-t_z s}\, \varphi_0(\tilde{z}) \quad \text{(with } z = P(\tilde{z})\text{)} \end{aligned}$$

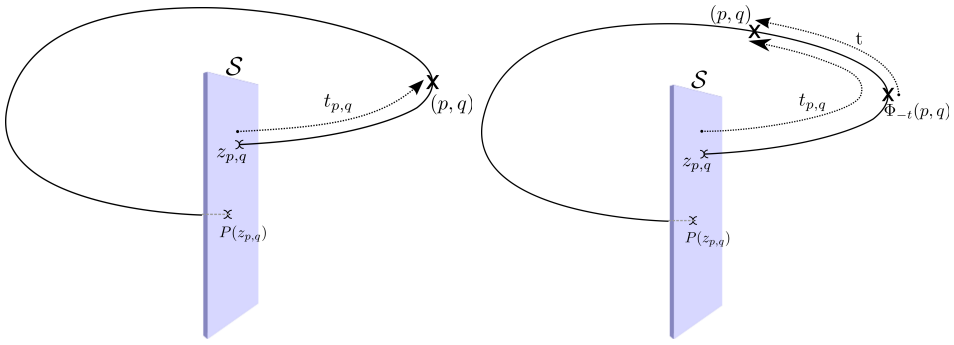

(a) continuation for every $(p,q) \in \Sigma_E$ (b) notations of times t and $t_{p,q}$

Figure 60: Poincare section $\mathcal{S}$

where the last equation gives the evolution of φ_0 on $\mathcal{S}$.
$\tilde{\varphi}$ is an eigenfunction of $\hat{F}_t$ as

$$\hat{F}_t \ \tilde{\varphi_0}(p,q) \equiv \tilde{\varphi_0}\left(\Phi_{-t}(p,q)\right) = \varphi_0(z_{p,q}) \ e^{-s(t_{p,q}-t)} = \tilde{\varphi_0}(p,q) \ e^{st}$$

The illustrations of the different times are plotted in figure 60(b). To summarize the findings up to here: Finding the classical escape rate is equivalent of finding the correct s in the operator family $\hat{P}_s$, such that there is an eigenfunction φ_0 with eigenvalue 1. So we are led to the problem of finding the poles of the dynamical ζ-function

$$\zeta^{-1}(s) := \det(1 - \hat{P}_s) \tag{15.7}$$

The determinant of an operator can be evaluated by the identity $\ln \ \det = \mathrm{Tr} \ \ln$ [50] or $\det \ \exp = \exp \ \mathrm{Tr}$, for which a heuristic explanation is given in appendix C. Thus we have

$$\det(1 - \hat{P}_s) = \det \exp\left(\ln(1 - \hat{P}_s)\right) = \exp \mathrm{Tr}\left(\ln(1 - \hat{P}_s)\right)$$

Via the antiderivative of the geometric series we obtain

$$\det(1 - \hat{P}_s) = \exp\left(-\sum_{n=1}^{\infty} \frac{\mathrm{Tr}(\hat{P}_s{}^n)}{n}\right) \tag{15.8}$$

Here one needs to admit that the trace is only defined for trace class operators. We do not want to enter the mathematical discussion of the existence of the trace, but simply assume that it exists in a suitable Hilbert space. The next step is to evaluate the trace. Let us first rewrite:

$$\begin{aligned} \hat{P}_s\varphi(z) &:= e^{-t_z s} \ \varphi\left(P^{-1}(z)\right) \\ &= \int e^{-t_z s} \ \delta(x - P^{-1}(z)) \ \varphi(x) \, \mathrm{d}x \end{aligned}$$

where $e^{-t_z s}\ \delta(x - P^{-1}(z))$ can be understood as the kernel of an integral operator, from which the trace can then be calculated (appendix D).

$$\begin{aligned} \mathrm{Tr}\hat{P}_s &= \int e^{-t_z s}\ \delta(z - P^{-1}(z))\,\mathrm{d}z \\ &= \sum_{z:P(z)=z} e^{-t_z s}/|\det(1 - J_P(z))| \end{aligned}$$

where $|\det(1 - J_P(z))|$ is the determinant of the Jakobi matrix, the stability matrix evaluated on the trajectory starting and ending in z. Analogously

$$\mathrm{Tr}\hat{P}_s^{\,n} = \sum_{z:P^n(z)=z} e^{-t_{z,n} s}/|\det(1 - J_P^n(z))| \tag{15.9}$$

with $t_{z,n} := \sum_{l=0}^{n-1} t_{P^l(z)}$ is a Birkhoff sum over n evolutions of P. We now can write equation (15.7) with equations (15.8) and (15.9)

$$\zeta^{-1}(s) := \det(1 - \hat{P}_s) = \exp\left(-\sum_{n=1}^{\infty} \frac{\sum_{z:P^n(z)=z} e^{-t_{z,n} s}\ |\det(1 - J_P^n(z))|^{-1}}{n}\right) \tag{15.10}$$

This double sum could now be calculated, if all the fixed points $P^n(z) = z$ in the Poincare section are known, but it can be simplified even more. The sum over all orbit lengths (i.e. applications of Poincare operator) combined with the sum over all orbits of length n can also be translated into a sum over all prime periodic orbits, meaning orbits that are only passed through once, times the sum over the number of cyclings through the orbit. Expressed in a mathematical language: For a z with $P^n(z) = z$ and cycling time t_z there will be a smallest number $k \geq 1$ with $P^k(z) = z$. This k is called primitive period and n/k the multiplicity of the orbit, i.e. the number how often this orbit is run through. Further its true that for $1 \leq m \leq n$ the cycle time and the stability do not depend on the starting point on the orbit, i.e. $t_{z,n} = t_{P^k(z),n} \equiv T_p$ and $|\det(1 - J_P(z))| = |\det(1 - J_p)|$. As for a periodic orbit p the number of fixed points $P^n(z) = z$ coincides with its primitive period k_p we obtain for ζ

$$\zeta^{-1}(s) = \exp\left(-\sum_{n=1}^{\infty} \sum_{p \in PO(n)} \frac{k_p}{n_p} \frac{e^{-T_p s}}{|\det(1 - J_p)|}\right) \tag{15.11}$$

where the second sum now runs over all periodic orbits of length n. For every periodic orbit it is either $k_p = n_p$ –a primitive orbit– or $n_p = j\ k_p$, a repeated cycling of a primitive orbit. Moreover we have for period time and

stability matrix $T_p = j\ T_{p'}$ and $J_p = J_{p'}^j$ connecting an orbit $p \in PO(n)$ and its corresponding primitive orbit $p' \in PPO$.

$$\zeta^{-1}(s) = \exp\left(-\sum_{p' \in PPO}\sum_{j=1}^{\infty}\frac{1}{j}\ \frac{\left(e^{-T_{p'}s}\right)^j}{|\det(1-J_{p'}^j)|}\right) \tag{15.12}$$

Now we factorize the determinant into products of expanding and contracting eigenvalues as presented in [53]: For the 2 dimensional Hamiltonian system we have the two eigenvalues Λ_p and $\lambda_p = 1/\Lambda_p$ and can thereby write (using the geometric series)

$$\begin{aligned}
|\det(1-J_p^j)|^{-1} &= |(1-\Lambda_p^j)\ (1-\lambda_p^j)|^{-1} = |\Lambda_p|^{-j}\sum_{h=0}^{\infty}\sum_{k=0}^{\infty}\Lambda_p^{-hj}\lambda_p^{kj} \\
&= |\Lambda_p|^{-j}\sum_{h=0}^{\infty}\sum_{k=0}^{\infty}\Lambda_p^{-(h+k)j} = |\Lambda_p|^{-j}\sum_{k=0}^{\infty}(k+1)\Lambda_p^{-kj}
\end{aligned}$$

Inserting it into equation (15.12):

$$\begin{aligned}
\zeta^{-1}(s) &= \exp\left(-\sum_{p\in PPO}\sum_{j=1}^{\infty}\sum_{k=0}^{\infty}(k+1)\frac{1}{j}\ \left(e^{-T_p s}\right)^j\left(|\Lambda_p|^{-j}\Lambda_p^{-kj}\right)\right) \\
&= \exp\left(\sum_{p\in PPO}\sum_{k=0}^{\infty}(k+1)\ln\left(1-\frac{e^{-T_p s}}{|\Lambda_p|\Lambda_p^k}\right)\right) \\
&= \prod_{p\in PPO}\prod_{k=0}^{\infty}\left(1-\frac{e^{-T_p s}}{|\Lambda_p|\Lambda_p^k}\right)^{k+1}
\end{aligned}$$

a Selberg product of zeta functions. Interchanging the two products [49] (only allowed where it converges absolutely) one obtains a product of ζ_k functions.

$$\begin{aligned}
\zeta^{-1}(s) &= \prod_{k=0}^{\infty}\prod_{p\in PPO}\left(1-\frac{e^{-T_p s}}{|\Lambda_p|\Lambda_p^k}\right)^{k+1} \\
&\equiv \prod_{k=0}^{\infty}1/\zeta_k^{k+1}
\end{aligned} \tag{15.13}$$

From these definitions, the zeroth factor will be the one whose zeros have the largest real part. As we are only interested in these zeros we will only study this ζ-function as it is commonly done in literature, for example in [54, 49, 50]. Wirzba in [55] investigates numerically the resonances of the dynamical and a slightly different Selberg product zeta function (i. e. without the exponent

$k+1$), the *Gutzwiller-Voros function*, and finds for both a good agreement with the exact quantum mechanical ones for regions not too deep in the complex plane. This justifies the ansatz of considering only the zeroth term and by defining the *weight* τ_p of a prime periodic orbit as

$$\tau_p := \frac{e^{-T_p s}}{\Lambda_p} \tag{15.14}$$

we can write $\zeta(s) \equiv \zeta_0(s)$ which is the form of the well-known *dynamical ζ-function* [46] of Ruelle

$$\zeta^{-1}(s) = \prod_{p \in PPO} \left(1 - \frac{e^{-T_p s}}{\Lambda_p}\right) = \prod_{PPO} (1 - \tau_p) \tag{15.15}$$

15.2 Generalized Weights and the Topological Pressure

The weights in (15.15) can be regarded as a special case of a generalized weight function (for the strict derivation see [13])

$$\tau_p^A := \exp \int_0^{T_p} \left[A(\Phi_t(z_p)) - s\right] \, \mathrm{d}t \tag{15.16}$$

with a function $A : \Sigma_e \to \mathbb{C}$. To obtain the special case (15.14) one has to take

$$A = -\kappa^{(u)}(z) := -\frac{\mathrm{d}}{\mathrm{d}t}\Big|_{t=0} \ln \Lambda_z(t) \tag{15.17}$$

the local unstable Lyapunov exponent. Thus the integral in (15.16) becomes

$$\exp \int_0^{T_p} \left[-\kappa^{(u)}(\Phi_t(z_p)) - s\right] \, \mathrm{d}t = \Lambda_{z_p}^{-1}(T_p) \; e^{-sT_p} \equiv \Lambda_p^{-1} \; e^{-sT_p} \tag{15.18}$$

and the original weight of equation (15.14) is revealed. For an arbitrary weight function A the largest real pole of $\zeta_A(z)$ is called the *topological pressure* $P(A)$. Its existence was shown in [56]. For further purpose one choses a certain form for the function A

$$A_\beta \equiv -\beta \; \kappa^{(u)} \tag{15.19}$$

with a free parameter β and obtains the ζ-function and the topological pressure with respect to β

$$\zeta^{-1}_{-\beta \; \kappa^{(u)}}(z) \;\; =: \;\; \zeta_\beta^{-1}(z) = \prod_p \left[1 - \frac{\exp(-zT_p)}{\Lambda_p^\beta}\right] \tag{15.20}$$

$$P(-\beta \; \kappa^{(u)}) \;\; =: \;\; P(\beta) \tag{15.21}$$

For $\beta = 1$ thus the topological pressure $-P(1)$ denotes the classical escape rate. Typical shapes of the topological pressure for the 3-disk system and two different R/a parameters are shown in figure 61. Later in section 15.4 we will see, that also the root of the topological pressure has a crucial significance, indicating the Hausdorff dimension. An interesting property of

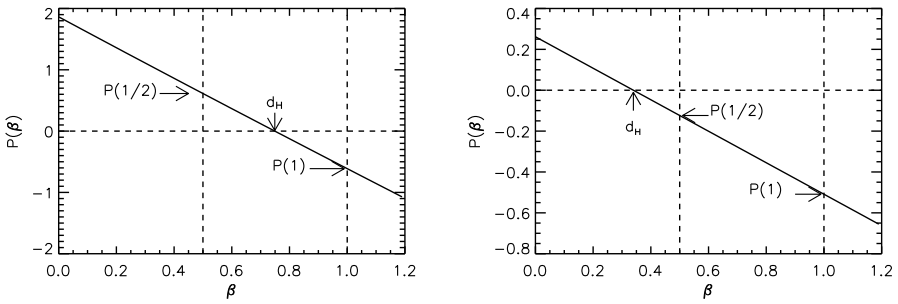

Figure 61: Topological Pressure (black solid line) for systems with $R/a = 2.2$ (left) and with $R/a = 4.5$ (right) and marks for $P(d_H) = 0$, $P(1/2)$ and $P(1)$

the distribution of imaginary parts of the resonances has been observed in [52]: Numerically they found a concentration at $\mathrm{Im}(k) = -\gamma_0/2 = P(1)/2$ that is at half of the classical escape rate. This corresponds to the classical expectation as the quantum mechanical probability density is the modulus square of the wave function [13]. Thus we compared the experimentally (and also numerically) derived resonance distributions with the calculated classical escape rate, see section 17.2.

15.3 Spectral Gap

In 1988 and 1989 Ikawa [45] and Gaspard/Rice [13] independently derived a connection between the topological pressure, being a purely classical quantity, and the quantum mechanical spectral gap. A spectral gap in this context is a constant $C < 0$ such that $\mathrm{Im}(k_n) \leq C$. Gaspard and Rice started from Gutzwiller's trace formula and used semiclassical zeta functions to conclude that $\mathrm{Im}(k_n) \leq P(1/2)$. They also confirmed this estimate numerically [13]. Later this estimate for the spectral gap has been also obtained mathematically for more general semiclassical systems [57]. It is, however, known that this bound is in general not optimal as it does not take into account phase cancellation (see section 8.2 in [58] and [59]). Some arguments for this bound on the spectral gap are given in appendix G.
Especially for weakly open systems this bound has no implication: As $P(\beta)$

is monotonously decreasing it is evident that for systems with $d_H > 1/2$ the bound $P(1/2)$ is positive (see figure 61 left), but the imaginary parts are negative anyway. Such systems are nowadays also called systems with "thick repeller" in contrast to systems with "thin repeller" where $d_H < 1/2$ and $P(1/2)$ is a true constraint on the imaginary parts (see e.g. [58]) (see figure 61 right). In section 17.2 we will compare the calculated values of the bound of the spectral gap with our experimentally derived resonance distribution.

15.4 Hausdorff Dimension and Counting Function

The famous Weyl formula states that the number of levels $N(k) := \{\#k_n : k_n \leq k\}$ is given by $N(k) = Vk^D/(D/2)!(4\pi)^{D/2} + \ldots$ for a system with volume V in a D-dimensional space [52] and especially for 2 dimensional billiard systems by

$$N_{\text{Weyl}}(k) = \frac{1}{4\pi}Ak^2 \pm \frac{1}{4\pi}Uk + c \tag{15.22}$$

where $\pm$ depends on the boundary condition: $+$ for Neumann and $-$ for Dirichlet boundary conditions. The constant c is defined by the curvature and the corners in the system [60]. The dimension of the billiard ($d = 2$) defines the leading exponent for large k. To transfer this concept on the n-disk systems we first need to generalize the standard idea of dimension, which relates points to the dimension zero, curves to dimension one and areas to dimension two. All these values are integer, but it turned out that there are sets, to which it is not possible to assign such an integer dimension for instance fractals like the famous cantor set. Thus there are additional ways to describe the dimension, which can relate even non-integer values to a set's dimension. Of course these new concepts must not be contradictory to the standard dimension. One new concept is introduced in the following: the Hausdorff dimension. Imagine a set in a d-dimensional space which is covered by d-dimensional spheres of radius $r < \epsilon$. The minimal number of spheres $N(\epsilon)$ needed to cover the entire set grows with decreasing ϵ. In the limit $\epsilon \to 0$ the number of spheres is supposed to grow as

$$N(\epsilon) \propto 1/\epsilon^{D_H} \tag{15.23}$$

where the exponent D_H is then called "Hausdorff dimension". Accordingly to the Weyl law for closed systems Sjöstrand presented a conjecture about a *fractal* Weyl law in 1990 [61], which attracted much attention thanks to a second publication in 2003 by Lu, Sridhar and Zworski [52] who additionally confirmed it numerically:

For open systems where eigenvalues turn into complex resonances $\tilde{k}_n = \mathrm{Re}\tilde{k}_n + i\mathrm{Im}\tilde{k}_n$ the counting statistics of resonances is typically defined by

$$N(k) := \#\{\tilde{k}_n : \mathrm{Im}\,\tilde{k}_n > -C,\ \mathrm{Re}\,\tilde{k}_n \leq k\} \tag{15.24}$$

where C is a fixed finite positive constant, which should not be too small. The fractal Weyl law now states the proportionality for $k \to \infty$

$$N(k) \propto k^{1+d_H} \quad \Leftrightarrow \quad \ln N(k)/\ln k \propto 1 + d_H \tag{15.25}$$

where $d_H = (D_H - 2)/2$ is the partial Hausdorff dimension of the repeller. In [52] they give several mathematical arguments and confirm this conjecture by some computations of n-disk systems. A short summary of intuitive arguments and the relation between partial and global Hausdorff dimension is given in appendix E. In section 17.3 the counting of our experimental resonances is described and the found slope of $\ln N(k)/\ln k$ is compared with theoretical values: As explained e.g. in [62] the reduced Hausdorff dimension d_H of the fractal repeller is given by the condition $P(d_H) = 0$. In appendix F a heuristic derivation for that is presented.
To find the root of the topological pressure seems to be very laborious at first glance: Applying a Newton algorithm on $P(\beta)$ means a lot of calculations as for every value of it the root of $\zeta_\beta^{-1}(s)$ must be found. But at second sight it gets clear that finding a root of ζ in s, which is again supposed to be zero, is equivalent of finding directly the root of

$$\zeta_\beta^{-1}(0) = \prod_p \left[1 - \frac{1}{\Lambda_p^\beta}\right] \tag{15.26}$$

which is obviously much easier to evaluate numerically and will thus be used for calculating the Hausdorff dimension for our system in section 17.3.

15.5 Semiclassical ζ-Function

Gaspard and Rice also derived a semiclassical zeta function in [46] starting from Gutzwiller's trace formula using a Green's function formalism

$$\zeta_{\mathrm{sc}}^{-1}(z) = \prod_p \left(1 - \frac{1}{\sqrt{\Lambda_p}} \exp(izT_p + in_p\pi)\right) \tag{15.27}$$

with length T_p, stability Λ_p and word length n_p of the periodic orbits. The poles of this zeta functions are supposed to coincide with the exact quantum mechanical ones in the semiclassical limit. Figure 62 shows the semiclassical

resonances in orange dots and the quantum mechanical ones as black crosses (their calculation will be explained in appendix I), revealing a good agreement even for small Re ka. Resonances deep in the complex plane with $\mathrm{Im}(k_n) < -0.8$ do not show this agreement because of convergence problems of the calculations of the zeta function. Here it would be necessary not only to take into account orbits until order $n = 8$, but much higher orders or even instead of $\zeta_{\mathrm{sc}}^{-1}(z)$ the full Selberg product according to equation (15.13). But

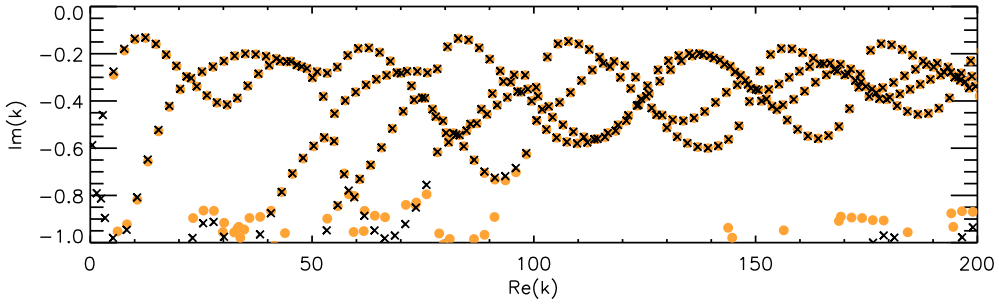

Figure 62: Semiclassical resonances of the 3-disk system $R/a = 4.5$ (orange dots) calculated up to order $n = 8$ in good agreement with quantum mechanical resonances (black crosses)

to test low lying resonances with large imaginary parts (particularly with regard to the resonances gap, see section 17.2) for much higher energies as it will be possible for the quantum mechanical numerics this function is very convenient.

15.6 Convergence of Algorithm and Cycle Expansion

If one wants to compute the classical or semiclassical ζ-function one faces the problem of dealing with the infinite product

$$\zeta_\beta(z)^{-1} = \prod_p [1 - t_p] \tag{15.28}$$

where t_p is the abbreviation for the orbits weights, defined in (15.20) respectively (15.27). Truncating it like $\prod_p [1 - t_p] \approx (1 - t_1) \dots (1 - t_n)$ with $1 \dots n$ just numbering period orbits would only lead to a very slow convergence. In 1989 Cvitanović and Eckhardt [14] presented the cycle expansion, an effective and well converging way of its calculation: Instead of truncating the product, they expanded it and then truncated the sum after a finite word length

(concerning the reduced code in the fundamental domain). The convergence of the numerics is surprisingly good and already for second order convenient [14]. For the 3-disk binary code it is explained in detail in [14], [50] and [49]: But there seems to be no reference dealing with the 5-disk case, thus we will present it here as an illustrating example: In section 14 it was found that we need the four symbols $1, 2, \underline{1}, \underline{2}$ to describe all the period orbits in the 5-disk fundamental domain. Thus the ζ-function becomes (up to order 2)

$$\begin{aligned} \zeta^{-1} &= (1-zt_1)(1-zt_2)(1-zt_{\underline{1}})(1-zt_{\underline{2}})(1-zt_{12}) \\ &\quad (1-zt_{1\underline{1}})(1-zt_{1\underline{2}})(1-zt_{2\underline{1}})(1-zt_{2\underline{2}})(1-zt_{\underline{12}})\ldots \end{aligned} \tag{15.29}$$

where z is a book keeper variable to indicate the total word length and will be set to one in the final evaluation. Now the product is expanded and the terms are reorganized such that the terms of the same power of z (i.e. the same total word length) are grouped together leading to

$$\begin{aligned} &\approx 1 - zt_1 - zt_2 - zt_{\underline{1}} - zt_{\underline{2}} + z^2t_1t_2 + z^2t_1t_{\underline{1}} + z^2t_1t_{\underline{2}} + z^2t_2t_{\underline{1}} \\ &\quad + z^2t_2t_{\underline{2}} + z^2t_{\underline{1}}t_{\underline{2}} - z^2t_{12} - z^2t_{1\underline{1}} - z^2t_{1\underline{2}} - z^2t_{2\underline{1}} - t_{2\underline{2}} - z^2t_{\underline{12}} \end{aligned} \tag{15.30}$$

$$\begin{aligned} &= 1 - z(t_1 + t_2 + t_{\underline{1}} + t_{\underline{2}}) + \\ &\quad z^2\left[(t_1t_2 - t_{12}) + (t_1t_{\underline{1}} - t_{1\underline{1}}) + (t_1t_{\underline{2}} - t_{1\underline{2}}) + (t_2t_{\underline{1}} - t_{2\underline{1}}) + (t_2t_{\underline{2}} - t_{2\underline{2}}) + (t_{\underline{1}}t_{\underline{2}} - t_{\underline{12}})\right] \end{aligned} \tag{15.31}$$

This grouping of terms reveals that every parenthesis includes the difference between a longer orbit and the combination of its shorter "shadowing" orbits. This behavior is illustrated in figure 63. Here it becomes visible that the

Figure 63: Periodic orbits in the fundamental domain (shaded region) of the 5-disk system: left: orbit $\underline{1}1$ (black) with shadowing orbits $\underline{1}$ and 1 (red dashed); right: orbit $\underline{12}$ with the shadowing orbits $\underline{1}$ and $\underline{2}$

orbits $\underline{1}$ and 1 (red dashed) approximate the longer orbit $\underline{1}1$ (black) in the left picture and that the orbits $\underline{1}$ and $\underline{2}$ (red dashed) approximate $\underline{12}$ (black)

in the right. This is also true for the other orbit combinations, even for longer ones [14]. These approximations will lead to an appropriate canceling of the terms in parenthesis. Thus the correction decays exponentially with orbit length [50]. This mechanism makes the cycle expansion so successful and often doubles the number of significant digits for a given cycle length as compared to other methods [14]. It is worth mentioning that the ζ-function is thus dominated by short orbits of the word length 1 as these are the fundamental ones with which the other orbits are approximated and as these have –of course– no shorter partners to cancel out.

15.7 Factorization of the ζ-Function

The discrete symmetries of the geometry of the n-disk system can help to simplify the treatment of the dynamics even more. A very detailed description is given in [50] and its main ideas for the example of the 3-disk system will be repeated in the following, as we take benefit from them in the implementation of the ζ-function. Let $G = \{e, g_2, g_3, \dots g_g\}$ be the symmetry group under which our system is invariant. For the 3-disk case we have $C_{3v} = \{e, \sigma_{12}, \sigma_{23}, \sigma_{31}, C_3, C_3^2\}$, the identity, reflections with respect to axes and rotations by $2\pi/3$ and $4\pi/3$, respectively, illustrated in figure 64. Let us

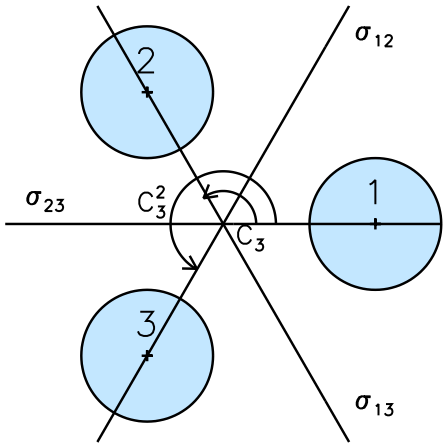

Figure 64: Full 3-disk system with symmetry axes

first reduce the number of independent cycles by means of the symmetries: For cycles p those discrete symmetries mean that there can exist subgroups

$\mathcal{H}_p$ of G of order h_p, whose elements leave the cycle invariant. The weight of a cycle t_p remains invariant under any symmetry transformations g. The elements of the quotient space $b \in G/\mathcal{H}_p$ generate degenerate cycles bp with a multiplicity of $m_p = g/h_p$. Thus the product in equation (15.28) can be rewritten as

$$\prod_p [1 - t_p] = \prod_{\hat{p}} [1 - t_{\hat{p}}]^{m_{\hat{p}}} \tag{15.32}$$

where $\hat{p}$ is only one representative per class of $m_{\hat{p}}$ degenerate cycles. In our example the group C_{3v} subdivides into $C_e = \{e\}$ (dimension $h_e = 1$), $C_v = \{e, \sigma_i\}$ (dimension $h_{C_v} = 2$) and $C_3 = \{e, C_3, C_3^2\}$ (dimension $h_{C_3} = 3$) leading to possible cycle multiplicities of $g/h_{C_3} = 2$ (e.g. for cycles $\overline{123}$ and $\overline{132}$), $g/h_{C_v} = 3$ (e.g. $\overline{1213}$) and $g/h_e = 6$ (e.g. $\overline{12123}$, which has no symmetry). In the next step it is shown that all computations can be restricted to the fundamental domain, as each global cycle p corresponds to a fundamental domain cycle $\hat{p}$. The global phase space M can be presented by the fundamental domain $\tilde{M}$ and its images under the action of the symmetry group $a\tilde{M} \equiv M_a$, $b\tilde{M} = M_b$, ... Let us assume orbit segments starting in M_a and ending in M_b, then $h = ab^{-1}$ is the symmetry operation mapping the endpoint domain onto the starting point domain. Its left regular representation $D(h)$ is a $g \times g$ matrix with entries $D(h)_{ab} = 1$ if $a = hb$ and zero otherwise. $D(h)$ thus maps a tile M_a to a different tile $M_{ha} \neq M_a$ (for $h \neq e$). However, there are boundary points left invariant under this transformation, e.g. σ_{12}, the reflection across an axis, leaves the axis itself invariant. It is important that $\mathrm{Tr} D(h) = g\delta_{h,e}$ is only non-zero for $h = e$, as only $D(e)$ has diagonal elements. Next each factor in the product (15.28) will be related to the left regular representation $D(h)$ by the same means as in the derivation of the ζ-function in section 15.1, but here for an orbit $\tilde{p}$ in the fundamental domain and $h_{\tilde{p}}$ an element of $\mathcal{H}_p$, the symmetry group of p:

$$\begin{aligned}
\det(1 - D(h_{\tilde{p}})\, t_{\tilde{p}}) &= \exp \mathrm{Tr} \ln(1 - D(h_{\tilde{p}})\, t_{\tilde{p}}) \qquad (15.33)\\
&= \exp\left(-\sum_{n=1}^{\infty} \frac{\mathrm{Tr}(D(h_{\tilde{p}}^n)\, t_{\tilde{p}}^n)}{n}\right)\\
\text{with } k \text{ defined by } h_{\tilde{p}}^k = e \qquad &= \exp\left(-\sum_{n=1}^{\infty} \frac{\mathrm{Tr}(D(h_{\tilde{p}}^{kn})\, t_{\tilde{p}}^{kn})}{kn}\right)\\
&= \exp\left(-\sum_{n=1}^{\infty} \frac{\mathrm{Tr}(D(e^n)\, t_{\tilde{p}}^{kn})}{kn}\right)\\
&= \exp\left(-\sum_{n=1}^{\infty} \frac{g\, t_{\tilde{p}}^{kn}}{kn}\right)
\end{aligned}$$

$$\begin{aligned} &= \exp\left(-\frac{g}{k}\sum_{n=1}^{\infty}\frac{(t_{\tilde{p}}^k)^n}{n}\right) \\ &= \exp\left(\frac{g}{k}\ln\left(1-t_{\tilde{p}}^k\right)\right) \\ &= \left(1-t_{\tilde{p}}^k\right)^{g/k} \end{aligned}$$

Here $t_{\tilde{p}}^k = t_p$ relates the weight of the orbit in the fundamental domain $\tilde{p}$ with the global orbit p and $g/k = m_p$, the multiplicity of the orbit, thus we are in accordance with (15.32). This identity is valid cycle by cycle in (15.28). As we know from the symmetry considerations above $D(h)$ decomposes in d_α dimensional blocks of irreducible representations $D(h) = \oplus_\alpha\, d_\alpha D_\alpha(h)$. Thus the determinant (15.33) factorizes as

$$\det(1 - D(h)\ t) = \prod_\alpha \det(1 - D_\alpha(h)t)^{d_\alpha} \tag{15.34}$$

Regarding the transfer operator this factorization means that it reduces to block diagonal form, every block belonging to the invariant subspace. The ζ-function now finally factorizes as

$$\begin{aligned} \zeta^{-1} &= \prod_p (1 - t_p) \\ &= \prod_{\tilde{p}} \det(1 - D(h_{\tilde{p}})\ t_{\tilde{p}}) \\ &= \prod_{\tilde{p}}\prod_\alpha \det(1 - D_\alpha(h_{\tilde{p}})\ t_{\tilde{p}})^{d_\alpha} \\ &= \prod_\alpha \underbrace{\prod_{\tilde{p}} \det(1 - D_\alpha(h_{\tilde{p}})\ t_{\tilde{p}})^{d_\alpha}}_{\equiv\left(\frac{1}{\zeta_\alpha}\right)^{d_\alpha}} \end{aligned}$$

The determinants of the d-dimensional irreducible representations can be evaluated using an expansion in terms of traces, for our example with one- and two-dimensional representations we obtain in terms of group characters

$$\begin{aligned} \det(1 - D_\alpha(h)\ t) &= 1 - \chi_\alpha(h)t \qquad \text{for one dim.} \\ \det(1 - D_\alpha(h)\ t) &= 1 - \chi_\alpha(h)t + \frac{1}{2}\left(\chi_\alpha^2(h) - \chi_\alpha(h^2)\right)t^2 \qquad \text{for two dim.} \end{aligned}$$

Now we can easily write down the exact factorization of the ζ-function $\zeta = \zeta_{A_1}\zeta_{A_2}\zeta_E^2$ with the two one-dimensional representations A_1 and A_2 and the

two-dimensional representation E for our example using the character table 5.

C_{3v}	A_1	A_2	E
e	1	1	2
C_3, C_3^2	1	1	-1
σ	1	-1	0

Table 5: Character table for C_{3v}

Thus equation (15.34) becomes

$$\det(1 - D(h)\ t) = (1 - \chi_{A_1}(h)t)\ (1 - \chi_{A_2}(h)t)\ \left(1 - \chi_E(h)t + \chi_{A_2}(h)t^2\right)^2$$

with $\chi_{A_2}(h) = \frac{1}{2}(\chi_E^2(h) - \chi_E(h^2))$ for every group element h. For orbits $t_{\tilde{p}}$ belonging to symmetry e we obtain with $g = 6$ and $k = 1$ from (15.33)

$$\begin{aligned} e: \quad (1 - t_{\tilde{p}})^6 &= (1 - t_{\tilde{p}})\ (1 - t_{\tilde{p}})\ \left(1 - 2t_{\tilde{p}} + t_{\tilde{p}}^2\right)^2 \\ \text{For the rotations i.e. } k = 3 & \\ C_3, C_3^2: \quad \left(1 - t_{\tilde{p}}^3\right)^2 &= (1 - t_{\tilde{p}})\ (1 - t_{\tilde{p}})\ \left(1 + t_{\tilde{p}} + t_{\tilde{p}}^2\right)^2 \\ \text{For the reflection we have with } k = 2 & \\ \sigma: \quad \left(1 - t_{\tilde{p}}^2\right)^3 &= (1 - t_{\tilde{p}})\ (1 + t_{\tilde{p}})\ \left(1 + 0t_{\tilde{p}} - t_{\tilde{p}}^2\right)^2 \end{aligned}$$

The terms in the first parentheses always belong to the A_1 representation, where we observe that it is given by the standard binary expansion as all characters are equal to 1

$$1/\zeta_{A_1} = (1{-}t_0)\,(1{-}t_1)\,(1{-}t_{10})\,(1{-}t_{001})\,(1{-}t_{011})\,(1{-}t_{0001})\,(1{-}t_{0011})\,(1{-}t_{0111})\ldots$$

The second pair of parentheses represents A_2 with

$$1/\zeta_{A_2} = (1{+}t_0)\,(1{-}t_1)\,(1{+}t_{10})\,(1{-}t_{001})\,(1{+}t_{011})\,(1{+}t_{0001})\,(1{-}t_{0011})\,(1{+}t_{0111})\ldots$$

where every orbit with an odd number of zeros gets an extra minus sign. The third parentheses belong to E and lead to the following zeta function

$$1/\zeta_E = (1 + t_1 + t_1^2)\ (1 - t_0^2)\ (1 + t_{100} + t_{001}^2)\ (1 - t_{10}^2)\ (1 + t_{1001} + t_{1001}^2)\ldots$$

Regarding our experiments in which we realize the fundamental domain with Dirichlet boundary conditions at the symmetry axes (the detailed description can be found in section 16.1) that means that though the setup obeys the A_2 symmetry of the full system, we have to consider the ζ-function for the

A_1 case: Because this factor ζ_{A_1} of the symmetry decomposition of the full system equals the full ζ-function of the fundamental domain system, which is the one we realized. Hence all the quantities like e.g. the classical escape rate obtained from a ζ-function which are compared to any experimental result are computed for the A_1 representation.
Up to what order it is necessary to compute the ζ-function for our purpose and which role the pruning plays for the convergence is presented on a technical level in the next section.

16 Experimental Setup and Resonance Extraction

16.1 The Experiments

In the experiments we realized the quantum version of the symmetry reduced 3- and 5-disk system using a microwave cavity. To maintain the clearness in the text we will often refer to a n-disk system, also here in the experimental part, instead of writing "3-disk and 5-disk system, respectively". In both experiments the baseplate is an aluminum triangle whose largest side is 100 cm long. Two sidewalls with a height of 6 mm are set atop, including an angle of 60° for the 3-disk, and 36° for the 5-disk system, respectively. Thus the resonator forms the fundamental domain of the n-disk system with metallic sidewalls, which act as mirrors reducing the symmetry of the system: Those walls induce Dirichlet boundary conditions for the electric field of the TM_0 mode, thereby restricting the measurements to a single representation A_2 of the underlying symmetry group C_{nv} (see sketches on the left of figures 65 and 66) as explained in section 14. The advantage of this symmetry reduction is of course the access to a much larger system as it would be realizable in a full symmetry construction, additionally the degeneracies due to the symmetries are lifted. The third side of the cavity is left open, but additionally covered with a wide strip of microwave absorber. In the case of the 3-disk system it is a serrated absorber of the same height as the cavity Those measurements were performed by Alexander Potzuweit in his Diploma thesis [63]. In the newer measurements of the 5-disk system a reticular absorber material with smoothly increasing height was used. The absorbers were tested and developed by Tobias Weich during his Diploma thesis [64] and the measurements were performed by myself. Both absorber shapes aim to avoid any reflections at the open end, imitating infinity.
The R/a parameter can be adjusted by moving a half-disk inset of radius $a = 19.5\,\text{cm}$, which is in contact with top and bottom plate, along the one metallic side wall. In the 3-disk system the R/a range between 2.26 and 6.17 was technically accessible, in the 5-disk case we were able to reach values between 2 and 3.9, both with a stepwidth of $\Delta R = 10\,\text{mm}$. A thin wire antenna (r=0.7 mm), which is sufficiently short not to touch the bottom plate, is inserted through a hole in the top plate (not shown in the photographs in figures 65 and 66), placed in between the acute angle of the aluminum walls and the movable disk inset. The position is chosen such that the antenna is not too close to the walls and is not touched by the disk inset even for the smallest accessible R/a values. Thus always a coupling to the interior of

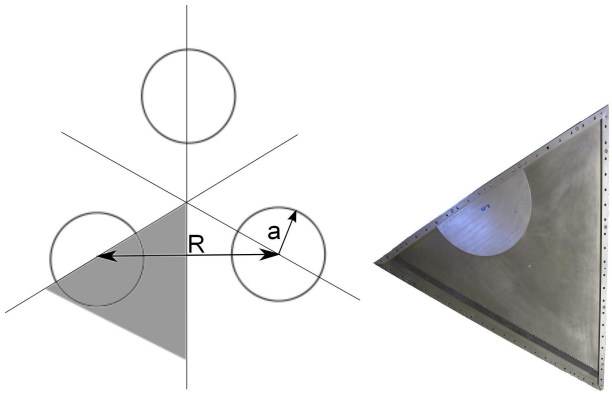

Figure 65: Sketch of 3-disk system with shaded fundamental domain, the disk radius is denoted by a, the disk distance by R and photograph of the experimental cavity with disk inset and absorber of first type (top plate removed)

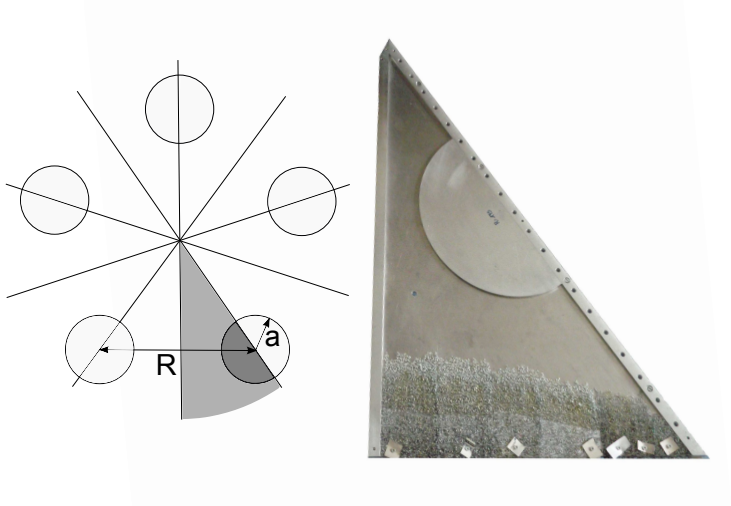

Figure 66: On the left of this figure a sketch of the full 5-disk scattering system is given. The gray shaded part indicates the fundamental domain of the symmetry reduction. On the right side a photograph of the experimental setup is presented (top plate removed). The reticulated absorber (second type) is fixed at the third open side of the cavity

the scattering system is guaranteed, where the long-living states exist. The whole setup is covered by a second aluminum plate of the same size and

shape as the bottom plate that is screwed onto the billiard walls leaving no gaps or slits.
The reflection coefficient is then measured with a vector-network-analyzer (VNA), revealing the complex S-matrix. The height of the cavity $h = 6\,\mathrm{mm}$ (along the vertical z-direction) leads to a cutoff frequency of 25 GHz. By limiting the frequency range to be analyzed to 24 GHz we thus make sure that only the TM_0 mode can propagate and the cavity may be considered as two-dimensional. Under the assumption of a point-like antenna the measured reflection signal is of the form [65]

$$S_{11}(\nu) = 1 + \sum_j \frac{\tilde{A}_j}{\nu^2 - \nu_j^2} \tag{16.1}$$

where the ν_j are the complex valued resonance positions. As we are interested in the complex resonance positions we need to extract ν_j and $\tilde{A}_j$ from the experimental signal: For closed systems and low frequencies the resonances are well separated and could be treated by a multi-Lorentz-fit. But for open systems, where the resonances overlap strongly, a fit would not converge. Therefore a more sophisticated method is needed.

16.2 Data Analysis by Means of the Harmonic Inversion

In figure 67 the spectra for three different R/a parameters of the 5-disk system are shown. For the closed system (R/a=2, black solid line) even in the high frequency regime some separate resonances are visible. For R/a=2.25 the opening between the half circle and the straight wall is approximately 24 mm. Thus the opening supports approximately 4 modes in the shown frequency range and the resonances can still be recognized but are sufficiently broadened (red dotted line). By further increasing the opening (R/a=3.83, blue dashed line) the resonances become strongly overlapping. In order to extract the resonances from this frequency signal we use the Harmonic Inversion (HI) algorithm as it has been presented by Main et al. [66] in 2000. It was already applied in our group on experimental data by Kuhl et al. [67] to determine the line width distributions in slightly open cavities with antenna and wall absorption. To illustrate the challenges of applying this algorithm to experimental data, I first give a short summary of the algorithm and refer to [66, 67] for further details. Afterwards I present some additional procedures around the application of the HI to circumvent the occurring problems. A lot of investigation of the limits of the HI applied on our experimental data was already performed by Tobias Weich [64]. The implementations of the

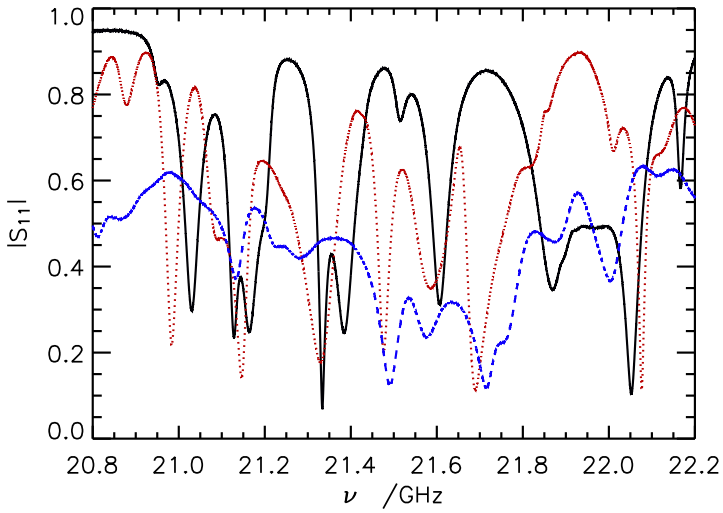

Figure 67: The plot shows measured reflection spectra for the closed system $R/a = 2$ (black solid line), a system in the transition region with $R/a = 2.25$ (red dotted line) and an open system with $R/a = 3.83$ (blue dashed line).

procedures of data analysis based on the improved HI method and the investigation of the presented experimental data with the new tool was done in the scope of this thesis.

For all studied resonances one has $|\mathrm{Re}(\nu_j)| \gg |\mathrm{Im}(\nu_j)|$, thus equation (16.1) can be approximated by

$$\frac{\tilde{A}_j}{\nu^2 - \nu_j^2} = \frac{\tilde{A}_j}{(\nu - \nu_j)(\nu + \nu_j)} \approx \frac{A_j}{\nu - \nu_j} \tag{16.2}$$

with $A_j = \frac{\tilde{A}_j}{2\nu_j}$. This leads to

$$S_{11}(\nu) = 1 + \sum_j \frac{A_j}{\nu - \nu_j}, \tag{16.3}$$

which is more convenient in the following.
The HI algorithm consists of 4 steps: windowing, truncating the Fourier transformed signal, Padé approximation and finally filtering. In the first step the large measured signal is divided into overlapping windows. This is necessary to reduce the number of resonances in each window, which then will be analyzed separately. Otherwise it is not possible to apply the Padé approximation. In order to reduce boundary effects of the signal division,

only those extracted resonances within a given range $\Delta\nu_r$ in the center of each of the windows will be taken into account. The windows must therefore overlap. In the following I use $\Delta\nu_r$=1 GHz with an overlapping region of 1 GHz on each side leading to a total window size of 3 GHz. Here a rectangular windowing is the most suited as in other window shapes, like Cosine or Hamming, the data points in the center obtain a higher weight than those closer to the edges which is not wanted for the further treatment. Applying

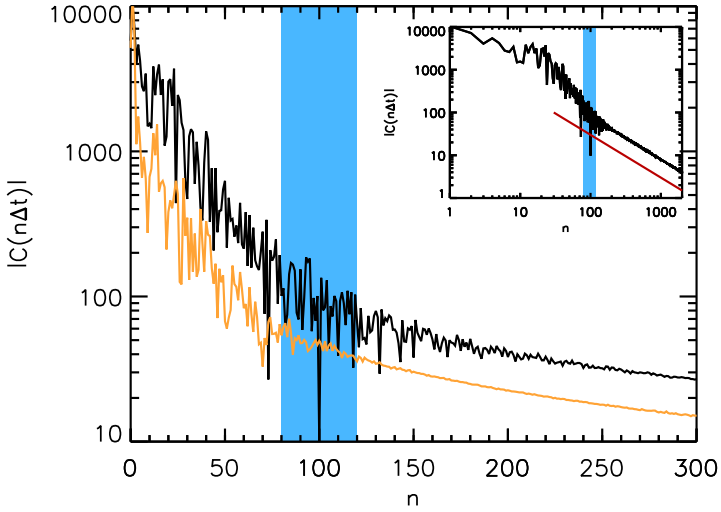

Figure 68: This figure shows the fast Fourier transform of the reflection signal of the frequency window from 20 to 23 GHz for the closed ($R/a = 2$, upper black curve) and an open ($R/a = 3.83$, lower orange curve) 5-disk system. The unit of the x-axis is the number of data points of this discrete time signal. The inset shows the decay for the closed system in a double logarithmic plot. The red straight line corresponds to an $1/n$-decay. The light blue shaded region indicates the variation of the cutoff parameter between 80 and 120 data points, which is used in the data analysis described in the text.

a fast Fourier transform (FFT) to each measured window of 3 GHz width and a step-width of 0.1 MHz we obtain a discrete time series of 30 000 data points. Using (16.3) and neglecting the window effects and experimental uncertainties, the ideal FFT signal is given by

$$C(t) = \delta(t) + \sum_j d_j e^{-2\pi i \nu_j t}. \tag{16.4}$$

In open systems the resonance frequencies have a negative imaginary part and $C(t)$ decays exponentially with t. In figure 68 examples for two R/a

parameters are shown. The decay at the beginning given by a sum of exponentials is due to the widths of the resonances and then changes to an $1/n$ decay, the windowing effect of the rectangular cut of the signal (see the inset). The relevant information of the decay is hence contained in the first part of the time signal. By truncating the time signal after N_{trunc} data points we make sure that the number of data points is not too large for the Padé approximation. As it will be crucial in the sequel that the analyzed time series is of form (16.4) it is important that one cuts off the signal before the $1/n$ decay takes over. On the other hand N_{trunc} should also be chosen sufficiently large such that the relevant information is contained in the truncated signal. Figure 68 shows that for the analyzed microwave spectra and a total window size of 3 GHz a truncation between $N_{\text{trunc}} = 80 \ldots 120$ is reasonable, see shaded region.
After this truncation an equidistant discrete time series of N_{trunc} data points $C(\Delta t \cdot n) = \sum_j d_j e^{-2\pi i \nu_j \Delta t \cdot n}$ with $n = 0 \ldots N_{\text{trunc}} - 1$ remains and the central idea is now to interpret this signal as a system of nonlinear equations of the form

$$c_n = \sum_{k=1}^{N_{\text{trunc}}/2} d_k z_k^n \quad \text{with } n = 0 \ldots N_{\text{trunc}} - 1 \tag{16.5}$$

which is solved by the Padé approximation [66, 68]. A consequence of this

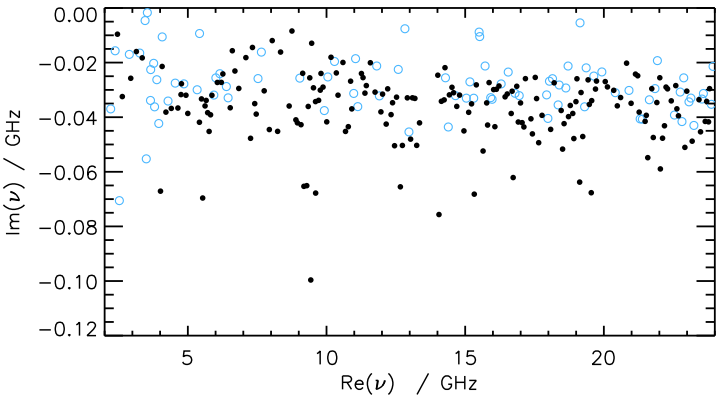

Figure 69: This figure shows the resonances of the 5-disk system with $R/a = 3.83$ in the complex plane obtained via the HI for one set of parameters. The light blue circles are resonances that are removed by the filter, whereas the black dots correspond to the remaining resonances.

approach is that $N_{\text{trunc}}/2$ determines the number of resonances which are returned by the Padé approximation. Choosing this parameter according to the criteria discussed above $N_{\text{trunc}}/2$ will be larger than the true number of

resonances and the Padé approximation will generate spurious resonances which have to be filtered out. There are two filter mechanisms: (i) The Padé approximation is performed a second time with a time signal shifted by one point, i.e. $C(\Delta t \cdot n)$ with $n = 1 \ldots N_{\mathrm{trunc}}$. Resonances that are unstable concerning a minimal tolerance ("pointError") are rejected. (ii) Only resonances whose heights $\frac{|A_j|}{|\mathrm{Im}\nu_j|}$ exceed sufficiently the noise level of < 0.005 are accepted ("HiFilter"). The noise can be observed e.g. in the black line in figure 67. For the data analyzed in this thesis we set this filter to 0.05. The effect of the filtering is illustrated in figure 69. Without filtering the HI returns too many resonances, especially there appear resonances with very small widths which are not realistic for such an open system. After filtering, only the resonances shown as black dots survive and the other resonances (light blue circles) are sorted out. For the remaining resonances a spectral gap and a conglomeration around $\mathrm{Im}(\nu) \approx -0.03$ can be observed. We will see later in section 17.2 that this corresponds to half the classical escape rate $-\gamma^{\mathrm{5Disk}}_{R/a=3.83} \cdot 0.5 = -0.031\,\mathrm{GHz}$.

The description of the algorithm above shows that the HI-algorithm requires the fixing of several parameters, such as N_{trunc} or the window overlap. T. Weich tested in his Diploma thesis [64] that for ideal (numerical) data of the form of equation (16.3) the HI results are independent on the exact parameter choice as long as they are in a plausible range. But this assumption will never be exactly true for experimental data due to inevitable experimental noise and errors which lead to the problem, visualized in figure 70. Here the measured microwave spectrum for $R/a = 3.83$ (black solid line) was analyzed by the harmonic inversion in order to extract the resonances in the valid range between 21 and 22 GHz. Therefore the HI was applied to the data with 160 different parameter sets by varying N_{trunc} between 80 and 120 – as discussed above– and changing the buffer region on both sides between 1 and 0.98 GHz, respectively. According to figure 68 all these parameter sets are plausible. If the complex resonance positions of these 160 HI results are plotted in one plot (light blue dots in the lower part of figure 70) one observes that the resonances of the different parameter sets form clusters in the complex plane but are not equal. If one pursues, however, an individual result of a particular parameter set marked by the red circles one observes, that for this parameter set several clusters are missing. For other parameter sets nearly all the clusters within the valid interval matches with the individual resonances. The blue triangles mark one example. So which parameter set is the correct one?

One reasonable criterion is the reconstruction of the original signal with the found resonances (and their amplitudes): Suppose one is interested in reso-

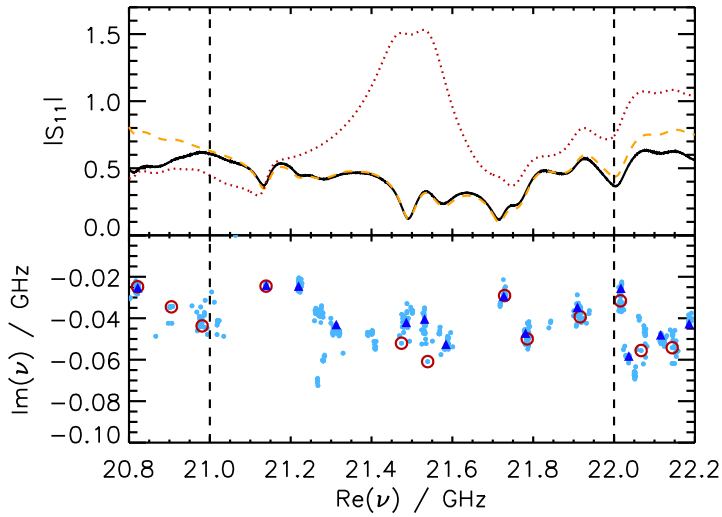

Figure 70: The upper plot shows the measured microwave spectrum ($R/a = 3.83$) (black solid line) as well as two reconstructions obtained by the HI results for two different parameter sets (orange dashed and red dotted lines). The lower plot shows the corresponding complex resonance positions. The red circles correspond to the resonances of the reconstructed signal shown above as red dotted line and the blue triangles to the orange dashed line. Light blue dots represent the resonance positions of the HI results for all parameter sets. The two vertical dashed lines mark the valid range of the analyzed window.

nances in the frequency interval from 21 to 22 GHz as in figure 70 and has chosen to take the overlap on each side to be 1 GHz. The HI Algorithm thus analyzes the whole interval from 20 to 23 GHz. As a result it returns a set of resonances and amplitudes $\{(\nu_j, A_j)\}$. The superposition $\sum_j \frac{A_j}{\nu-\nu_j}$ is now compared with the measured signal $S_{11}(\nu)$ between 21 and 22 GHz. Note that all the resonances in the large window ranging between 20 and 23 GHz are contained in the superposition. But what about resonances outside this window and very broad resonances which cannot be extracted from the signal? Here we approximate their influence by a complex valued linear function over the size of the valid region. Such a background function is thus fitted to the difference between superposition and measured signal. The result of the full reconstruction (which now contains the superposition of Lorentzians and the fitted background) is plotted in the upper part of figure 70. While the reconstructed signal (orange dashed line) of one set of resonances (blue triangles) agrees well with the measured data, the deviation of another reconstruction (red dotted line) using the other set (red circles) is enormous.

It is clear that thus one set of resonances is more reliable than another one depending on their reconstruction.
This finding led us to the general proceeding of data analysis used in the following sections: As it is not sufficient to use only one parameter set for applying the HI on such kind of experimental data and, as even the set leading to the best reconstruction may overlook single resonances, we perform the HI for many parameter sets, calculate the reconstructions in the described way, reject those with unconvincing reconstruction by means of their χ^2 value and average over all the others. The used parameters are given in table 6. Of

measured frequency range:	$1 - 25\,\mathrm{GHz}$
window size:	$1\,\mathrm{GHz}$
overlap of windows:	$1\,\mathrm{GHz}$
total window size:	$3\,\mathrm{GHz}$
number of windows:	22
accessible frequency range:	$2 - 24\,\mathrm{GHz}$
N_{trunc}:	$80 \ldots 120$
shift of overlap region:	$0.02\,\mathrm{GHz}$
total number of parameter sets:	160
point error:	0.01
HI filter:	0.05
reconstruction tolerance:	χ^2 error $<$ variance of the signal

Table 6: HI parameters

course this averaging process does only make sense for statistical properties as counting function or probability distributions $P(\mathrm{Im}(k))$. But these are the quantities we focus on. The averaging process is described in detail in the corresponding text passages of the next section, tests of its robustness are given as well.

17 Experimental Results

17.1 Resonances of the 3-Disk System

For the 3-disk system there is a second way to test the reliability of the HI by comparing the experimentally obtained resonances with the theoretical ones. For the symmetry reduced 3-disk system the resonances were calculated by the algorithm of Gaspard and Rice [51], see appendix I.
One remark in advance concerning the expected agreement of the individual resonances: Even for experiments with closed microwave systems it is known that only the low lying resonances agree well with the theoretical predictions. But the spectrum is not very robust: For higher frequencies the experimental perturbations (antenna, misalignments,...) will disturb it such that the individual measured resonances cannot be associated anymore directly to the theoretical ones. However statistical properties such as the resonance density persist. In this case for the open 3-disk system we expect this effect to be even more significant since the spectra of non hermitian Hamiltonians are known to be even much more unstable under perturbations compared to hermitian Hamiltonians [69].
Figure 71 shows the good HI-resonances in orange respectively blue (the best one) for $R/a = 5.5$ and in the full measured Re(k)-range from 40 to 500 m^{-1} corresponding to frequencies between 2 and 24 GHz. Again the orange poles form "clouds" around the blue triangles –the drawn-out shape of the clouds is a consequence of the non isometric axis ranges. The black crosses indicate the numerically calculated resonances. The composition of resonance chains is typical for large R/a parameters [51, 52, 55]. As expected the individual resonance structure is not reproduced by the experimental data. So let's have a look at a statistical quantity: the distribution of the imaginary parts $P(\mathrm{Im}(k))$.
They are shown in the right part of figure 71, in black the calculated and in blue for the experimental spectrum. Both distributions show up to be the same within the limits of error. The same was true for the other good resonance sets. All the distributions shown below have hence been obtained by superimposing the results of all good reconstructions, calling it simply $P(\mathrm{Im}(k))$ without extra indicating the averaging. The example corresponding to this R/a parameter is shown in the right hand part of figure 71 in orange, it looks also very similar to the other two distributions. $P(\mathrm{Im}(k))$ is robust with respect to errors in the reconstruction as long as the number of resonances entering the reconstruction can be determined reliably and the fluctuations of resonance positions can be assumed to be Gaussian and independent. For the example shown in figure 71 the number varied between 94

for the numerical data and 117 for the individual reconstruction, a precision of about 20%. For all three histogramms we find a very good agreement with the bound of $P(1/2)$ for the spectral gap (dashed black line in the right hand side of the figure) and classical escape rate ($-\gamma_{\mathrm{cl}}/2$ = solid black line) for the maxima.

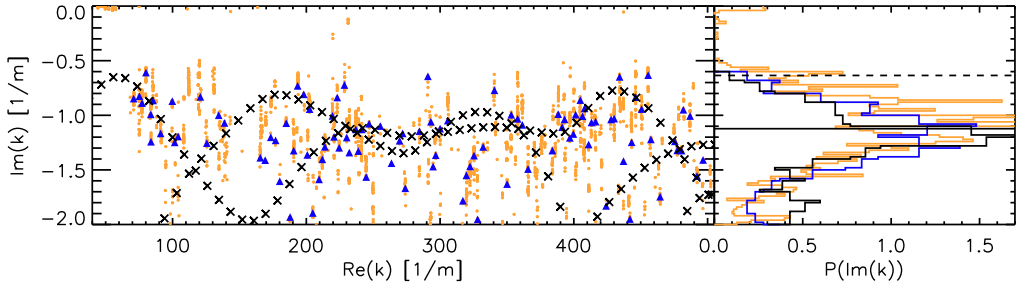

Figure 71: In the left panel the resonances for $R/a = 5.5$ in the complex k-plane are shown and the distribution of the imaginary parts of k in the right panel. The orange clouds correspond to all resonances leading to good reconstruction as well as the orange (averaged) histogram. Note that many orange dots overlay each other. Blue triangles and histogram describe the set belonging to the best reconstruction. Black crosses (and histogram) are the numerical poles. The dashed line in the right panel corresponds to $P(1/2)$, the solid line is $-\gamma_{\mathrm{cl}}/2$.

17.2 Spectral Gap and Classical Escape Rate

By measuring the averaged distribution $P(\mathrm{Im}(k))$ for symmetry reduced 3- and 5-disk systems for different R/a parameters we can now study its parametric dependence on the opening of the system (see figure 72) and can compare gap and maximum with the data calculated in appendix H.
For every R/a value we set up the averaged histogram $P(\mathrm{Im}(k))$ corresponding to the orange one in figure 71 and plotted them as a shade plot using the color code from white to black with increasing data value. For the 5-disk case the measured data is presented in figure 72(a). For $R/a = 2$ the system is completely closed, however, we observe already a small gap $\approx -0.15\,\mathrm{m}^{-1}$ caused by antenna and wall absorbing effects. While opening the system we first observe that the very narrow width distribution gets wider and that the maximum of the distribution moves towards higher imaginary parts. From approximately $R/a = 2.5$ the resonance free region starts to grow and reaches a value of approximately $\approx -0.5\,\mathrm{m}^{-1}$ for the maximal accessible opening at $R/a = 3.9$. Over the whole R/a range the value of $P(1/2)$ stays positive,

thus it provides no lower bound on the spectral gap. The solid black line in the shade plot corresponds to half the classical escape rate. It stops for $R/a = 2.41$ because for lower R/a values pruning sets in (in order 4). As already observed numerically in the high frequency regime [52] also in our experimental data in a much lower frequency regime the maximum of the width distribution is described by $-\gamma_{\mathrm{cl}}/2$. Here we emphasize that there are no free parameters to fit γ to the experiments. Theoretical and experimental values were derived independently!
More open systems can be realized by measuring the 3-disk system. Here the repeller becomes thin for $R/a \geq 2.83$ i.e. $P(1/2)$ becomes negative and provides a lower bound on the gap. As for the 5-disk system one observes again that the gap is increasing and for high R/a values the gap coincides well with the lower bound $P(1/2)$ (dotted black line). At which R/a parameter exactly the gap in the experimental data opens and whether it opens before $P(1/2)$ becomes negative is less clear as compared to the 5-disk system. The internal region of the totally closed system ($R/a = 2$) is too small to enable meaningful measurements. Here there are no pruned orbits of order 4 from $R/a = 2.01$, thus we are able to plot the calculated curve in the full measured range. The maximum of the width distribution decreases for $R/a > 3$ which is surprising at first sight. This decrease agrees however, with the decrease of the classical escape rate (solid black line). The reason for it is the chosen scaling. As in the experiments the disk radius stays fixed we chose a scaling proportional to a. Also in the theoretical studies a is normalized to 1. For a classical particle an increase of R/a means that each scattering at a disk is more defocussing. However, also the time of flight between two scattering events increases linearly which overcompensates the defocussing effect for large enough R/a leading to the decrease of γ. While for large R/a the maximum of the width distribution coincides with $-\gamma_{\mathrm{cl}}/2$ this coincidence seems not be true anymore for $R/a < 3.5$. As a consistency check figure 72(c) shows the shade plot for the numerical data of the symmetry reduced 3-disk system. Also there the correspondence of $-\gamma_{\mathrm{cl}}/2$ (solid black line) is clearly visible only for $R/a > 3.5$ and becomes less prominent for smaller R/a values. For $R/a > 4$ the lower bound $P(1/2)$ (dotted black line) coincides well with the numerically observed gap and seems to be a sharp bound there. The opening of the spectral gap is, however, not described by $P(1/2)$ which becomes most obvious for $2.5 < R/a < 2.83$. Here $P(1/2)$ is still positive but a clear gap is already visible, the same phenomenon as observed in the experimental data of the 5-disk system. Have in mind that the prediction of the gap is in the semiclassical limit whereas the experiments and numerical calculation are taking into account only up to 200 resonances. Thus the good agreement between the theoretical predictions and our experimental data comes as a

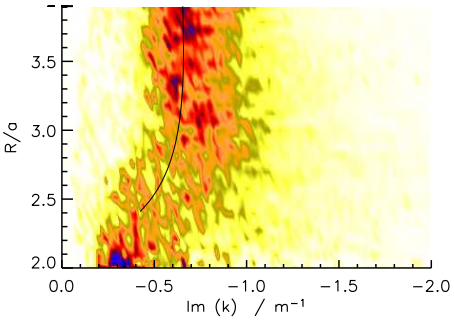

(a) 5-disk experiment

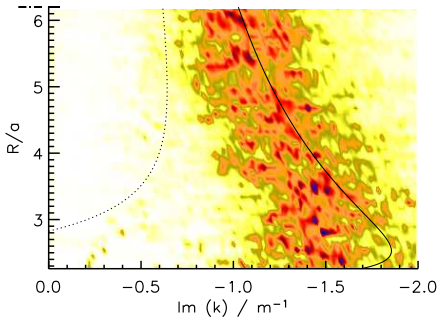

(b) 3-disk experiment

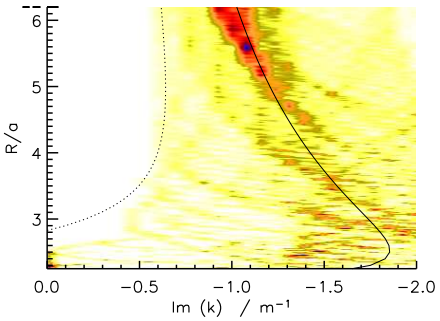

(c) 3-disk simulation

Figure 72: These figures show shade plots of the distribution of $\mathrm{Im}(k)$ depending on the R/a parameter for the 5-disk (a), the 3-disk experiment (b) and the 3-disk numeric (c). The classical escape rate (precisely: $-\gamma_{\mathrm{cl}}/2$) is the solid black line. $P(1/2)$ corresponds to the dotted line. For the 5-disk case the $P(1/2)$ is still positive and hence does not arise in the plot. All curves are only plotted where no pruning (until order $n = 4$) occurs.

surprise. We recognized that the resonance with the largest imaginary part, which defines the gap, is always found at quite low lying wave numbers, see e.g. the resonance at $\mathrm{Re}(k) = 55\,\mathrm{m}^{-1}$ in figure 71. It is not evident that those low lying resonances should already coincide with the prediction of a *semiclassical* quantity. But for larger R/a values it appears that this gap defined by just these resonances is optimally described by $P(1/2)$.

17.3 Counting Function and Hausdorff Dimension

For the investigation of the trend of the counting function exponents we focus on the 5-disk system as the accessible R/a range started at 2, the closed

case, and then the system can be opened step by step. In the 3-disk case the remaining area was so small that the antenna would have to be positioned to close to the walls. Hence in the following only the 5-disk data is analyzed. In order to study spectral asymptotics we have to determine the counting function (15.24) from the measured reflection spectrum. The resonances are obtained by applying the HI on the measured signal with all the parameters given in table 6 according to section 16.2. For each window and each parameter set the HI returns a set of complex resonances and amplitudes. Every set is checked for the reconstruction criterion and rejected or accepted. Now the density of states in the valid range of each window is obtained by averaging over the results of all remaining parameter sets taking care of a correct normalization. The *averaged* counting function finally was obtained by the averaged density of states of all windows. In the following we will refer to this "averaged counting function" only as "counting function". In figure

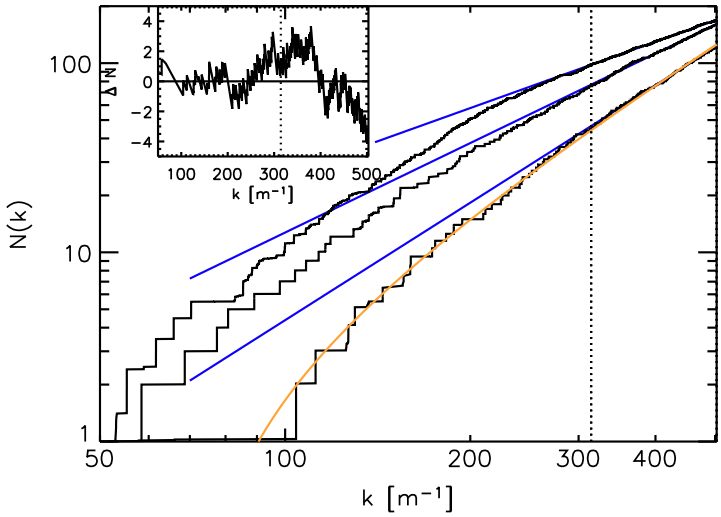

Figure 73: The counting functions for R/a=2, 2.25, and 3.9 (in this order from bottom to top) are plotted in black (histograms). Fits of their slope in the frequency range 15-24 GHz, corresponding to a k range of 315-500 mm^{-1} (dotted vertical line) are shown in blue (straight lines). The light orange curve over the lower histogram corresponds to the Weyl formula with 12% loss for the closed system. Plotted in the inset is the difference between the Weyl formula with 12% loss and the experimental counting function for the closed system (R/a=2).

73 three examples of the experimentally obtained counting functions for different R/a-parameters are shown: for the closed ($R/a = 2$) and the most open system ($R/a = 3.9$) as well as for the transition region ($R/a = 2.25$).

The curve of the closed system is compared to the prediction of the Weyl law (15.22) with area and boundary term corresponding to our cavity. Measuring only at one fixed position we cannot expect to find all resonances as several of them have an amplitude of the order of the noise. In closed room temperature aluminum cavities of similar sizes this typically lead to a loss of 5-10%. Here we found the best agreement between the histogramm of $R/a = 2$ and the Weyl law (15.22) with 12% loss (orange curve), which is still reasonable. The inset shows that the experimental data fluctuates around the theory with a deviation of less than 4 resonances.
For the open systems the fractal Weyl law only predicts the asymptotic exponent of the counting function. To compare our results with this prediction the slope was fitted with a standard regression (blue lines) to our experimental counting functions in the interval 15-24 GHz (marked by the dotted vertical line). For the fit we need on the one hand a sufficiently large range to extract the slope reliably, on the other hand we need large k to get into the semiclassical regime. In the chosen fit range all counting functions show an approximately linear behavior, especially the two extremal ones, indicating a suitable fit range also for all the other R/a parameters. In figure 74 shows the slopes of the counting functions obtained by this means parametrically plotted versus R/a. For the quantum-mechanically closed system the classical Weyl law predicts a value of 2. As long as the slit between disk and metallic wall is smaller than half a wavelength of the maximal frequency 24 GHz, the system is quantum mechanically closed and couples only by tunneling to the exterior. This region is highlighted by the darker blue shading and an exponent of 2 is still expected. For large R/a-parameter the fractal Weyl law predicts a fractional exponent between 1 and 2. The black solid line shows the calculated exponent $1+d_H$ of the fractal Weyl law, where d_H is the reduced fractal dimension of the repeller. The calculation of the exponent was described in section 15.4. Due to pruning effects this method fails to calculate d_H for small R/a parameters, thus the black theoretical line stops at $R/a = 2.4$. In between we expect a transition region smoothly connecting the two extremal regions (light blue shading). Experimentally the expected start value of about 2 for the closed system and a smooth transition to lower non-integer values between 1 and 2 is seen. For the open system the fitted exponents do not match the theoretically predicted curve, but the parametric dependence can be seen by shifting the theoretical curve down by 0.4. Nevertheless the exponents are significantly larger than one and definitely non integer.

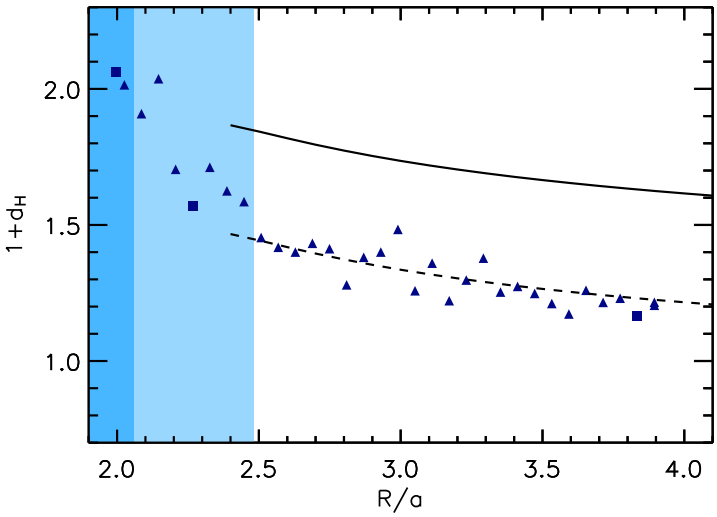

Figure 74: The data points correspond to the fitted exponent of the counting function in dependence of the R/a parameter. The solid line shows the asymptotic exponent $1+d_H$ predicted by the fractal Weyl law and the dashed curve is the same shifted by 0.4 as a guide to the eye. The three squares mark the examples which have already been presented in the previous figures. The darker shaded blue region indicates the R/a values without open channels whereas in the range marked by the lighter shaded blue region only a few open channels $(1 \ldots 8)$ exist.

17.4 Discussion

A possible explanation for the exponents being too low could be the following. Suppose that the probability, that the harmonic inversion overlooks some resonances, increases when the resonances become more and more overlapping. The density of states for the 5-disk system is supposed to increase like k^{d_H} thus with increasing k the resonances become stronger overlapping and the supposed loss of resonances increases as well. Such a loss, which increases with k, would lead to a systematically lower fitted exponent. Even if the procedure of averaging over many HI parameter sets and checking the reconstruction significantly increases the reliability of the results, those ambiguities will remain as this error occurs in every obtained resonance set. This assumption also is in accordance with the closed systems where no shift is necessary: As the resonance for the more closed systems are significantly less overlapping even for high frequencies (see figure 67) the loss-mechanism may not have set in, yet. Moreover there are of course the experimental uncertainties influencing the findings: The exponential behavior of the counting

function is predicted in the semiclassical limit, corresponding to the limit of infinite frequencies. Experimentally we are, however, restricted to a finite frequency and width range. In order to approach the semiclassical regime one may either increase the billiard size or reduce the billiard height and increase the frequency range (to remain below the cutoff frequency). Our cavity has already a side length of 1 m, a sufficient increase is hardly manageable. Also the height of 6 mm leaves no margin for reduction. Moreover one has to keep in mind that the fit takes place at a logarithmic scale and a significant improvement of the fit range would however demand an exponential increase of size or frequency range. Furthermore the loss mechanism described above will be much worse. Concluding we have to admit that a better experimental realization avoiding those sources of errors is not achievable. But the parametric dependence of d_H was reproduced correctly, as well as the non integer nature of this fractal dimension, being the first experimental finding on the fractal Weyl law. Moreover the results on the spectral gap confirming that the expression for it is only a bound and not a sharp limit hopefully motivate the mathematicians to focus on improving this bound. Up to now also the conglomeration of imaginary parts around the escape rate $(-\gamma_{cl}/2)$ is not well explained by mathematical means, but was now observed in a real physical system for the first time. Another important direction of research is the understanding of the shape of the distribution of imaginary parts. Here there are mainly theoretical approaches for weakly open system, coupling via only few channels to the environment [70, 67]. For wide open systems the shape of the distribution is of actual research interest [71].

A Mode Separation in the Helmholtz Equation

In the next paragraphs the separation of modes in the Helmholtz-equation is examined carefully, going beyond the standard mode picture of [17, 12]. The problem becomes more and more complicated the more modes are open. To keep the description as simple as possible the final equations are set up for the coupling of zeroth and first mode, to illustrate it with a concrete example. However from the universal ansatz the bulky expressions for other modes can be derived as well.
The starting point for the perturbation ansatz is the full Helmholtz equation for the z component of the electric field $\psi(x, y, z) = E_z(x, y, z)$

$$-(\partial_x^2 + \partial_y^2 + \partial_z^2)\ \psi(x, y, z) = k^2\ \psi(x, y, z) \tag{A.1}$$

We assume a spatially varying height $h(x, y)$ between the plates, which is a smooth function with a small derivative in x and y direction $\partial_{x/y} h(x, y) = \epsilon$. The ansatz for the wavefunction is given by the sum over the different cosine components as in (2.7), but with the spatially varying $h(x, y)$

$$\psi(x, y, z) = \sum_{n=0}^{n_{\max}} \psi_n(x, y)\ \cos\left(\frac{n\pi z}{h(x, y)}\right)$$

where the maximal mode number $n_{\max}$ is given by the condition

$$k^2 - \left(\frac{n\pi z}{h(x, y)}\right)^2 \overset{!}{\geq} 0 \quad \forall n \in [0, 1, \ldots n_{\max}]$$

Strictly speaking even $n_{\max}$ becomes a function of the position (x, y), which lead to fuzzy cut-off frequencies for the modes. Inserting the ansatz into the primary equation (A.1) we obtain

$$\begin{aligned}\Delta\ \psi(x, y, z) = \sum_{n=0}^{n_{\max}} \cos\left(\frac{n\pi z}{h(x, y)}\right) \Delta_{xy}\psi_n(x, y) + \\ 2\partial_x\psi_n(x, y)\ \partial_x \cos\left(\frac{n\pi z}{h(x, y)}\right) + 2\partial_y\psi_n(x, y)\ \partial_y \cos\left(\frac{n\pi z}{h(x, y)}\right) + \\ \psi_n(x, y)\Delta_{xy} \cos\left(\frac{n\pi z}{h(x, y)}\right) - \psi_n(x, y)\left(\frac{n\pi}{h(x, y)}\right)^2 \cos\left(\frac{n\pi z}{h(x, y)}\right)\end{aligned}$$

Due to the varying height there occur the extra terms including first and second order derivatives of the cosine which will be treated next: From here

we write $h \equiv h(x,y)$ except if its spatial dependency is stressed.

$$\begin{aligned}
\partial_x \cos\left(\frac{n\pi z}{h(x,y)}\right) &= \sin\left(n\pi z/h\right)\ \left(n\pi z/h^2\right)\partial_x h(x,y) \\
\partial_{xx} \cos\left(\frac{n\pi z}{h(x,y)}\right) &= \cos\left(n\pi z/h\right)\ \left(n\pi z/h^2\right)^2 \underbrace{\left(\partial_x h(x,y)\right)^2}_{\epsilon^2} \\
&- \sin\left(n\pi z/h\right)\left(2n\pi z/h^3\right)\underbrace{\left(\partial_x h(x,y)\right)^2}_{\epsilon^2} \\
&+ \sin\left(n\pi z/h\right)\left(n\pi z/h^2\right)\partial_{xx} h(x,y)
\end{aligned}$$

and analogously for ∂_y and ∂_{yy}. As the derivative of $h(x,y)$ is assumed to be small we neglect the two terms of order ϵ^2 in the further calculations. Thus we obtain

$$\begin{aligned}
\Delta\ \psi(x,y,z) = \sum_{n=0}^{n_{\max}} &\cos\left(n\pi z/h\right)\Delta_{xy}\psi_n(x,y) + 2\partial_x\psi_n(x,y)\sin\left(n\pi z/h\right)\left(n\pi z/h^2\right)\partial_x h(x,y) \\
&+2\partial_y\psi_n(x,y)\sin\left(n\pi z/h\right)\left(n\pi z/h^2\right)\partial_y h(x,y) + \psi_n(x,y)\sin\left(n\pi z/h\right)\left(n\pi z/h^2\right)\Delta_{xy} h(x,y) \\
&-\psi_n(x,y)\left(n\pi/h\right)^2\cos\left(n\pi z/h\right) + \mathcal{O}(\epsilon^2)
\end{aligned} \tag{A.2}$$

As we only want to explain the potential dependency of the $n = 0$ mode we restrict the occurring modes in this ansatz to TM_0 and TM_1 and write down the two summands:

$$\begin{aligned}
\mathrm{TM}_0 \ &: \quad \Delta_{xy}\psi_0(x,y) \\
\mathrm{TM}_1 \ &: \quad \cos\left(n\pi z/h\right)\Delta_{xy}\psi_1(x,y) + \psi_1(x,y)(\pi/h)^2\cos\left(n\pi z/h\right) + \sin\left(n\pi z/h\right)\ \left(\pi z/h^2\right)\cdot \\
&\quad [2\partial_x\psi_1(x,y)\ \partial_x h(x,y) + 2\partial_y\psi_1(x,y)\ \partial_y h(x,y) + \psi_1(x,y)\ \Delta_{xy} h(x,y)]
\end{aligned}$$

Now the $z\sin(\pi z/h)$-term is expanded in the basis of the cosines, approximated again by the first two modes:

$$\begin{aligned}
z\sin(\pi z/h) &= \sum_{n=0}^{\infty}\left[\int_0^h z\sin(\pi z/h)\cos(n\pi z/h)\mathrm{d}z\right]\cos(n\pi z/h) \\
&\approx \underbrace{\left[\int_0^h z\sin(\pi z/h)\mathrm{d}z\right]}_{=C_0} + \underbrace{\left[\int_0^h z\sin(\pi z/h)\cos(\pi z/h)\mathrm{d}z\right]}_{=C_1}\cos(n\pi z/h)
\end{aligned}$$

Now all the summands can be inserted in equation (A.2)

$$\begin{aligned}\Delta\ \psi(x,y,z) = &\Big\{\Delta_{xy}\psi_0(x,y) + 2C_0[2\partial_x\psi_1(x,y)\ \partial_x h(x,y)\\ &+ 2\partial_y\psi_1(x,y)\ \partial_y h(x,y) + \psi_1(x,y)\ \Delta_{xy}h(x,y)]\Big\}\\ &+ \cos(\pi z/h)\Big\{\Delta_{xy}\psi_1(x,y) + 2C_1[2\partial_x\psi_1(x,y)\ \partial_x h(x,y)\\ &+ 2\partial_y\psi_1(x,y)\ \partial_y h(x,y) + \psi_1(x,y)\ \Delta_{xy}h(x,y)] - (\pi/h)^2\psi_1(x,y)\Big\}\\ &+ \mathcal{O}(\epsilon^2)\end{aligned}$$

The terms in curly brackets $\{\dots\}$ contain the description of the zeroth and first component in the cosine expansion. The second one contains only ψ_1 and its derivatives. From that the TM_1 mode in first order perturbation can be calculated directly at least numerically, as it is not coupled to the other mode. Is one interested in only the correction of the TM_0 mode in first order perturbation, then one needs to solve only the original potential equation for TM_1 (2.7), as the additional terms will lead to order ϵ^2 terms if inserted into

$$\begin{aligned}(\Delta_{xy} + k^2)\ \psi_0(x,y) = &\ 2C_0[2\partial_x\psi_1(x,y)\ \partial_x h(x,y)\\ &+ 2\partial_y\psi_1(x,y)\ \partial_y h(x,y) + \psi_1(x,y)\ \Delta_{xy}h(x,y)]\end{aligned} \tag{A.3}$$

Here the inhomogeneity on the right hand side is only dependent on TM_1 and the first and second derivatives of the height function $h(x,y)$, which act as a source for TM_0. From this we see, that the zeroth mode is coupled to the first mode and will correspondingly feel a potential. This explains the observed mode coupling and the experimentally measured patterns for TM_0, shown in section 7.3. The impact of the source terms is additionally illustrated in the figures 28.

B Scaling Behavior of branched Flows

A detailed and mathematically strict derivation of the scaling law can be found in [72, 73]. In the following a hand-waving description is given.
The main idea of treating the weak random potential is a random walk ansatz for the momentum in the transverse y-direction.

$$\frac{\mathrm{d}p_y}{\mathrm{d}t} = \sigma_0^2 \eta(t) \tag{B.1}$$

where η with $\langle \eta(t)\eta(t')\rangle = \delta(t-t')$ is a delta-correlated Gaussian white noise and $\sigma_0^2 \propto \epsilon^2/l_c$ the kick strength (using the notation from [28]). The central limit theorem gives us the corresponding Fokker Planck equation for the probability $P(\tilde{p}_y, t) = \langle \delta(\tilde{p}_y - p_y)\rangle_\eta$ of finding $\tilde{p}_y$ at time t for the solution p_y of the Langevin equation (B.1) averaged over many noise realizations.

$$\frac{\partial P(p_y,t)}{\partial t} = \frac{\sigma_0^2}{2}\frac{\partial^2 P(p_y,t)}{\partial p_y^2}$$

It is a diffusion equation with the solution

$$P(p_y,t) = \frac{1}{\sqrt{2\pi\sigma_0^2 t}} e^{-p_y^2/2\sigma_0^2 t}$$

The second moment can be seen directly from the distribution

$$\langle p_y^2 \rangle = \sigma_0^2 t$$

Its square root gives the typical velocity in y-direction. The integral over it in time from 0 to t indicates the corresponding distance in y-direction, which was covered during t_0.

$$\int_0^t \sqrt{\langle p_y^2(\tau)\rangle}\mathrm{d}\tau = \sigma_0 t^{3/2}$$

As discussed above caustics occur if a trajectory has traveled around one correlation length l_c in transverse direction, thus it is at $t = t_0$

$$l_c \stackrel{!}{=} \sigma_0 t_0^{3/2}$$

Using the proportionality expression for σ_0^2 we finally obtain

$$t_0 = (l_c/\sigma_0)^{2/3} \propto l_c \epsilon^{-2/3}$$

C Determinant of Operators

Here only a heuristic argument for the identity ln det = Tr ln is given, for details see [50]. Let us assume a diagonal matrix

$$\begin{pmatrix} d_1 & 0 & \dots & 0 \\ 0 & d_2 & \dots & 0 \\ \vdots & 0 & \ddots & \vdots \\ 0 & \dots & 0 & d_n \end{pmatrix} \tag{C.1}$$

Then one can write

$$\det \exp D = e^{d_1} \dots e^{d_n} = e^{d_1 + \dots + d_n} = \exp\left(\mathrm{Tr} D\right) \tag{C.2}$$

Thus for a matrix $\ln L := D$ we obtain

$$\begin{aligned} \det \exp \ln L = \det L &= \exp\left(\mathrm{Tr} \ln L\right) \\ \ln \det L &= \mathrm{Tr} \ln L \end{aligned}$$

As ln and det are independent of the chosen basis the identity is valid for all finite operators and for those infinite ones which have a trace.

D Integral Operators

An integral operator with kernel $K(x, y)$ is defined as

$$(\hat{K}\varphi)(x) := \int K(x, y)\varphi(y)\,\mathrm{d}y$$

This is a sort of a generalization of the matrix multiplication

$$(A\nu)_i = \sum_j A_{ij}\nu_j$$

and especially

$$\mathrm{Tr}A := \sum_i A_{ii}$$

Based on this the (flat) trace for integral operators is -if existing-

$$\mathrm{Tr}^b\hat{K} := \int K(y, y)\,\mathrm{d}y$$

For well-behaved operators the flat trace and the trace, $\mathrm{Tr}\hat{K} := \sum\langle\nu|\hat{K}|\nu\rangle$, where the ν form an orthonormal basis of the Hilbert space $\mathcal{H}$, coincide.

E Heuristic Arguments for the fractal Weyl Law

In [52] Lu, Sridhar and Zworski gave some intuitive and some more mathematically rigorous derivations of the fractal Weyl law. Some of their ideas are repeated in the following to demonstrate their way of argumentation.
The standard Weyl law counts the number of independent quantum states in an energy shell Σ_E in a phase space of dimension $2d_{PS}$, where d_{PS} is the dimension of the system in configuration space. The smallest volume of a maximally localized quantum state is –based on the uncertainty principle– a box with side length $\sqrt{\hbar}$ and a volume $\sqrt{\hbar}^{2d_{PS}} = \hbar^{d_{PS}}$. Thus the number of resolved, i.e. countable, states is volume of energy shell divided by the $\hbar$-boxes $= \mathrm{Vol}(\Sigma_E)/\hbar^{d_{PS}}$.
For an open system the volume of the energy shell is infinite, as many points are carried to infinity (or come from infinity if you reverse the time direction). Hence the number of quantum resonances must be related to the volume of the trapped set $\mathcal{T}$, the set of points, which are not carried to infinity by the classical flow (again in both time directions). Thus we obtain for the number of maximally localized states on the trapped set, which corresponds to the number of eigenvalues of the parameter dependent differential equation $-\hbar^2\Delta\psi_n = k_n^2\psi_n$

$$\#\mathrm{EV}_{\hbar,a,b} := \{k_n \mid \ a \le k_n \le b\} \propto \frac{\mathrm{Vol}(\mathcal{T}_\hbar)}{\hbar^{d_{PS}/2}}$$

where $\mathcal{T}_\hbar = \{z \in \mathrm{PS} \mid \ d(z,k) < \sqrt{\hbar},\ k \in \mathcal{T}\}$ are those points in phase space with a distance to a point k in the trapped set of less than $\sqrt{\hbar}$. Consider now a covering of it

$$\bigcup_i X_i \quad \text{with} \ |X_i| < \sqrt{\hbar}$$
$$\Rightarrow \mathrm{Vol}(\mathcal{T}_\hbar) \propto \underbrace{N(\hbar)}_{\propto\ \hbar^{D_H/2}} \cdot \underbrace{\mathrm{Vol}(X_i)}_{\propto\ \hbar^{d_{PS}/2}}$$

where the definition of the Hausdorff dimension (15.25) for the first underbrace appears for small $\hbar$. For the number of resonances we then end up with

$$\#\mathrm{EV}_{\hbar,a,b} \propto \hbar^{-D_H/2} \quad \text{for small } \hbar \tag{E.1}$$

This problem is equivalent to the counting function of the non-parametric differential equation $-\Delta\psi_n = \tilde{k}_n^2\psi_n$ defined as

$$N(k) := \#\{0 < \tilde{k}_n < k\} \quad \text{where k is a real number}$$

Let us choose $k = 1/\hbar$. Then

$$N(k) = \#\{0 < \tilde{k}_n < \frac{1}{\hbar}\} = \#\{0 < \hbar\tilde{k}_n < 1\}$$

and $\tilde{k}_n$ solves $-\Delta\psi_n = \tilde{k}_n^2\psi_n$ if and only if $k_n := \hbar\tilde{k}_n$ solves $-\hbar^2\Delta\psi_n = k_n^2\psi_n$. Thus we know

$$N(k) = \#\mathrm{EV}_{\hbar=1/k,\ a=0,\ b=1} \overset{(E.1)}{\propto} (1/k)^{-D_H/2}$$

The Hausdorff dimension D_H and the reduced Hausdorff dimension d_H of a trapped set used e. g. in equation (15.23) are related by $D_H = 2d_H + 2$. This can be easily understood as D_H is given as

$$D_H(\text{trapped Set}) = 1 + 1 + d_H^{(u)} + d_H^{(s)}$$

where the first 1 corresponds to the conserved energy, as it lets the periodic orbits unchanged, the second 1 corresponds to the neutral direction of the classical flow and $d_H^{(u/s)}$ is the dimension of the unstable/stable manifold on the Poincare section. As the dynamics are reversible it is $d_H^{(u)} = d_H^{(s)} \equiv d_H$. Thus the Counting function finally looks like in the high energy regime

$$N(k) \propto k^{1+d_H}$$

F How the Hausdorff Dimension relates to the Root of the topological Pressure?

For the following argumentation an alternative definition of the Hausdorff dimension is more suitable than the one introduced in eq. (15.4). Let C be a set with a covering $C \subset \cup X_i$ with $|X_i| < \epsilon$, then the Hausdorff dimension is the number with

$$\sum_i |x_i|^s \stackrel{\epsilon\to 0}{\longrightarrow} \begin{cases} 0, & s \text{ too large} \\ \text{finite}, & s = d_H \\ \infty, & s \text{ too small} \end{cases}$$

It can be easily shown that this is equivalent to the statement that the number of covering spheres of a set goes like $N(\epsilon) \propto \epsilon^{-d_H}$ for $\epsilon \to 0$. Let us now cover the volume of the set with spheres of radius ϵ.

$$\text{Vol} \propto \sum_i \epsilon_i^s = N(\epsilon)\ \epsilon^s, \quad \text{where } N(\epsilon) \text{ is the number of necessary spheres}$$

As the volume is supposed to be finite we have $s = d_H \Leftrightarrow N(\epsilon) \propto \epsilon^{-d_H}$.
An illustrative example of the new definition is the covering of a 2 dimensional area, where the number of needed boxes with side length $1/n$ goes like n^2, thus we find

$$\text{Vol} \propto \sum_i (1/n)^s = n^2(1/n)^s = \text{finite} \ \Leftrightarrow \ s = 2$$

And for the Cantor 2/3-set the number of intervals goes like 2^n and the interval size with $(1/3)^n$ so that

$$\text{Vol} \propto 2^n(1/3)^{ns} = \text{finite} \ \Leftrightarrow \ s = \ln(2)/\ln(3)$$

the known Hausdorff dimension of the Cantor 2/3-set. In order to understand the relation between Hausdorff dimension and topological pressure in a very heuristic way we restrict the two dimensional dynamics on the Poincare section to the unstable manifold. The corresponding one-dimensional map $E(s)$ is expanding –as it was restricted to the unstable manifold. As we neglected the coordinate of the stable manifold, the map is not invertible anymore, but a so-called 2:1 map, i.e. a map where each point has two preimages. As an illustrative example such a map consists of two branches 0 and 1 (coming from the two valued symbolic dynamics of the symmetry-reduced 3 disk system) with slopes larger than one (as it is expanding). As shown in figure 75

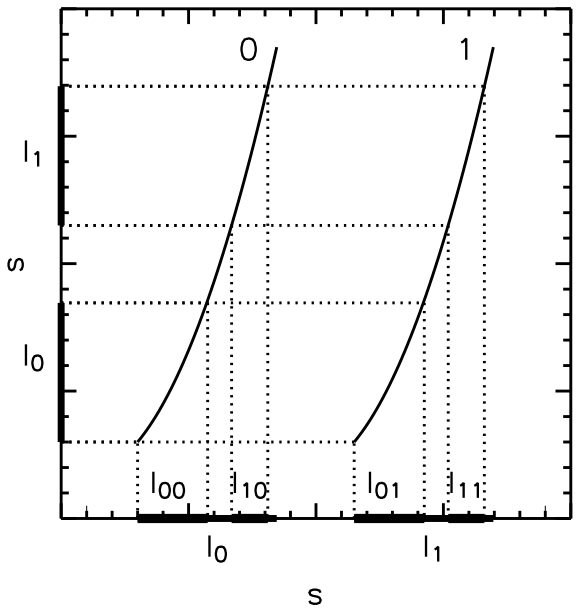

Figure 75: Schematic picture of map $E(s)$ on the unstable manifold and the intervals of first and second order for the symmetry reduced 3 disk system

only the subsets I_0 and I_1 of the full interval I remain finite under the map. With the second iteration there are four intervals I_{00}, I_{01}, I_{10} and I_{11} remaining finite. Further iterations lead to more and smaller nested intervals. The trapped set is then $\mathcal{T} \subset E^{-n}(I_0 \cup I_1)$ for every $n \in \mathbb{N}$. The interval of second order is e.g. defined like $I_{01} = E_1^{-1}\ E_0^{-1}(I)$. Thus for every binary word $w \in W_n$ of length n (equivalent to a periodic orbit) there is a corresponding interval I_w including a fixpoint x_w. A covering of this fractal set of intervals then has the form

$$\mathrm{Vol}_n = \sum_{w \in W_n} |I_w|^s = \sum_{w \in W_n} (1/\Lambda_w)^s \tag{F.1}$$

where the stability Λ_w can be described by $\left(\frac{\mathrm{d}}{\mathrm{dx}} E^n(x_w)\right)^{-1}$ for large n, the derivative at the fixpoints, which goes like $1/I_w$. Now we can rewrite equation (F.1)

$$\begin{aligned}
\sum_{w \in W_n} (1/\Lambda_w)^s &= \exp(n \underbrace{1/n \ln \sum \Lambda_w^{-s}}_{:=\tilde{P}_n(s)}) \\
&= \exp(n\ \tilde{P}(s)) \overset{\text{def } d_H}{\underset{n\to\infty}{\longrightarrow}} \begin{cases} 0, & \lim_{n\to\infty} \tilde{P}_n(s) < 0 \\ \text{finite}, & \lim_{n\to\infty} \tilde{P}_n(s = d_H) = 0 \\ \infty, & \lim_{n\to\infty} \tilde{P}_n(s) > 0 \end{cases}
\end{aligned}$$

Now it needs to be shown that $\lim_{n\to\infty} \tilde{P}_n(s) = 0 \Leftrightarrow P(s) = 0$, where P is the standard topological pressure defined in equation (15.21).

$$\begin{aligned}
P(s) = 0 \Leftrightarrow 0 &= \zeta_s^{-1}(0) \\
\text{(with (15.10))} &= \exp\left(-\sum_{n=1}^{\infty} \frac{\sum_{\text{fixpoints(n)}} \Lambda_z^{-s}}{n}\right) \\
&= \exp\left(-\sum_n \frac{1}{n} \left(\sqrt[n]{\sum_{w\in W_n} \Lambda_w^{-s}}\right)^n\right) \\
&= 1 - \sqrt[n]{\sum_{w\in W_n} \Lambda_w^{-s}} \\
\Leftrightarrow \quad &\underbrace{\frac{1}{n} \ln\left(\sum_{w\in W_n} \Lambda_w^{-s}\right)}_{\tilde{P}_n(s)} = \ln(1) = 0
\end{aligned}$$

Thus $s = d_H$ and the Hausdorff dimension is fixed by the condition $P(d_H) = 0$.

G Bound for the spectral Gap

Finding the resonance-free area in the complex plane is equivalent of finding the area where the ζ-function converges. It is possible to define the area, where it converges absolutely, which is of course a stronger condition. We have shown in section 15.5 that the resonances of the semiclassical ζ-function agree well with the quantum mechanical ones. Thus we start with the form (15.11) of the semiclassical ζ-function (15.27) knowing that a series $\sum_n f_n$ converges absolutely if $|f_n| \leq n^{-\alpha}$ for an exponent $\alpha > 1$:

$$\zeta^{-1}(z) = \exp\left(-\sum_{n=1}^{\infty}\sum_{p\in PO(n)}\frac{k_p}{n_p}\,\tau_p\right)$$

and the weights were defined as (15.16)

$$\tau_p = \exp\int_0^{T_p}\left[A_\beta - z\right]\,\mathrm{d}t$$

and for the semiclassical case

$$\begin{aligned} z &= -ik \\ A_\beta &= -\beta\;\kappa^{(u)} + i\pi\epsilon \end{aligned} \tag{G.1}$$

where $\beta = (1/2 + j),\ j \in \mathbb{N}$ and $\int_0^{T_p}\epsilon\,\mathrm{d}t = n_p$, the number of reflection of a trajectory. With $\int_0^{T_p}\kappa^{(u)}\,\mathrm{d}t = \ln\Lambda_p$ (15.17) and for $\beta = 1/2$ one recovers the case (15.27).
Let us now consider the modulus of the weight

$$|\tau_p| = \exp\int_0^{T_p}\left[\mathrm{Re}A - z\right]\,\mathrm{d}t$$

as another weight

$$\tilde{\tau}_p = \exp\int_0^{T_p}\left[-1/2\;\kappa^{(u)} - z\right]\,\mathrm{d}t \quad \text{for the case} \quad \beta = 1/2$$

With these weights now a classical ζ-function $\tilde{\zeta}_{\beta=1/2}(z)$ in the same form as in (15.15) can be defined. It is known [56] that it has a maximal real pole (i.e. the topological pressure $P(\beta = 1/2)$). Thus we know that $\tilde{\zeta}(z)$ converges on the real axis right from $P(1/2)$ (thick black line in figure 76 "rra") to infinity. As $\tilde{\zeta}(z)\Big|_{\mathrm{rra}}$ is a sum over exponentials with real arguments it is

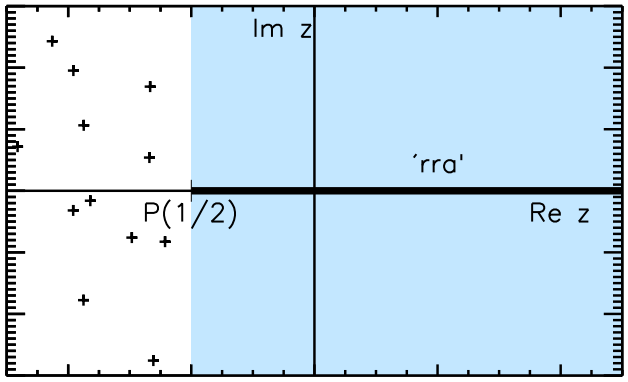

Figure 76: Schematic picture of the resonances of the semiclassical ζ-function (black crosses) in the complex plane and the resonance free region (blue shaded) defined by $P(1/2)$

even absolutely convergent. On the other hand $\tilde{\zeta}(z)\Big|_{\text{rra}}$ equals by definition $\exp\left(\sum_n \sum_p \frac{k_p}{n_p} |\tau_p|\right)$, which thus is absolutely convergent. Hence $\zeta(z) = \exp\left(\sum_n \sum_p \frac{k_p}{n_p} \tau_p\right)$ converges absolutely in the shaded region in the figure 76 and $P(1/2)$ is finally the bound for the resonances.
Additionally we have from the definitions

$$\text{Re}A < \text{Re}A' \Rightarrow P(A) < P(A')$$

so that the smallest possible real part of A $(= 1/2\ \kappa^{(u)})$ defines the best bound on the gap. Note that the complex plane in figure 76 is rotated by 90° (i.e. multiplication by i) compared to the complex plane in the other figures, e.g. 69. This comes from the extra i in front of the resonance position k in (G.1). For further purpose the semiclassical resonances were rotated backwards to coincide with the quantum mechanical ones.
Here it must be emphasized that the range of convergence can be of course larger than the range of absolute convergence, so that we found only a very rough bound as no phase cancellations were taken into account. But as it was presented in the experimental part of this thesis this bound seems to be sharp for wide open systems (see figure 72(b)).

H Implementation of the ζ-Function

For the implementation of the ζ-function the IDL procedures written by Alexander Potzuweit in [63] were the basis for my modifications. Especially the symmetry reduction was disregarded before and was added in the scope of this thesis. In the following a short overview over the algorithm and the main procedures is given, that can all be found in the *idl4dat.lib*: The most important procedure is calc_ZetaFunc_stability_st.pro. It obtains the system's geometry (i.e. position and radius of the disks) and returns the Hausdorff dimension, the classical escape rate, $P(1/2)$ or the values of the function value of the classical or semiclassical ζ-function up to a specified order L of periodic orbits. First the stabilities and orbit lengths of the certain disk geometry are calculated. With the function get_orbits_SymRed.pro all the symbolic orbits of a word length $w \leq W$ are collected combinatorically, e.g. the orbits 0 and 1 in the 3-disk case in order $W = 1$. Afterwards these orbits must be converted in the global notation of disk numbers ($0 \to \overline{23}$ and $1 \to \overline{123}$) because only from this notation the function calc_orbit_st.pro can calculate the coordinates of the orbits, precisely the coordinates of the collisions with the disks, using a minimization method by IDL (amoeba.pro). Now optionally a pruning check can be performed: All line segments of the orbits are checked for intersection points with the disks' boundaries. If there are more intersection points then start and end point this orbit and with that all other orbits of that order are rejected and "NaN" is returned. If all the orbits are valid then its stabilities are calculated using the monodromy matrices [62]. We have

$$m_{\text{coll}} = \begin{pmatrix} -1 & 0 \\ \frac{-2}{a\ \cos(\phi)} & -1 \end{pmatrix} \quad \text{for the collisions} \tag{H.1}$$

$$m_{\text{line}} = \begin{pmatrix} 1 & L_{\text{free}} \\ 0 & 1 \end{pmatrix} \quad \text{for the free flights} \tag{H.2}$$

where ϕ is the angle of the reflection respective to the perpendicular at the intersection point, a the disk radius and L_{free} the length of the line segment. Those matrices are now consecutively multiplied for every orbit. The stability of the orbit is now the eigenvalue of the final matrix whose modulus square is larger than one. This is done in calc_lambda.pro with the IDL procedure La_eigenproblem.pro. At the same time the geometrical orbit length and the word length (corresponds to the number of reflections) are saved. Note that all those findings are valid for the global geometry. To return to the symmetry reduction the ratio f between global word length and reduced word length is needed, as this describes the multiplicity of the reduced orbit. Now

the reduced length and reduced stability can be calculated via $L_{\text{red}} = L_{\text{glob}}/f$ and $\Lambda_{\text{red}} = \sqrt[f]{\Lambda_{\text{glob}}}$ as the period length of the full orbit is the sum along the segments and its stability the product of the reduced stabilities [50]. From the reduced word lengths, geometrical lengths and stabilities of the individual orbits every combination up to a fixed maximal order is calculated using a recursive algorithm (calc_LambdaComb_rek.pro, calc_TpComb_rek.pro, calc_NpComb_rek.pro). From that the classical or semiclassical ζ-function is accessible. Via different keywords in calc_ZetaFunc_stability_st.pro the roots in z of equation (15.20) for β values of 1 (escape rate) or 1/2 (bound) or the (real) root in β for $z = 0$ (d_H) can be obtained. Moreover the function values of classical (15.20) or semiclassical (15.27) ζ-function can be returned with keywords zeta_values respectively SemiClass_values. Hence it is possible to

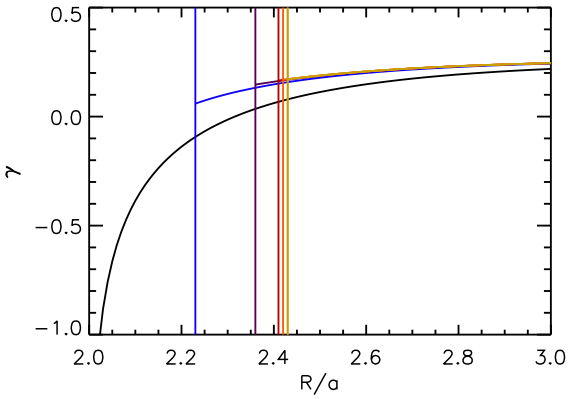

Figure 77: Classical escape rate for a 5-disk system with $a = 1$ in order $n = 1 \ldots 7$ (from black to orange). The vertical lines indicate the start point of the curves, where no orbits are pruned

carry out a loop over many R/a configurations and return d_H (further used in section 17.3) or γ_{cl} and $P(1/2)$ (see section 17.2) parametrically. One example is shown in figure 77 for γ_{cl} in a 5-disk system, calculated in orders $n = 0 \ldots 7$. All the curves are only plotted in a range, where no pruning occurs. That means that all the included periodic orbits were checked for no extra intersection points with disk boundaries, see the orbit examples in figure 57. The vertical lines mark the corresponding R/a parameters. It turns out that the curves converge well and also the ending of the pruning seems to converge around $R/a = 2.41$. Based on this picture and tests of the 3-disk systems we decided to calculate the classical quantities in all the further plots up to an order of 4, which corresponds to the red line in the figure, to achieve a suitable accuracy, but take care of the computing time.

I Calculation of quantum mechanical n-Disk Resonances

For the 3-disk system Gaspard and Rice [51] 1989 gave an explicit expression for its scattering matrix in terms of Bessel and Hankel functions which allows to calculate the quantum resonances numerically by evaluating the poles of the scattering matrix. In 1999 Wirzba investigated the scattering matrices for any n-disk system with arbitrary disk radii and disk number in detail [55]. As the numerical code was already implemented for Sebastian Möckel's Bachelor thesis [74] and he already gave a detailed description and summary of the derivation of the matrices I restrict here to only a short overview over the algorithm: The boundary value problem of a quantum mechanical wave, scattered at hard obstacles, has to be solved. Let $\psi_m^k(\vec{r})$ be a solution of the problem at wave number k and m the quantum number of the angular momentum. It obeys

$$(\Delta_r + k^2)\ \psi_m^k(\vec{r}) = 0 \tag{I.1}$$

outside and $\psi_m^k(\vec{r}) = 0$ at the disks' boundaries. Sufficiently far apart from the scattering center the wave function can be described in terms of the scattering matrix S like

$$(\Delta_r + k^2)\ \psi_m^k(\vec{r}) \propto \frac{1}{\sqrt{2\pi kr}} \sum_{l=-\infty}^{\infty} \left[\delta_{ml} e^{-i(kr-\pi/2l-\pi/4)} + S_{ml} e^{i(kr-\pi/2l-\pi/4)}\right] e^{il\phi_r} \tag{I.2}$$

where r and ϕ_r are modulus and polar angle of vector $\vec{r}$. The scattering element S_{ml} defines the scattering of an incoming wave with quantum number of the angular momentum m into an outgoing wave with quantum number l. As S corresponds to the unity matrix if no scattering occurs it is suitable to write S as the deviation from unity $S(k) \equiv 1 - iT(k)$. In general S can be extremely complicated, but for our symmetric n-disk systems one can decompose it into [55]

$$\begin{aligned} S_{mm'}(k) &= \delta_{mm'} - iT_{mm'}(k) && \text{(I.3)} \\ &= \delta_{mm'} - iC_{ml}^{j}(k) \left(M^{-1}(k)\right)_{ll'}^{jj'} D_{l'm'}^{j'}(k) && \text{(I.4)} \end{aligned}$$

The indices m, m', l, l' correspond to the angular momenta, whereas the upper indices j, j' indicate the disk numbers. There are explicit expression for the matrices C, D and M, but they are quite bulky and we will see that only M is relevant for the singularities of the scattering matrix

$$M_{ll'}^{jj'} = \delta_{jj'}\delta_{ll'} + (1-\delta_{jj'})\frac{a_j}{a_{j'}}\frac{J_l(ka_j)}{H_{l'}^{(1)}(ka_{j'})} H_{l-l'}^{(1)}(kR_{jj'})\ e^{i(\alpha_{j'j} - l'(\alpha_{j'j}-\pi))} \tag{I.5}$$

where $R_{jj'}$ is the distance between the disk centers j and j', $\alpha_{j'j}$ the angle between the vector pointing at disk center j' and the vector connecting the disk centers j and j' and $H^{(1)}$ the Hankel function of first kind. For the determinants one finds

$$\det_L S = \frac{\det_L(M - iDC)}{\det_L(M)} \tag{I.6}$$

where index L stands for the operation on the extended tuple (l, j) of quantum numbers and disks and index l only for the quantum numbers. Equation (I.6) shows that the singularities of the scattering matrix S, i.e. the quantum resonances, corresponds to the roots of the determinant of M as long as D and C behave well (what they do [55]!).
For the 3-disk case equation (I.5) reduces to

$$M_{ll'}^{jj'} = \delta_{jj'}\delta_{ll'} + \frac{J_l(ka)}{H_{l'}^{(1)}(ka)}\ H_{l-l'}^{(1)}(kR)\ \xi_{jj'}(l, l') \tag{I.7}$$

with

$$\xi_{jj'}(l, l') = (1 - \delta_{jj'})\ e^{i(\alpha_{j'j} - l'(\alpha_{j'j} - \pi))} \tag{I.8}$$

For the symmetry reduced case of the 3-disk system M can be decomposed even more with respect to the three different representations of the group $C_{3\nu}$: the one-dimensional symmetric A_1 and antisymmetric A_2 and the two-dimensional representation E. Their concrete expressions can be found in [51] and form the basis of the computation. All the results –presented for example in figures 71 and 72(c)– are calculated for the A_2 representation as this one corresponds to the experiments. For the code the implementation of complex Bessel and Hankel function was performed using the *TBCI templated C++ numerical library*, the calculation of the determinant was done with a stabilized LU-decomposition and the root finding process was a globally convergent Newton-Raphson algorithm with line search and backtracking, both taken form the numerical recipes [75]. The approximation of the infinite-dimensional matrices and the limits of the used functions were already investigated in [74], finding a satisfying accuracy of two decimal places for the resonances.

References

[1] W. Schrödinger. Quantisierung als Eigenwertproblem. 79:361, 1926.

[2] F. Bloch. Über die Quantenmechanik der Elektronen in Kristallgittern. *Z. Phys. A*, 52:555, 1929.

[3] Alfred Wegener. *Die Entstehung der Kontinente und Ozeane*, volume 66. F. Vieweg, 1920.

[4] N. Bohr. Über die Serienspektra der Elemente. *Z. Phys.*, 2:423, 1920.

[5] R. P. Feynman and A. R. Hibbs. *Quantum Mechanics and Path Integrals*. McGraw-Hill, New York, 1965.

[6] M. C. Gutzwiller. *Chaos in Classical and Quantum Mechanics*. Interdisciplinary Applied Mathematics, Vol. 1. Springer, New York, 1990.

[7] H. Weyl. Über das Spektrum der Hohlraumstrahlung. *Journal für die reine und angewandte Mathematik*, 141:163, 1912.

[8] E. J. Heller. Bound-state eigenfunctions of classically chaotic Hamiltonian systems: Scars of periodic orbits. *Phys. Rev. Lett.*, 53:1515, 1984.

[9] H.-J. Stöckmann. *Quantum Chaos - An Introduction*. University Press, Cambridge, 1999.

[10] P. W. Anderson. Absence of diffusion in certain random lattices. *Phys. Rev.*, 109:1492, 1958.

[11] D. S. Wiersma, P. Bartolini, A. Lagendijk, and R. Righini. Localization of light in a disordered medium. *Nature*, 390:671, 1997.

[12] Y.-H. Kim, U. Kuhl, H.-J. Stöckmann, and J. P. Bird. Investigating dynamical tunnelling in open quantum dots by means of a soft-walled microwave-cavity analogue. *J. Phys.: Condens. Matter*, 17:L191, 2005.

[13] P. Gaspard and S. A. Rice. Semiclassical quantization of the scattering from a classically chaotic repeller. *J. Chem. Phys.*, 90:2242, 1989.

[14] P. Cvitanović and B. Eckhardt. Periodic-orbit quantization of chaotic systems. *Phys. Rev. Lett.*, 63:823, 1989.

[15] J. Stein and H.-J. Stöckmann. Experimental determination of billiard wave functions. *Phys. Rev. Lett.*, 68:2867, 1992.

[16] H.-J. Stöckmann and J. Stein. "Quantum" chaos in billiards studied by microwave absorption. *Phys. Rev. Lett.*, 64:2215, 1990.

[17] H.-M. Lauber, P. Weidenhammer, and D. Dubbers. Geometric phases and hidden symmetries in simple resonators. *Phys. Rev. Lett.*, 72:1004, 1994.

[18] M. A. Topinka, B. J. LeRoy, S. E. J. Shaw, E. J. Heller, R. M. Westervelt, K. D. Maranowski, and A. C. Gossard. Imaging coherent electron flow from a quantum point contact. *Science*, 289:2323, 2000.

[19] K. E. Aidala, R. E. Parrot, T. Kramer, E. J. Heller, R. M. Westervelt, M. P. Hanson, and A. C. Gossard. Imaging magnetic focusing of coherent electron waves. *Phys. Rev. E*, 72:066214, 2005.

[20] M. P. Jura, M. A. Topinka, L. Urban, A. Yazdani, H. Shtrikman, L. N. Pfeiffer, K. W. West, and D. Goldhaber-Gordon. Unexpected features of branched flow through high-mobility two-dimensional electron gases. *Nature*, 3:841, 2007.

[21] E. J. Heller, L. Kaplan, and A. Dahlen. Refraction of a Gaussian seaway. *J. Geophys. Res.*, 113:C09023, 2008.

[22] M. A. Wolfson and S. Tomsovic. On the stability of long-ragne sound propagation through a structured ocean. *J. Acoust. Soc. Am.*, 109:2693, 2001.

[23] R. Höhmann, U. Kuhl, H.-J. Stöckmann, L. Kaplan, and E. J. Heller. Freak waves in the linear regime: A microwave study. *Phys. Rev. Lett.*, 104:093901, 2010.

[24] B. S. White and B. Fornberg. On the chance of freak waves at sea. *J. Fluid Mech.*, 355:113, 1998.

[25] M. V. Berry. Regular and irregular semiclassical wavefunctions. *J. Phys. A*, 10:2083, 1977.

[26] R. Höhmann. *Experimental tests of random wave models with chaotic microwave billiards*. PhD thesis, Philipps-Universität Marburg, 2008.

[27] L. Kaplan. Statistics of branched flow in a weak correlated random potential. *Phys. Rev. Lett.*, 89:184103, 2002.

[28] J. J. Metzger, R. Fleischman, and T. Geisel. Universal statistics of branched flow. *Phys. Rev. Lett.*, 105:020601, 2010.

[29] J. J. Metzger. private communication.

[30] J. Unterhinninghofen, U. Kuhl, J. Wiersig, H.-J. Stöckmann, and M. Hentschel. Measurement of the Goos-Hänchen shift in a microwave cavity. *New J. of Physics*, 13:023013, 2011.

[31] L. Bittrich. *Flooding of Regular Phase Space Islands by Chaotic States*. PhD thesis, Technische Universität Dresden, 2010.

[32] M. S. Longuet-Higgins. The statistical analysis of a random, moving surface. *Phil. Trans. R. Soc. Lond. A*, 249:321, 1957.

[33] R. Schäfer M. C. Münnix and T. Guhr. A random matrix approach to credit risk. Preprint, 2011. arXiv:1102.3900.

[34] ITAP. Technische Daten zum Windkanal, Online-Publikation, http://www.itap.de/windkanal.pdf, 1.12.2012.

[35] Pascal Knebel. *Aktives Gitter zur Simulation atmosphärischer Windfelder im Windkanal*. PhD thesis, Universität Oldenburg, 2011.

[36] R. Stresing, J. Peinke, R. E. Seoud, and J. C. Vassilicos. Defining a new class of turbulent flows. *Phys. Rev. Lett.*, 104:194501, 2010.

[37] A. N. Kolmogorov. A refinement of previous hypotheses concerning the local structure of turbulence in a viscous incompressible fluid at high Reynolds number. *J. Fluid Mech.*, 13:82, 1962.

[38] M. J. Lighthill. On the generated aerodynamically turbulence as a source of sound. *Proc. R. Soc. Lond. A*, 222:1148, 1954.

[39] J. E. F. Williams and D. L. Hawkings. Sound generation by turbulence and surfaces in arbitrary motion. *Phil. Trans. R. Soc. Lond. A*, 264:321, 1969.

[40] Y.-H. Kim, M. Barth, H.-J. Stöckmann, and J. P. Bird. Wavefunction scarring in open quantum dots: A microwave-billiard analogy study. *Phys. Rev. B*, 65:165317, 2002.

[41] U. Dörr, H.-J. Stöckmann, M. Barth, and U. Kuhl. Scarred and chaotic field distributions in three-dimensional Sinai-microwave resonators. *Phys. Rev. Lett.*, 80:1030, 1998.

[42] W. E. Bies, L. Kaplan, M. R. Haggerty, and E. J. Heller. Localization of eigenfunctions in the stadium billiard. *Phys. Rev. E*, 63:066214, 2001.

[43] S. Barkhofen, T. Weich, A. Potzuweit, H.-J. Stöckmann, U. Kuhl, and M. Zworski. Experimental observation of the spectral gap in microwave n-disk systems. *Phys. Rev. Lett.*, 110:164102, 2013.

[44] A. Potzuweit, T. Weich, S. Barkhofen, U. Kuhl, H.-J. Stöckmann, and M. Zworski. Weyl asymptotics: From closed to open systems. *Phys. Rev. E*, 86:066205, 2012.

[45] M. Ikawa. Decay of solutions of the wave equation in the exterior of several convex bodies. *Ann. Inst. Fourier*, 38:113, 1988.

[46] P. Gaspard and S. A. Rice. Scattering from a classically chaotic repellor. *J. Chem. Phys.*, 90:2225, 1989.

[47] K. Pance, W. Lu, and S. Sridhar. Quantum fingerprints of classicsl Ruelle-Pollicot resonances. *Phys. Rev. Lett.*, 85:2737, 2000.

[48] W. Lu, L. Viola, K. Pance, M. Rose, and S. Sridhar. Microwave study of quantum n-disk scattering. *Phys. Rev. E*, 61:3652, 2000.

[49] B. Eckhardt, G. Russberg, P. Cvitanović, P. Rosenqvist, and P. Scherer. Pinball scattering. In C. Casati and B. Chirikov, editors, *Quantum Chaos Between Order and Disorder*, page 405. University Press, Cambridge, 1995.

[50] P. Cvitanović and B. Eckhardt. Symmetry decomposition of chaotic dynamics. *Nonlinearity*, 6:277, 1993.

[51] P. Gaspard and S. A. Rice. Exact quantization of the scattering from a classically chaotic repellor. *J. Chem. Phys.*, 90:2255, 1989.

[52] W. T. Lu, S. Sridhar, and M. Zworski. Fractal Weyl laws for chaotic open systems. *Phys. Rev. Lett.*, 91:154101, 2003.

[53] P. Cvitanović and B. Eckhardt. Periodic orbit expansions for classical smooth flows. *J. Phys. A*, 24:L237, 1991.

[54] P. Gaspard and D. Alonso Ramirez. Ruelle classical resonances and dynamical chaos: The three- and four-disk scatterers. *Phys. Rev. A*, 45:8383, 1992.

[55] A. Wirzba. Quantum mechanics and semiclassics of hyperbolic n-disk scattering systems. *Phys. Rep.*, 309:1, 1999.

[56] D. Ruelle and G. Gallavotti. *Thermodynamic formalism*, volume 112. Addison-Wesley Reading, Massachusetts, 1978.

[57] S. Nonnenmacher and M. Zworski. Quantum decay rates in chaotic scattering. *Acta Mathematica*, 203:149, 2009.

[58] S. Nonnenmacher. Spectral problems in open quantum chaos. *Nonlinearity*, 24:R123, 2011.

[59] V. Petkov and L. Stoyanov. Analytic continuation of the resolvent of the Laplacian and the dynamical zeta function. *Anal. PDE*, 3:427, 2010.

[60] H. P. Baltes and E. R. Hilf. *Spectra of Finite Systems*. BI-Wissenschaftsverlag, Mannheim, 1976.

[61] J. Sjöstrand. Geometric bounds on the density of resonances for semiclassical problems. *Duke Math. J.*, 60:1, 1990.

[62] P. Gaspard. *Chaos, scattering and statistical mechanics*. University Press, Cambridge, 1998.

[63] A. Potzuweit. Mikrowellenmessungen an n-Scheiben Streusystemen. Master's thesis, Philipps-Universität Marburg, 2009.

[64] T. Weich. Resonances in open expanding maps and in an experimental realization of the three disk system. Master's thesis, Philipps-Universität Marburg, 2010.

[65] J. Stein, H.-J. Stöckmann, and U. Stoffregen. Microwave studies of billiard Green functions and propagators. *Phys. Rev. Lett.*, 75:53, 1995.

[66] J. Main, P. A. Dando, D. Belkić, and H. S. Taylor. Decimation and harmonic inversion of periodic orbit signals. *J. Phys. A*, 33:1247, 2000.

[67] U. Kuhl, R. Höhmann, J. Main, and H.-J. Stöckmann. Resonance widths in open microwave cavities studied by harmonic inversion. *Phys. Rev. Lett.*, 100:254101, 2008.

[68] H. Padé. *Sur la représentation approchée d'une fonction par des fractions rationnelles*. Number 740 in Théses de la Faculté des sciences de Paris. Gauthier-Villars et Fils, 1892.

[69] Y. V. Fyodorov and D. V. Savin. Statistics of resonance width shifts as a signature of eigenfunction nonorthogonality. *Phys. Rev. Lett.*, 108:184101, 2012.

[70] H. J. Sommers, Y. V. Fyodorov, and M. Titov. S-matrix poles for chaotic quantum systems as eigenvalues of complex symmetric random matrices: from isolated to overlapping resonances. *J. Phys. A*, 32:L77, 1999.

[71] H. Schomerus and J. Tworzydło. Quantum-to-classical crossover of quasibound states in open quantum systems. *Phys. Rev. Lett.*, 93:154102, 2004.

[72] V. A. Kulkarny and B. S. White. focusing of waves in turbulent inhomogeneous media. *Phys. Fluids*, 25:1770, 1982.

[73] J. Metzger. *Branched Flow and Caustics in two-dimensional random potentials and magnetic fields.* PhD thesis, University of Göttingen, 2010.

[74] S. Möckel. Berechnung der quantenmechanischen Resonanzen in n-Disc Systemen, jun 2010.

[75] W. H. Press, B. P. Flannery, S. A. Teukolsky, and W. T. Vetterling. *Numerical recipes in PASCAL.* Cambridge University Press, New York, 1990.

Acknowledgments

I thank everybody who contributed to the success of this thesis. My special thanks goes to the following persons:

Prof. Dr. H.-J. Stöckmann for many fruitful discussions, for giving me the possibility to do my PhD in his group, the substantial feedback to my work, and last but not least for providing the ideas for the projects,

Prof. Dr. U. Kuhl for the choice of the topic, all the suggestions concerning measurements and data analysis, for giving me the opportunity to take part in so many conferences and events and the friendly supervision during my time in the quantum chaos group,

Prof. Dr. B. Eckhardt as a second referee for help and discussions about the n-disk systems and the detailed feedback,

Prof. Dr. J. Peinke for the hospitality during my stay in Oldenburg and for giving me the opportunity to perform several sound measurements in his laboratory,

Dr. Ragnar Fleischmann and Dr. Jakob Metzger from Göttingen for the cooperation in our joint project and the simulations of the branched flow,

The members of the electronic workshop for their reliable support with all the measuring equipment and the rescue of the Wiltron,

The members of the mechanic workshop for the help with the large measurement table and the tuning of the antenna,

My colleagues Markus Allgaier, Julian Böhm, Stefan Gehler, Bernd Köber of the quantum chaos group in Marburg for the pleasant working atmosphere,

My parents for the great support not only during my study and but the last 27 years,

My dear boyfriend Tobi for all his patience, the encouragement and the constructive feedback on all my work.

Wissenschaftlicher Werdegang

14.10.1985	geboren in Krefeld
2005-2010	Studium der Physik an der Philipps-Universität Marburg
27.09.2007	Vordiplom mit Nebenfach Informatik
08.06.2010	Diplom mit Nebenfach Mathematik
2009-2010	Diplomarbeit in der Arbeitsgruppe Quantenchaos (PD. Dr. Ulrich Kuhl und Prof. Dr. H.-J. Stöckmann): *Microwave Measurements on Graphene-like structures*
2010-2013	Promotion in der Arbeitsgrupppe Quantenchaos an der Philipps-Universität Marburg *Microwave Measurements on n-Disk Systems and Investigation of Branching in correlated Potentials and turbulent Flows*